UCTEA Turkish Chamber of Civil Engineers
TMMOB İnşaat Mühendisleri Odası

Turkish Journal of Civil Engineering

formerly
Teknik Dergi

Volume 36
Issue 2
March 2025

Turkish Journal of Civil Engineering (formerly Teknik Dergi) Publication Principles

Turkish Journal of Civil Engineering (TJCE), a non-profit, open access scientific and technical periodical of UCTEA Chamber of Civil Engineers, publishes papers reporting original research work and major projects of interest in the area of civil engineering. TJCE annually publishes six issues and is open to papers in English and Turkish. It should be noted that TJCE (formerly, Teknik Dergi/ Technical Journal of Turkish Chamber of Civil Engineers) is being published regularly for more than 30 years since 1990. Main publication principles of TJCE are summarized below:

1. Articles reporting original scientific research and those reflecting interesting engineering applications are accepted for publication. To be classified as original, the work should either produce new scientific knowledge or add a genuinely new dimension to the existing knowledge or develop a totally new method or substantially improve an existing method.
2. Articles reporting preliminary results of scientific studies and those which do not qualify as full articles but provide useful information for the reader can be considered for publication as technical notes.
3. Discussions received from the readers of the published articles within three months from publication are reviewed by the Editorial Board and then published together with the closing remarks of the author.
4. Manuscripts submitted for publication are evaluated by two or three reviewers unknown to the authors. In the light of their reports, final decision to accept or decline is taken by the Editorial Board. General policy of the Board is to get the insufficient manuscripts improved in line with the reviewers' proposals. Articles that fail to reach the desired level are declined. Reasons behind decisions are not declared.
5. A signed statement is taken from the authors, declaring that the article has not been published as a "journal article or book chapter". In case the Editorial Board is in the opinion that the article has already been published elsewhere with minor changes or suspects plagiarism or a similar violation of ethics, then not only that article, but none of the articles of the same authors are published.
6. Papers reporting works presented as conference papers and developed further may be considered for publication. The conference it was presented to is given as a footnote in the first page.
7. Additionally, a document signed by all authors, transferring the copyright to UCTEA Chamber of Civil Engineers is submitted together with the manuscript.

UCTEA Turkish Chamber of Civil Engineers
TMMOB İnşaat Mühendisleri Odası

Turkish Journal of Civil Engineering

formerly
Teknik Dergi

Volume 36
Issue 2
March 2025

UCTEA Turkish Chamber of Civil Engineers
TMMOB İnşaat Mühendisleri Odası
Necatibey St. No: 57, Kızılay 06440 Ankara, Turkey
Tel: +90.312.294 30 00 - Faks: +90.312.294 30 88
E-mail: imo@imo.org.tr - www.imo.org.tr

Publisher *(Sahibi)*:
Nusret SUNA
On behalf of UCTEA Turkish Chamber of Civil Engineers

Administrative Officer *(Yazı İşleri Müdürü)*:
Bülent TATLI

Volume 36 - Issue 2 - March 2025 *(Cilt 36 - Sayı 2 - Mart 2025)*
Published bi-monthly. Local periodical. *(İki ayda bir yayınlanır, yerel süreli yayın)*
Date of Print: March 1, 2025 *(Baskı Tarihi: 1 Mart 2025)*

ISSN: 2822-6836

Turkish Journal of Civil Engineering (formerly Teknik Dergi) is indexed by
- Science Citation Index Expanded
- Scopus
- Journal Citation Reports / Science Edition
- TRDizin
- Engineering Index
- Concrete Abstracts (American Concrete Institute)
- National Technical Information Service (US NTIS)
- CITIS
- EBSCO
- Ulrich's International Periodical's Directory
- Google Scholar

Turkish Journal of Civil Engineering (formerly Teknik Dergi) is a peer reviewed open access periodical publishing papers of original research and interesting practice cases. It addresses both the research community and the practicing engineers.

Printed by *(Baskı)*:
Ankamat Matbaacılık San.
İvedik OSB. 1344. Sok. Yenimahalle / Ankara - Tel: 0.312.394 54 64
Sertifika No: 46700

Reviewers:

This list is renewed each year and includes reviewers who served in the last two years of publication.

Suman Kumar ADHIKARY
Kamil Bekir AFACAN
Ayda Şafak AĞAR ÖZBEK
Elif AĞCAKOCA
Bülent AKBAŞ
Sami Oğuzhan AKBAŞ
Zülal AKBAY ARAMA
Rıfat AKBIYIKLI
Özge AKBOĞA KALE
Sarven AKCELYAN
Burcu AKÇAY ALDANMAZ
Cihan Taylan AKDAĞ
Bekir AKGÖZ
Cem AKGÜNER
Erkan AKPINAR
Muhammet Vefa AKPINAR
Atakan AKSOY
Hafzullah AKSOY
Bekir AKTAŞ
Osman AKYÜREK
Uğurhan AKYÜZ
Alper ALDEMİR
Cenk ALHAN
Kayran ALTAN
Gülay ALTAY
Muhammet Gökhan ALTUN
Adlen ALTUNBAŞ
Yalçın ALVER
Mustafa M. ARAL
Ahmet ARGEŞO
Erdinç ARICI
Yalın ARICI
Musa Hakan ARSLAN
Okan ARSLAN
Deniz ARTAN İLTER
Deepankar Kumar ASHISH
Ayşegül ASKAN GÜNDOĞAN
Ali Osman ATAHAN
Hakan Nuri ATAHAN
Güzide ATASOY ÖZCAN
Ali Osman ATEŞ
Mustafa ATMACA
Özgür AVŞAR
Cem AYDEMİR
Ersin AYDIN
Serdar AYDIN
Ülker Güner BACANLI
Mehmet Nurullah BALCI
Selim BARADAN
Eray BARAN
Türkay BARAN
Efe BARBAROS
Bekir Oğuz BARTIN
Zeynep BAŞARAN BUNDUR
İrfan BATUR
Cüneyt BAYKAL
Mehmet BERİLGEN
Önder Halis BETTEMİR
Katrin BEYER
Niyazi Özgür BEZGİN
Ozan BİLAL
Turhan BİLİR
Senem BİLİR MAHÇİÇEK
Barış BİNİCİ
Jitendra BOTHARA
İlker BOZ
İlknur BOZBEY
Ali BOZER
Mehmet Bakır BOZKURT
Zafer BOZKUŞ
Zekai CELEP
Halim CEYLAN
Ömer CİVALEK
Barlas Özden ÇAĞLAYAN
Ferit ÇAKIR
Melih ÇALAMAK
Gülben ÇALIŞ
Süheyla Pelin ÇALIŞKANELLİ
Serdar ÇARBAŞ
Tevfik Kutay ÇELEBİOĞLU
Ahmet Ozan ÇELİK
Oğuz Cem ÇELİK
Ozan Cem ÇELİK
Hilmi Berk ÇELİKOĞLU
Mecit ÇETİN
Elif ÇİÇEK
Emin ÇİFTÇİ
Hüseyin ÇİLSALAR
Erdal ÇOKÇA
Turgay ÇOŞGUN
Ayşe DALOĞLU
Yakup DARAMA
Kutlu DARILMAZ
Alper DEMİR
Cem DEMİR
Hacımurat DEMİR
Selçuk DEMİR
Uğur DEMİR
Ender DEMİREL
Mehmet Cüneyd DEMİREL
Murat DİCLELİ
Seyyit Ümit DİKMEN
Ahmet Anıl DİNDAR
Gamze DOĞAN
Mustafa DOĞAN
Ünal DOĞAN
Marco DOMANESCHI
Gökhan DÖK
Cemalettin DÖNMEZ
Ebru DURAL
İsmail DURANYILDIZ
Cengiz DÜNDAR
Özgür EKİNCİOĞLU
Serkan ENGİN
Murat Altuğ ERBERİK
Ali ERCAN
Barış ERDİL
Şakir ERDOĞDU
Esin ERGEN PEHLEVAN
Uğur ERSOY
Yusuf Çağatay ERŞAN
Esra Ece ESELLER BAYAT
Müberra ESER AYDEMİR
Tuğba ESKİŞAR TEFÇİ
Abdullah GEDİKLİ
Ergun GEDİZLİOĞLU
Mehmet GENES
Ahmet Talha GEZGİN
Sadık Can GİRGİN
Zehra Canan GİRGİN
Michele GODIO
Saadet Gökçe GÖK
Tansu GÖKÇE
Serdar GÖKTEPE
Semih GÖNEN
Ali GÜL
Fazlı Erol GÜLER
Ilgın GÜLER
M. Fethi GÜLLÜ
Adil GÜLTEKİN
Fırat GÜMGÜM
Gürkan GÜNAY
Taylan GÜNAY
Lütfullah GÜNDÜZ
Samet GÜNER
Burcu GÜNEŞ
Oğuz GÜNEŞ
Mehmet Şükrü GÜNEY
Tuba GÜRBÜZ BÜYÜKKAYIKÇI
Aslı Pelin GÜRGÜN
Ercan GÜRSES
Tefarruk HAKTANIR
Soner HALDENBİLEN
Ömer Faruk HALICI
Hussein HAMADA
Ingo A. HANSEN
Emre HASPOLAT
Mustafa HATİPOĞLU
Lucas HOGAN
Sabriye Banu İKİZLER
Okan İLHAN
Erol İSKENDER
Medine İSPİR ARSLAN
Recep İYİSAN
Nuray Işık KABDAŞLI
Mehmet Rifat KAHYAOĞLU
Özkan KALE
Volkan KALPAKÇI
Muhammet KAMAL
Reza KAMGAR
Hakan Alper KAMİLOĞLU
Fatih KANTARCI
Armağan Fatih KARAMANLI
İlker KAZAZ
Saeid KAZEMZADEH AZAD
Mustafa Kubilay KELEŞOĞLU
Elçin KENTEL
Veysel Şadan Özgür KIRCA
Mehmet Anıl KIZILASLAN
Esat Selim KOCAMAN
Salih KOÇAK
Niyazi Uğur KOÇKAL
Baha Vural KÖK
Mete KÖKEN
Özgür KURÇ
Ali Osman KURUŞÇU
Muhammed Emin KUTAY
Akif KUTLU
Merih KÜÇÜKLER
Abdullah KÜRKÇÜ
Erol LALE
Jose LEMOS
Todd LITMAN
Faqih MAARIF
Müslüm Murat MARAŞ
Ali MARDANİ
Kasım MERMERDAŞ
Halit Cenan MERTOL
Mehmet Murat MONKUL
Nihat MOROVA
Yetiş Şazi MURAT
Sepanta NAIMI
Salih OFLUOĞLU
Fuad OKAY
Didem OKTAY
Derviş Volkan OKUR
Meral OLTULU
Şeref ORUÇ
Okan ÖNAL
Akın ÖNALP
Bihrat ÖNÖZ
Cihan ÖSER
Türkan ÖZBALTA
Yiğit ÖZÇELİK
Gökhan ÖZDEMİR
Zuhal ÖZDEMİR
Murat ÖZEN
Pelin ÖZENER
Ekin ÖZER
Hasan ÖZER
Hakkı Oral ÖZHAN
Hulusi ÖZKUL
Zeynep Huri ÖZKUL BİRGÖREN
Aşkın ÖZOCAK
Sadık ÖZTOPRAK
Baki ÖZTÜRK
Gözde Başak ÖZTÜRK
Onur ÖZTÜRK
Mustafa ÖZUYSAL
Nilüfer ÖZYURT ZİHNİOĞLU
Erhan Burak PANCAR
Seval PINARBAŞI ÇUHADAROĞLU
Elişan Filiz PİROĞLU
Bora POLATSU
Shehata E. Abdel RAHEEM
Selçuk SAATÇİ
Selman SAĞLAM
Mehmet SALTAN
Afşin SARITAŞ
Altuğ SAYGILI
Serdar SELAMET
Sercan SERİN
Nuri SERTESER
Emel SEYHAN
Halil SEZEN
Alper SEZER
Metin SOYCAN
Kurtuluş SOYLUK
Serdar SOYÖZ
Tayfun Altuğ SÖYLEV
Haluk SUCUOĞLU
Erol ŞADOĞLU
Zekai ŞEN
Burak ŞENGÖZ
Gülüm TANIRCAN
Serhan TANYEL
Mucip TAPAN
Ergin TARI
Yüksel TAŞDEMİR
Ali Şahin TAŞLIGEDİK
Kerem TAŞTAN
Hasan TATLI
Serdal TERZİ
Berrak TEYMUR
Hüseyin Onur TEZCAN
Mesut TIĞDEMİR
Salih TİLEYLİOĞLU
Onur Behzat TOKDEMİR
Nabi Kartal TOKER
Ali TOPAL
Cem TOPKAYA
Cenk TORT
Hasan TOSUN
Kamile TOSUN FELEKOĞLU
Gökçe TÖNÜK
Kemal Dirgen TÖZER
Nursu TUNALIOĞLU
Gürsoy TURAN
Kaan TÜRKER
Hasan Nuri TÜRKMENOĞLU
Cüneyt TÜZÜN
Mehmet Baran ULAK
Berna UNUTMAZ
Mehmet UTKU
Volkan Emre UZ
İbrahim Mert UZUN
Mehmet Seçil UZUNER
Deniz ÜLGEN
Mehmet Barış Can ÜLKER
Ali ÜNAY
Cüneyt VATANSEVER
Oral YAĞCI
Ahmet YAKUT
Erkut YALÇIN
Aslı YALÇIN DAYIOĞLU
Anıl YAZICI
Gökhan YAZICI
Cem YENİDOĞAN
Mehmet YETMEZ
Mehmet YILMAZ
Berivan YILMAZER POLAT
Ercan YÜKSEL
Ahmet Şahin ZAİMOĞLU
Abdullah Can ZÜLFİKAR

Turkish Journal of Civil Engineering (formerly Teknik Dergi)

Volume 36 Issue 2 Mart 2025

CONTENTS

Turkish Journal of Civil Engineering, 2025, 1-27, Paper 797, ***Research Article***

The Comparison of Fragility Curves of Moment-Resisting and Braced Frames Used In Steel Structures under Varying Wind Load

Abdulkadir OZALP[1*]
Hande GOKDEMIR[2]
Cihan CIFTCI[3]

ABSTRACT

In this study, the performance of two different steel structure types (moment-resisting frame and braced frame) under wind loading was compared by addressing the fragility curves of these structure types. To perform this comparison, the dimensions of the members of these structural systems were first determined. Then, nonlinear static pushover analyses were conducted to assess the performance levels of each frame type. After applying these analyses, time-history analyses were performed with 100 different wind loads for each varying equivalent mean wind speed. Afterwards, the probability of exceeding the predetermined structural performance limits of the structure types was determined using Monte Carlo simulation method. Finally, the results of the simulation method were used to adapt the maximum likelihood estimation method to obtain the fragility curves of the structures. To conclude, it has been revealed that the material cost of the structure doubles when diagonal elements are used, but the wind speed required for a 100% collapse probability to occur in the braced frame is twice as high compared to the moment-resisting frame.

Keywords: Performance based design, time history analysis, pushover analysis, load resistance factor design, fragility curve.

Note:
- This paper was received on November 29, 2022 and accepted for publication by the Editorial Board on July 27, 2024.
- Discussions on this paper will be accepted by May 31, 2025.
- https://doi.org/10.18400/tjce.1211905

1 Presidency of the Republic of Türkiye Directorate of Communications, Ankara, Türkiye
abdulkadir.ozalp@iletisim.gov.tr - https://orcid.org/0000-0002-8951-6841

2 Eskişehir Osmangazi University, Department of Civil Engineering, Eskişehir, Türkiye
handeg@ogu.edu.tr - https://orcid.org/0000-0003-0478-8133

3 Abdullah Gül University, Department of Civil Engineering, Kayseri, Türkiye
cihan.ciftci@agu.edu.tr - https://orcid.org/0000-0001-9199-6437

* Corresponding author

1. INTRODUCTION

Thanks to the advancing technology and production techniques, many different structures can be built today. In order to make these structures sustainable, the analysis and design of the structures are important. In the application of these analyses and designs, not only the stiffness values of the structures but also the external loads acting on the structures have an extremely important role. Among these external loads, hurricanes are one of the most destructive natural disasters that can cause serious damage to structures and loss of life due to the wind forces that they exert (especially for high-rise buildings to be the subject of this study). Meanwhile, this destructive effect of wind loads is also directly related to the geographical region where the structure is located. Since the size and distribution of wind loads vary according to geographical regions in the world, for example, according to the World Wind Map [1] given in Fig. 1, the wind speed is quite high on the east coast of the United States.

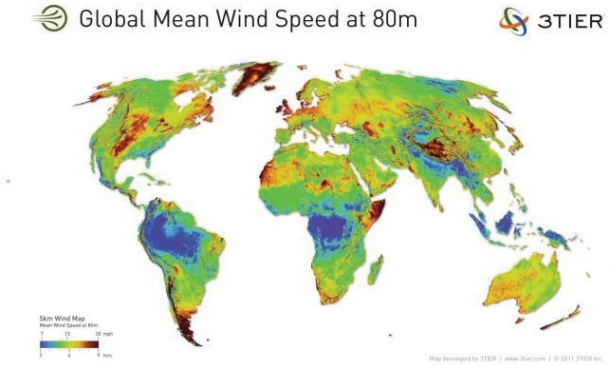

Figure 1 - The distribution of the average wind speed at 80 m height in the world

Hurricanes are common on the east coast of the US. In Fig. 2, wind speeds of office buildings located on the southeast and east coasts of USA are given [2]. According to the structural design regulations, these wind speeds are taken into account in the design calculations of buildings. However, in some cases, wind speeds can exceed these values, especially in hurricanes. The reason why such situations are ignored in regulations is that wind-caused natural events are not seen very often. However, in such situations, the effect of wind loads can be much more destructive. For example, Hurricane Sandy caused about $65 billion cost in property damage in the Ontario province of Canada and the northeastern coast of the United States [3]. Due to the severity, intensity, and effects of hurricanes in America, this country is chosen as the geography in this study.

Risk represents the probability of occurrence of hazardous events and the function of their social and economic impact. The search for more efficient methods to reduce risks and quantify these risks has led to the development of performance-based engineering approach. Performance-based engineering covers a wide place in the literature [4]. The main philosophy of the performance-based design is based on the material properties, type and dimensions of the selected building member to provide the targeted performance for the predetermined hazard level [5].

As mentioned above, in extraordinary situations such as natural disasters, the safety of buildings designed according to specific standards cannot be ensured [6]. If the force-displacement graph of the performance levels of the structures is known, it can be predicted when the structure will need to be evacuated, whether it can be used or not and when it will collapse. Then, performance-based analysis of buildings is of great importance in order to reduce the loss of life and property that may occur [7]. The fragility curves developed as a result of the performance-based analysis to predict the probability of collapse of the structures under varying wind speeds.

Fragility curves are cumulative distribution functions that enable to obtain the variability in the increment of probability of reaching damage states including engineering parameters such as story drift or exceeding these damage threshold limits [8–10].

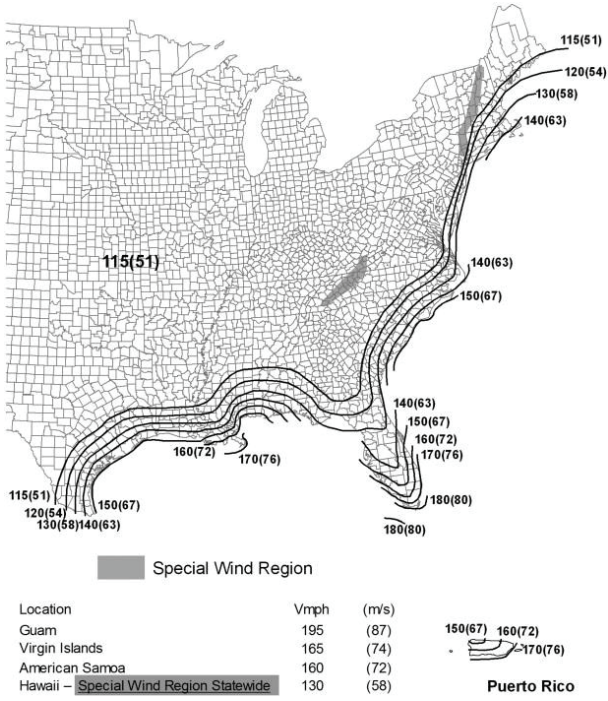

Figure 2 - Wind speeds of workplaces on the east and southeast coasts of the USA

The fragility analysis can be used not only in the field of structural engineering, but also in different areas such as the possibility of trees collapsing at extreme wind speeds. Ciftci et al. [11] explained an approach expected to be used to determine the probability of collapse of trees exposed to windstorm. In their study, this approach was exemplified by using two maple species in the state of Massachusetts, USA. As a result of this study, it has been shown that the applications related to the modeling of the collapse probability of open-grown trees using the probability-based fragility analysis and dynamic time history analysis make a unique contribution to the risk assessment of amenity trees. Lignos and Karamanci [8] discussed the development of the displacement-based and two-parameter fragility curves of steel structural

frames with concentric diagonal members designed for a seismic zone in their study. For steel diagonal elements subjected to periodic loading; drift-based fragility curves have been developed for three damage cases, including local buckling, bending buckling and loss of strength due to rupture of diagonals. The effect of material variety, cross-sectional shape of diagonals and loading protocols on drift-based fragility curves have been investigated. The effects of global and local slenderness ratios on the rupture ductility of steel diagonal elements with different shapes were investigated by using two-parameter fragility curves associated with geometric ratios such as the slenderness ratio together with the expected drift ratios when these previously defined three states occur. Studies have shown that the proposed fragility curves can be used to evaluate quickly the seismic fragility of frames with concentric diagonal members. Shin et al. [12] developed a seismic strengthening scheme with steel struts resistant to buckling for a 2-story steel frame structure designed only for dead loads by using the fragility contour method in their study. Then, using the fragility contour method, the seismic performance of the structure was assessed before and after the strengthening, and the improvement of performance level was evaluated in case of structural collapse or loss of bearing capacity of the structural members. Based on analytical studies, the most effective strut model for the strengthening scheme has been proposed based on various scenarios in terms of the weight of the developed strutting models. This study shows that the fragility contour method can be an effective tool for seismic evaluation and strengthening of structures. Sakurai et al. [13] investigated the contribution of the source of the variables in the moment-rotation characteristics of the connections to the unknowns in the frame deformations by using probability-based finite element analysis to compare the effect of bending stiffness of columns and beams and internal connection stiffness in their study. Probability- based finite element analysis was used to describe the system fragility that defines the probability of exceeding three limit states related to maximum lateral displacement, maximum inter-story drift ratio, and the elastic bending moment capacity which are the function of lateral load. In performance-based design, the effect of variables of internal connection stiffness on frame behavior is very important. The fragility analysis for frame deformation has shown that the coefficient on variation has a significant effect on the performance of frames (especially deformations of frames with complex geometry). Ramirez et al. [14] developed fragility functions that enable to calculate the damages that occur in column-beam connections with welded heads and bolted web built before 1994 in their study. While developing these functions, the experimental results of 51 column-beam connections tested within the scope of 10 different studies conducted in the last 26 years were taken into consideration. When developing the fragility curves, statistical unknowns related to factors based on the development of these curves as a small sample of the experimental results, as well as unknowns due to the difference between samples were taken into account. The results have shown that the developed fragility functions can be easily used by designers and those interested in this work in the performance-based evaluation process to calculate the probability of damage (yielding and crack development) in pre-Northridge column-beam connections which are part of moment-resisting frames after being hit by seismic waves of the considered earthquake scenario. The same functions can be easily used with the probability of exceeding a certain limit to calculate the maximum damage that may occur after the design and the most severe earthquake event considered. Kazantzi et al. [15] determined the arbitrarily chosen unknown system parameters that exist in nature of this structure in order to safely calculate the seismic performance of the 4-story moment-resisting steel frame in this study. Firstly, an advanced numerical model was created by transforming

the strength and plastic deformation properties of this system into three-dimensional parameters. Empirical relationships were derived from the experimental data used to model the periodic behavior of steel sections by using probabilistic distribution parameters including correlation between components. Finally, incremental dynamic analysis and Monte Carlo simulation were used to evaluate completely the seismic performance of the model under the effect of the unknowns. In this study, it was also examined which unknown model parameter would trigger negative demand-capacity correlation in the structural fragility assessment. Considering the structural quality levels (high, moderate and low) in FEMA P-58 and the moment-resisting frame examined, potential demand capacity correlation will likely result in the use of unconventional methods (e.g. fragility analysis) to calculate the fragility of local damage cases (especially where sub-standard quality control is applied during the construction phase) even though there is well agreement with structural demands obtained with or without considering unknown model parameters of very well-designed modern structures. Özel and Güneyisi [16] investigated the seismic reliability of the mid-rise reinforced concrete structures strengthened with eccentric steel braces by using fragility curves. As a result of the studies, four performance limit conditions (slight, moderate, major and collapse) were defined. The fragility curves for these limit states have been developed according to the peak ground acceleration with the log-normal distribution assumption. As a result of this study, improvements in the seismic performance of the mid-rise reinforced concrete structures which are strengthened with different eccentric braces have been achieved by using the formulation of fragility reduction. Kim and Shinozuka [17] examined the results of the fragility curve development for two typical bridge samples in southern California whose columns were reinforced with steel sheathing method against seismic effects in their study. Fragility curves were developed using a two-parameter log-normal distribution as a function of peak ground acceleration. Fragility curves of the bridge before reinforcement and post reinforcement were compared to quantify the improvement in fragility due to reinforcement. The improvement in fragility was determined quantitatively by comparing the median values of the fragility curves plotted before and after reinforcement in order to formulate the problem of developing fragility. The calculated analytical fragility curves corresponding to the damage cases and have an intuitive meaning regarding the design, strengthening and performance of the bridge for earthquake events that occurred in the past. In addition, it was expected that the experimental fragility curves can be much more reliable than the fragility curves derived by other means.

As a result of the literature review, while many studies on seismic fragility analyses of structures have been found, it has been observed that there are fewer studies on wind-induced fragility (e.g., Smith and Caracoglia 2011; Chuang and Spence 2017; Cui and Caracoglia 2019; Ma et al., 2021; Jiang et al., 2023). When these studies are examined, it is noticed that seismic fragility or wind-induced fragility analyses are based fundamentally on the same philosophy and contain great similarities, except for some details in their applications. The wind-induced fragility analysis was also used in this study as a tool to compare and discuss distinct steel structure types under wind loads. In this respect, although this study is not the first to present wind-induced fragility analysis for structures, it is unique in that it expresses and compares the performance-based behavior of two different steel structures (moment resisting and braced frames) under wind loads using fragility analysis. With this concept, in this study, these steel structural frames were designed as symmetrical office buildings having

six spans by considering the previous studies, since the torsion effect are not desired in the structures under consideration [18,19].

Therefore, it was decided to design the structure as an office building [20]. Considering the literature reviews, two different structural frame systems have been selected, namely, moment-resisting frame and braced frame [16, 18, 2 1–27]. These two frame types were used to provide stability in structures subjected to lateral loads. The fragility curves for these two frame types were plotted by using performance-based analysis method. Firstly, three different performance levels were determined for both frame types, namely, Immediate Occupancy (IO), Life Safety (LS) and Collapse Prevention (CP) using pushover analysis. Then, nonlinear time history analysis method was conducted for the frames depending on the varying wind speeds [28–30]. The number of frames exceeding the displacement limits of the performance levels was determined by comparing the displacement values obtained from the time history analyses with the limit displacement values of the previously determined performance levels. Finally, fragility curves were plotted by considering the number of frames exceeding the limit values of performance levels. According to the results, braced frames can withstand much higher wind speed than moment-resisting frames.

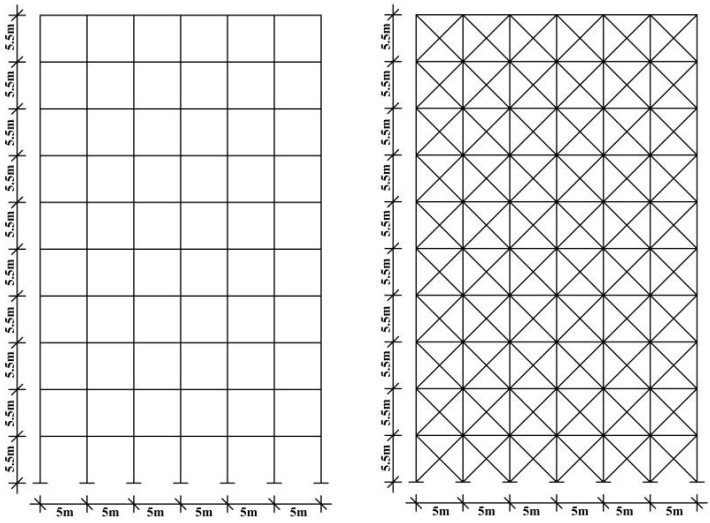

Figure 3 - Considered structural bearing systems a) Frontal view of moment-resisting frame b) Frontal view of braced frame

The focus of this study is to compare the fragility curves of two distinct structure types (the moment resisting frame and the braced frame). In order to apply the fragility analyses to these structural types, it is necessary to select a place corresponding to some assumptions required for all the analyses. The northeastern part of the USA was chosen for the case studies of this research for two reasons. First, this region on earth are often exposed to strong winds. The second reason is to utilize the existing knowledge of the authors, because some of the assumptions used in synthetic wind generation have been used previously for this region.

2. METHODOLOGY

This research contains a case study on the comparison of the fragility curves of two different structural systems (moment-resisting and braced systems) subjected to wind loading. The implementation of these fragility analyses is addressed in the three subtitles of this section that explain the three main steps. As the first step, the cross-sectional areas of the members had already been designed by considering dead loads, live loads, and wind loads. To give more details, the sections for columns, beams, and braces were roughly determined with the preliminary design by considering the live load and wind loads. After the section selections had been made, the load combinations determined according to ASCE 7-10 Section 2.3.2 were defined in the models for each structural system. Then, the design of the sections was finalized using the tool of section checks in the SAP2000 packaged software according to the American Steel Structure Institute Load and Resistance Factor Design (AISC-LRFD). In the second step, the capacity calculations of two structural systems were done using pushover analyses. For these pushover analyses, the needed critical rotations and displacements of the structural members with known cross-sectional areas were found for three performance levels: IO (immediate occupancy), LS (life safety), and CP (collapse prevention). Then, it was revealed that the beams for the moment-resisting system and the braces for the braced system were in charge of controlling all these performance levels, according to the pushover analyses. As the third step, these critical values of the performance levels were used as the limitations of the fragility analyses of the two structural types to be compared with each other.

2.1. A Case Study of Two Structural Systems

In this study, two different structural systems were used, namely the moment-resisting frame and the braced frame (Fig. 3). When a tal building is designed, the time required for analysis can be very long. Therefore, a 10-story steel frame with 5.5 m story height (total height 55 m) was chosen. While making this choice, the Home Insurance Building which is generally regarded as the world's first skyscraper, built in 1885 in Chicago, America and has a 10-story steel frame was taken into consideration [31]. The structural bearing systems used have 6 spans of 5 m length.

Considering the literature on braced frames, in some studies [16,32], diagonal elements were used only in selected bays of the structures, while in others [33–36], they were used in each bay. In this study, as in the examples given above, diagonal members were used in each bay of the braced frame structure. In addition, the column-beam connections used in these braced structures were modeled as pinned joints. Therefore, the lateral force resisting system in braced frames was provided only by the diagonal members used in each bay. In order to have the consistency for the moment resisting frame (MRF) structures with the braced ones, the lateral force resisting system of the MRF structures was provided by the fixed connections at all column-beam joints.

The architecture of the building is designed to be symmetrical as an office building. The spaces in the building (stairwells, elevator shaft,s etc.) are not taken into account. It was assumed that glass was used as facade material in the building. The weight of this material was ignored. It has been determined that the natural frequencies of the buildings are greater than 1 Hz in both cases, whether they have glass facade or not. For this reason, structures displace rigid behavior in these two cases. In this respect, the effect of using facade on the

lateral dynamic behavior of the structures has been neglected, and the structures were modeled using only structural elements.

As it can be seen in Fig.3, considering that the structural system elements and the supports at the base are symmetrical and also that the vertical wind load distribution symmetrically acts on the buildings for each bay, it was decided to analyze these building systems in 2D instead of 3D. In addition, it takes a long time to analyze the structures in three dimensions due to the large number of analyses to be made. Therefore, considering the literature reviews, the structures were modeled and analyzed as two dimensional systems [15]. SAP2000 was used to structural modeling [9,37,38].

As can be seen from Fig. 2, the highest wind speed belongs to Puerto Rico. However, since the wind speed to be applied in the fragility analysis will be above this value, there is no drawback in choosing the city of Boston. The basic wind speed for the city of Boston has been calculated as 62.14 m/s (Fig. 2). Since the structures used are the main wind force resisting systems, wind directionality factor K_d was chosen as 0.85, the exposure category as B, topographic factor K_{zt} as 1.0, wind impact factor G as 0.85, internal pressure coefficient GC_{pi} as +0.18, external pressure coefficient Cp for the windward wall as 0.8, and the C_p for the leeward walls as -0.5, respectively (Table 1).

Table 1 - Parameters used in calculating the wind loads affecting on the frames

K_d	0.85
Exposure Category	B
K_{zt}	1.0
G	0.85
GC_{pi}	0.18

Design wind pressures (see ASCE 7-10 Eq. 27.4-1) and velocity pressures (see ASCE 7-10 Eq. 27.3-1) were separately calculated for windward and leeward directions by using parameters listed in Table 1. For windward direction, the parameter K used in these calculations depends on height. For this reason, the vertical wind profile in windward direction has a non-uniform distribution as shown in Fig. 4. On the other hand, the vertical profile in leeward direction has uniform distribution because the K parameter has a constant value for this direction. In addition, for the calculations of the design wind pressure values in the windward and the leeward directions, the wind speed (V) values come from the wind speed data, which are synthetically generated for each mean speed in the scope of fragility analyses.

After determining the distributed wind load which exerts on buildings, characteristic live loads of the floors were determined according to ASCE 7-10 Table 4-1. Since the buildings to be used in the analysis were designed as office buildings, the characteristic live loads of these structures had been chosen as 2.40 kN/m^2 [39].

After determining the dead loads, live loads and wind loads for the structures, the building was modeled using Sap2000 [37]. Firstly, the geometrical properties of the structure were

determined. Then, the material properties were obtained. The most commonly used structural steel grades are ASTM A36 and ASTM A992 steels [40]. Structural steel types commonly used in America nowadays are produced according to ASTM A992 standard, which has higher yield and tensile strength than A36 steel [33]. Considering the literature review, the steel grade to be used in the buildings was considered as ASTM A992 [41]. The modulus of elasticity is 200 GPa, Poisson ratio is 0.3, shear modulus is 79.3 GPa, weight per unit volume is 76.9729 kN/m^3, mass per unit volume is 7.849 kN/m^3, minimum yield stress is 345 MPa and minimum tensile stress is 450 MPa for ASTM A992 steel.

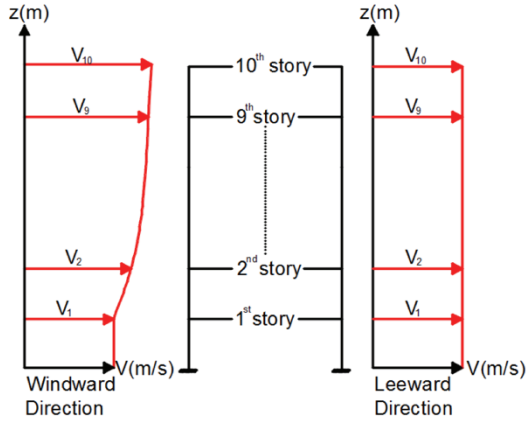

Figure 4 - Wind speed distribution for windward and leeward direction

Then the sections for columns, beams and braces were selected. Since the shear center does not coincide with the center of gravity of the section in singly symmetric double angle and T profiles, torsion effect may occur in these sections. In combined profiles, the compressive strength is affected by the shear transmission strength of the fasteners connecting the elements and the shear resistance of these fasteners [42]. W profile was selected for columns, beams and braces, considering the literature review [8,43]. The section chosen for the columns was W 21x111, for the beams was W 14x53, and for the braces was W 8x67.

After the section selections had been made, three different load models were defined as dead load, live load and wind load.

Nonlinear time history analysis method was used to examine the time-varying effect of loads during the modal analysis. Time history analysis can be conducted by using modal analysis or direct integration method [44]. In this work, eigenvectors were selected. However, modal nonlinear analysis gives better results with Ritz vectors [45]. For this reason, the direct integration method was used for time history analyses.

After the required loads were applied on the structural systems, the load combinations determined according to ASCE 7-10 Section 2.3.2 were defined and the analyses were conducted accordingly these combinations. The load combinations defined are given below [39].

$$1.4D \tag{1}$$

$$1.2D+1.6L+0.5S=1.2D+1.6L(S=0) \tag{2}$$

$$1.2D+1.3W+0.5L+0.5S=1.2D++1.3W+0.5L(S=0) \tag{3}$$

$$0.9D+(1.3W\ or\ 1.0E)=0.9D+1.3W(E=0) \tag{4}$$

$$0.9D-(1.3W\ or\ 1.0E)=0.9D-1.3W(E=0) \tag{5}$$

where, dead load is denoted by D, live load by L, snow load by S, earthquake load by E and wind load by W, respectively.

Then, considering the literature reviews, section checks were performed according to the American Steel Structure Institute Load and Resistance Factor Design (AISC-LRFD) method by using the SAP2000 software [46,47].

2.2. Capacity Calculation of Structural Systems

The capacity calculation of the selected structural systems was made by using pushover analysis [28,48, 49]. By applying this method, the structures were subjected to nonlinear static pushover analysis, and the nonlinearity was provided by assigning plastic hinges to the structural elements. The material nonlinear behavior of the elements was modeled by utilizing plastic hinges specified in the FEMA 356 guidelines. According to this regulation, while the plastic hinges of the columns and beams can be determined by moment - rotation relationships, the plastic hinge of the brace members can also be defined using force displacement relationships. The pre-existence of these mechanical relationships in the SAP-2000 program as a default setting provided great convenience for the implementation of this investigation. Since it was possible to obtain the detailed information and values regarding these relationships from the default settings in the SAP-2000 program, it was thought that there is no need to provide them in this text.

In this analysis method, the lateral load model distributed along the height of the structure was used. These lateral loads were then monotonously increased until the structure collapsed or reached the target displacement. Pushover analysis is a simple option to calculate the resistance capacity beyond the elastic region and can be used to determine potential weak zones in the structure [50]. Regarding the lateral load pattern used in pushover analyses, different loading patterns show only a slight change in performance in regular buildings (Abhilash et al. 2009). That is why the equivalent lateral force distribution utilized in FEMA-273 was arbitrarily selected for the pushover analyses addressed in this investigation.

Although two main design criteria are typically considered in ultimate bearing capacity methods (functionality limit, strength limit), there are several design criteria in performance-based design (IO, LS, CP).

It is inevitable for steel structural systems to exhibit nonlinear behavior under load due to the large ductility of steel material. In this regard, pushover analyses are among the most

frequently used techniques in the literature for the performance of these steel structures, as they are a type of nonlinear static analysis [51, 52]. Firstly, plastic hinges for structural members were defined according to ASCE/SEI 41-13 [53] to conduct this analysis. Since columns were mostly affected by axial force and moment, plastic hinges were defined to carry axial force and moment. As beams were mostly affected by moment, plastic hinges were defined to carry moment only. Because braces were only exposed to axial force, the plastic hinges were defined to carry only axial force. Additionally, in this study, the geometric nonlinearity of the pushover and time history analyses was carried out by taking into account P-Delta effects.

The displacement control was performed according to the joint at the top left corner of the frames (Figs. 5(a)-6(a)). As a result of the analysis, pushover curves of the moment- resisting frame and braced frame were obtained (Figs. 5(b)-6(b)). It was concluded that the braced frame started to lose its resistance after 7684.7 kN and the maximum displacement value without occurring collapse for the joint point at the top left corner is 0.085 m from Fig. 5(b). It was also concluded that the moment-resisting frame began to lose its bearing strength after 1651.9 kN and the maximum displacement value without occurring collapse for the joint point at the top left corner was 0.903 m from Fig. 6(b).

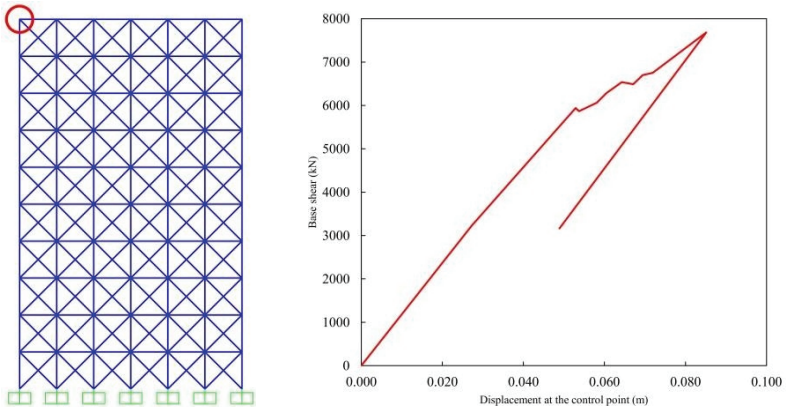

(a) (b)

Figure 5 - Pushover analysis results for the braced frame a) The joint where the displacement is checked in the pushover analysis b) The pushover curve of the structure

When Fig. 5(b) and Fig. 6(b) are compared, it is seen that braced frame can carry more load than the moment-resisting frame, while the maximum displacement value of the moment-resisting frame is greater. This shows that although the strength of braced frame is higher, the moment-resisting frame is more ductile.

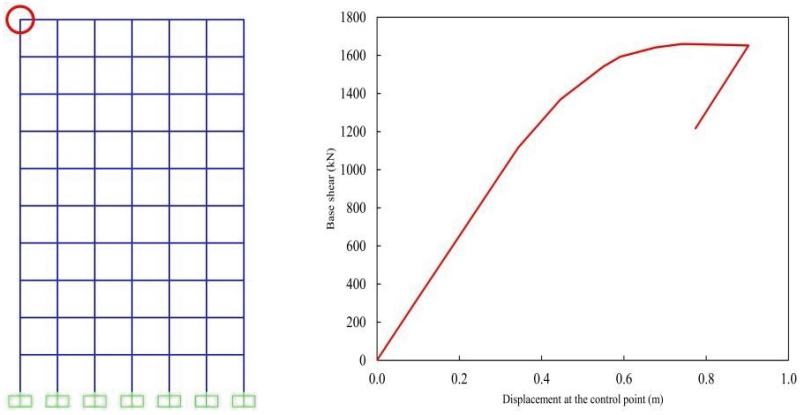

(a) (b)

Figure 6 - Pushover analysis results for the moment resisting frame a) The joint where the displacement is checked in the pushover analysis b) The pushover curve of the structure

After the pushover curves of both frames were obtained, structural performance levels were determined on these curves according to ASCE/SEI 41-13 [53]. These levels were divided into three categories as IO, LS and CP Performance levels and were determined by the levels of plastic rotation angles at the beams, and the plastic deformations at the braces according to the standard of ASCE/SEI 41-13 [53]. Acceptance criteria for plastic rotation angles of the beams and plastic deformations of the braces were determined according to equations given in the relevant specification. Table 2 shows these rotation angles and deformations corresponding to the structural members. According to Table 2, the performance levels of IO, LS, and CP occur beyond 0.003, 0.026, and 0.032 in radians respectively, for the beam members. For the brace members, IO, LS, and CP levels start with the plastic deformations having the values 0.002, 0.032, and 0,039 in meters, respectively.

Table 2 - Plastic rotation angles and deformations at the relevant structural members with the performance levels

Performance Levels	Plastic Rotation Angles for Beam Members (rad)	Plastic Deformations for Brace Members (m)
IO	0.003	0.002
LS	0.026	0.032
CP	0.032	0.039

As a result of the performed pushover analysis, it was observed that minor yielding occurred in one beam in the fourth step for the moment-resisting frame. Therefore, the fourth step was determined as the IO performance level. In the fifth step, it was observed that few beams had small-scale yielding but they could still carry shear force. Therefore, the fifth step was determined as the LS performance level. In the sixth step, it was observed that yielding started in one of the columns on the bottom floor of the building and yielding occurred in many beams. Therefore, the sixth step was determined as the CP performance level.

In the braced frame, it was observed that small-scale yielding occurred in one brace in the first step. Therefore, the first step was determined as the IO performance level. In the second step, it was observed that small-scale yielding occurred in few braces, and there was a sudden decrease in the lateral strength of one brace, but it did not lose its strength completely. Therefore, the second step was determined as the LS performance level. In the sixth step, it was observed that there was significant yielding and sudden strength loss in many braces, and small-scale yielding occurred in one of the columns on the bottom floor of the building. Therefore, the sixth step was determined as the CP performance level. In the Table 3, required force and displacements are shown in order for the moment-resisting frame to reach the predetermined performance levels. According to Table 3, in the fourth step of the moment-resisting frame, the displacement of the joint at the upper left corner of the frame was 0.343 m, the corresponding base shear is 1116.6 kN, in the fifth step the displacement of the joint at the top left corner of the frame is 0.446 m, the corresponding base shear is 1368.8 kN, In the sixth step, the displacement of the joint at the top left corner of the frame reached 0.550 m, and the related base shear equaled 1541.9 kN.

Table 3 - Displacement values occurring at the performance levels of the moment-resisting frame

Step	Displacement (m)	Base Shear (kN)
0	0.000	0.0
1	0.100	327.4
2	0.200	651.5
3	0.300	977.1
4	0.343	1116.6
5	0.446	1368.8
6	0.550	1541.9
7	0.591	1592.6
8	0.677	1641.6
9	0.740	1659.7
10	0.755	1659.3
11	0.866	1654.2
12	0.903	1651.9
13	0.774	1216.6

In the Table 4, the required force and displacements are shown in order for the braced frame to reach the predetermined performance levels. According to Table 4, in the first step of the braced frame, the displacement of the joint at the upper left corner of the frame is 0.027 m, the corresponding base shear is 3226.2 kN, in the second step the displacement of the joint at the upper left corner of the frame is 0.053 m, the related base shear is 5941.3 kN, in the sixth step, the displacement of the joint at the top left corner of the frame is 0.064 m and the base shear is 6536.3 kN.

Table 4 - Displacement values occurring at the performance levels of the braced frame

Step	Displacement (m)	Base Shear (kN)
0	0.000	0.0
1	0.027	3226.2
2	0.053	5941.3
3	0.054	5867.0
4	0.058	6061.3
5	0.061	6286.7
6	0.064	6536.3
7	0.067	6489.8
8	0.069	6700.1
9	0.072	6751.4
10	0.085	7684.7
11	0.049	3163.8

2.3. Obtaining Fragility Curves

Fragility functions can be plotted in a single step for the whole structure or in two steps by considering the entire structure and beam-column joints separately [14]. In this study, the fragility curve was created for the entire structure in one step.

In order to plot the fragility curve, firstly, wind models were created depending on the probability. The Ochi-Shin equation was used to determine the wind spectrum for Boston located on the Atlantic ocean coast (Eq. (6)).

$$S_{V_w}(\omega) = \frac{CV_w^2 F_g}{\omega} \tag{6}$$

where, wind spectral density is denoted by $SV_w(\omega)$, surface drag coefficient which is related to surface roughness is denoted by C, mean wind speed (m/s) at 55 m height is denoted by V_w, frequency of wind (rad/s) is denoted by ω and gust factor is denoted by F_g. The Ochi-Shin equation is also very useful in the condition of modifying the surface drag coefficient

which is a physical and singular parameter. Therefore, this equation was chosen while creating the probability based wind model. The C value was modified to use in the considered building systems. F_g value is calculated according to Eq. (7) [11].

$$F_g = \begin{cases} 583((1.592\omega)/V_w) & 0 \le \omega \le 0.001885V_w \\ \dfrac{420((1.592\omega)/V_w)^{0.7}}{(1+((1.592\omega)/V_w)^{0.35})^{11.5}} & 0.001885V_w \le \omega \le 0.0628V_w \\ \dfrac{838((1.592\omega)/V_w)}{(1+((1.592\omega)/V_w)^{0.35})^{11.5}} & 0.0628V_w \le \omega \end{cases} \quad (7)$$

The modification process included the calculation of the spectral densities of the changes in wind speed with time in the city of Boston. Then, these spectra were compared with Eq. (6) and defined as in Eq. (9) by changing the C value (Eq. (8)) defined initially [11].

$$C = (750 + 69V_w)(1.0 * 10^{-6}) \quad (8)$$

$$C = (750 + 69V_w)(3.7 * 10^{-6}) \quad (9)$$

Then, the spectral densities of the data obtained from the field were compared with the spectral densities plotted using the modified Ochi-Shin equation. Each of these spectra showed the wind spectrum experimentally generated based on observations of wind records in a very narrow mean wind speed range, and the spectrum plotted by the modified Ochi-Shin equation corresponding to the same average wind speed range. After making these comparisons, wind speed varying with 0.05 s increments in the range of 40 m/s ≤ V_w ≤ 220 m/s was generated for the reference height (55 m) for finite element model [11].

To produce wind speed data, firstly, for each V_w (wind speed) increase, 100 random wind data were generated by substituting Eq. (9) and Eq. (7) in Eq. (6) and using the spectral method shown in Eq. (10) [11]

$$V_w^G(t) = \sum_{r=1}^{n} A_r \sin(\omega_t t) + B_r \cos(\omega_t t) \quad (10)$$

Then, the Nataf model was used to transform Gaussian data into time history data series with log-normal marginal distribution which is the most widely used wind speed record distribution type (Eq. (11)).

$$V_i = \frac{\mu x_i^2}{\sqrt{\mu x_i^2 + \sigma x_i^2}} \exp\left(V_i^G \sqrt{\ln\left(\frac{\mu x_i^2 + \sigma x_i^2}{\mu x_i^2} \right)} \right) \quad (11)$$

where, Gaussian variable is denoted by V_i^G, mean is denoted by σx_i^2 and variance is denoted by μx_i. Although the Nataf model distorts the spectrum while transforming it from the

Gaussian space to the non-Gaussian space, this distortion was neglected because it was small (<1%) [11]. One of these time history data is shown in Fig. 7. From this figure, it is seen that wind speeds change in intervals of 0.05 seconds.

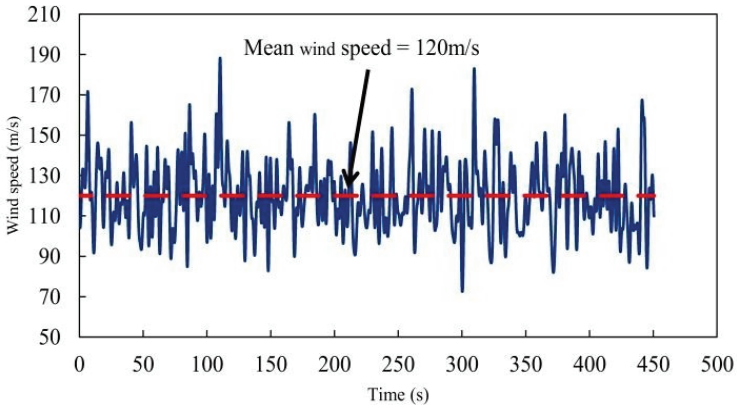

Figure 7 - One of the 100 data generated for an average wind speed of 120 m/s

After generating the wind data, nonlinear time history analyses were conducted on both frames using these data. The mean wind speed values varying between 40-100 m/s were used when conducting time history analyses for moment-resisting frames while the mean wind speed values varying between 70-220 m/s were used when conducting time history analyses for braced frames. Since the time values changed in the range of 0-450.5 seconds in increments of 0.05 seconds, time history analyses were conducted in 9010 steps and 100 analyses were conducted for each mean wind speed. For all these analyses, the damping ratio was used to be 0.02, which is consistent with the literature [54,55].

Then, the number of frames reaching or exceeding predetermined performance levels was calculated and the probability of reaching or exceeding these performance levels for both frames was determined by using these data.

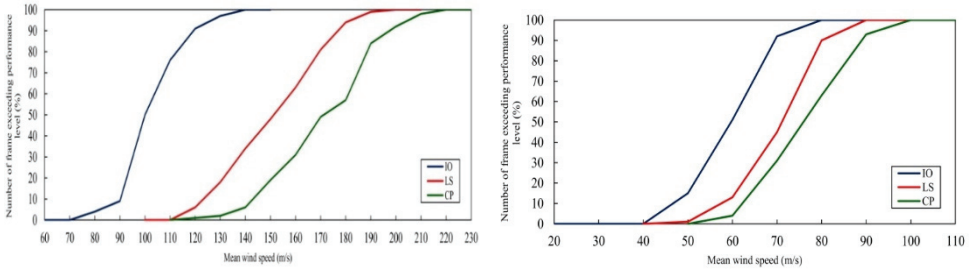

Figure 8 - Number of frames exceeding determined performance level vs mean wind speed plot a) Graph for braced frames b) Graph for moment-resisting frames

As a first step to determine these possibilities, graph of mean wind speed vs. number of frames reaching or exceeding the predetermined performance levels for both frame types was plotted using the Monte Carlo (MC) method. For structures with detectable level of failure probability, MC simulation can give precise results to a certain extent [18]. For this reason, in this study, the possibility of reaching or exceeding the predetermined performance levels of the structures was calculated using MC simulation. The number of frames exceeding the predetermined performance level vs. mean wind speed graph obtained by MC method was shown in Fig. 8.

After determining the probability of exceeding the performance levels for the frames depending on the wind speed, the fragility curves for these performance levels were plotted as a last step. When defining the fragility functions, the log-normal cumulative distribution function was generally used (Eq. (12)) [9,10,38,56].

$$P(C \mid IM = x) = \Phi\left(\frac{\ln(x/\theta)}{\beta}\right) \tag{12}$$

where, possibility of collapse the structure for wind speed corresponding to IM = x is denoted by P(C | IM = x), intensity measure is denoted by IM, standard normal cumulative distribution function is denoted by Φ function, mean of fragility curve (IM level which has 50% possibility of collapse) is denoted by θ and standard deviation of ln(IM) is denoted by β. In order for Eq. (12) to be adapted to the structure under consideration, the θ and β values obtained from the structural analysis results should be calculated. These parameters were shown as θ̂ and β̂ in calculations [57]. Generally, two different statistical approaches are used to calculate the parameters obtained from the data. The first method is the moments method, which aims to find parameters that show the same sample moment (mean, standard deviation, etc.) distribution of the observation data. The second method is the maximum likelihood estimation (MLE) method, which aims to find the parameters that are distributed in a way to provide the maximum probability of occurrence of the obtained observation data [57].

Since the wind speed used at each intensity measure level varies, the analyst may not fully observe the percentage increase in the collapse probability of the building with the increase in the intensity measure although it is known that the possibility of collapse of the structure will increase with the increase of the intensity measure. The suitable fitting technique for such data is the MLE method used by many researchers [57]. Therefore, the fragility curves were obtained using the MLE method. In this method, the structural analyses generate the number of collapse out of the total number of wind speeds for each IM = x_j intensity measure level. Since the analysis data was obtained at more than one intensity measure level, the likelihood of the whole data set was calculated by the following formula (Eq. (13)).

$$Likelihood = \prod_{j=1}^{m} \binom{n_j}{z_j} \Phi\left(\frac{\ln(x_j/\theta)}{\beta}\right)^{z_j} \left(1 - \Phi\left(\frac{\ln(x_j/\theta)}{\beta}\right)\right)^{n_j - z_j} \tag{13}$$

where the number of wind speed is denoted by nj, number of occurring collapses is denoted by zj and level of intensity measure is denoted by xj.

In order to calculate the fragility function parameters, the likelihood function in Eq. (13) should be maximized. This operation is equivalent to maximizing the logarithm of the likelihood function (Eq. 14). Thus, it can be easier to find the θ̂ and β̂ parameters.

$$\{\hat{\theta},\hat{\beta}\} = \arg\max_{\theta,\beta} \sum_{j=1}^{m} \left\{ \ln\left(\frac{n_j}{z_j}\right) + z_j \ln \Phi\left(\frac{\ln\left(x_j/\theta\right)}{\beta}\right) + (n_j - z_j)\ln\left(1 - \ln\Phi\left(\frac{\ln\left(x_j/\theta\right)}{\beta}\right)\right)\right\} \quad (14)$$

Fragility curves were plotted in computer environment for three different performance levels (IO, LS, CP) of moment-resisting frames and braced frames, depending on the MC data.

3. RESULTS AND DISCUSSIONS

As mentioned before, this research was conducted as a case study focusing on the comparison of the fragility analyses of two distinct structure types (moment-resisting and braced frames). Therefore, the results obtained with this research belong to the two different structural systems discussed within the case study, and these results are only recommended for other structural systems but not inclusive of all. Additionally, to repeat, it can be stated that this study focused on comparing the fragility curves of two different structural systems (moment-resisting and braced frames). For this comparison, all the mechanical properties of the beams in each system, such as the amount and cross-sectional areas (W14x53), were assigned the same. This situation was also true for columns (W21x111). Both structural systems offer only one different feature among themselves. This difference is that, while there are no cross members in the moment-resisting frame system, which can carry moments at the joints, the braced frame system has those cross members that carry axial loads.These structural frame systems have been analyzed as 2D for this study. Therefore, the differences between the fragility curves of these structural systems, which are equivalent in terms of all their features but differ in only one aspect, have explored and revealed more consistently and accurately.

The data obtained by MC and MLE method are shown in Fig. 9. In this figure, red line shows the results obtained from the calculations made according to the MLE method, while the blue points show the results obtained from the calculations made according to the MC method.

According to Fig. 9(a), no frame exceeds the IO performance level for 40 m/s average wind speed in moment-resisting frames. In addition, it is also seen that all frames exceed IO performance level for 80 m/s when MC method is used in calculations and for 100 m/s when MLE is used in calculations.

According to Fig. 9(b), no frame exceeds LS performance level for 40 m/s average wind speed in moment-resisting frames. In addition, it is also seen that all frames exceed LS performance level for 90 m/s when MC method is used in calculations and for 100 m/s when MLE is used in calculations.

According to Fig. 9(c), no frame exceeds CP performance level for 40 m/s average wind speed in moment-resisting frames. In addition, it is also seen that all frames exceed CP performance level for 100 m/s when MC or MLE method is used in calculations.

According to Fig. 9(d), no frame exceeds IO performance level for 70 m/s average wind speed in braced frames. In addition, it is also seen that all frames exceed IO performance

level for 140 m/s when MC method is used in calculations and for 150 m/s when MLE is used in calculations.

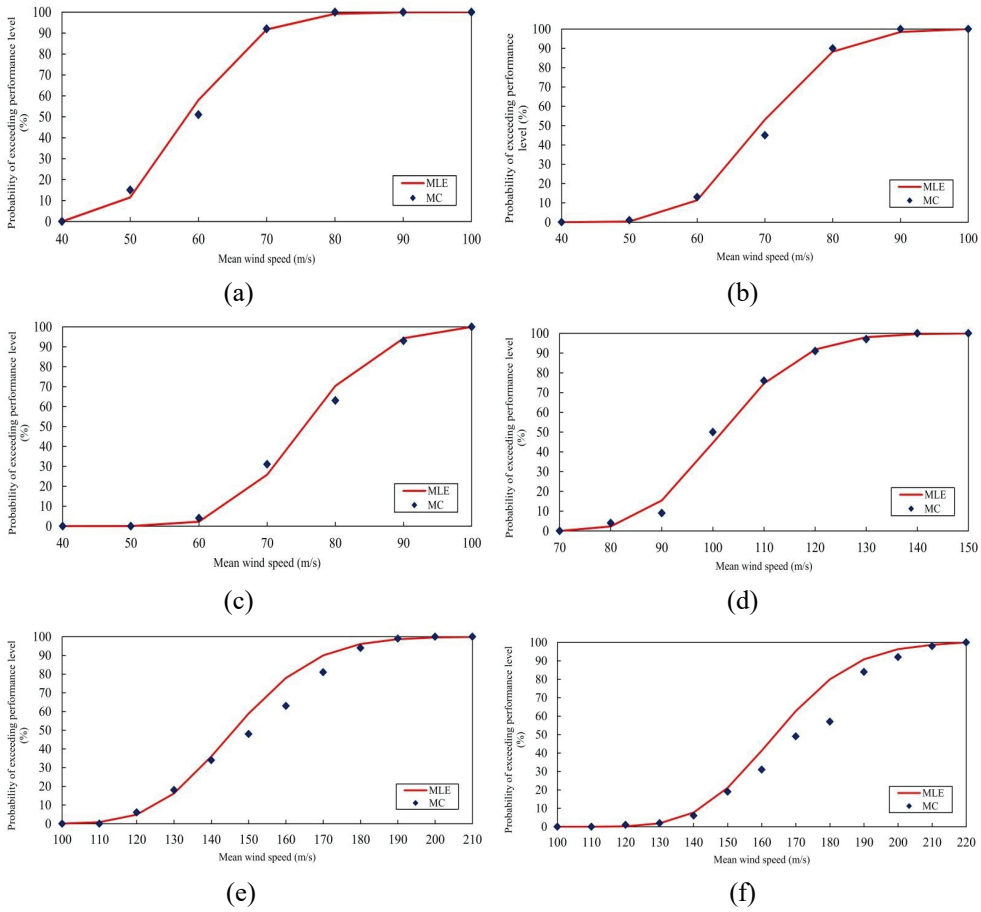

Figure 9 - Plots for probabilities of exceeding predetermined performance levels depending on changing wind speeds for frames a) Probability of exceeding IO performance level for moment-resisting frames b) Probability of exceeding LS performance level for moment-resisting frames c) Probability of exceeding CP performance level for moment-resisting frames d) Probability of exceeding IO performance level for braced frames e) Probability of exceeding LS performance level for braced frames f) Probability of exceeding CP performance level for braced frames

According to Fig. 9(e), no frame exceeds LS performance level for 100 m/s average wind speed in braced frames. In addition, it is also seen that all frames exceed LS performance level for 200 m/s when MC method is used in calculations and for 210 m/s when MLE is used in calculations.

According to Fig. 9(f), no frame exceeds CP performance level for 110 m/s average wind speed in braced frames. In addition, it is also seen that all frames exceed CP performance level for 220 m/s when MC or MLE method is used in calculations.

In addition, yielding starts and then collapse occurs in the mean wind speed range of 40-100 m/s in the moment-resisting frame, while yielding starts and then collapse occurs in the wind speed range of 70-220 m/s in the braced frame. Considering that hurricanes have a variable wind speed range, it can be stated that it is more advantageous if the process between yielding and collapse of structures takes place in a wider wind range.

Table 5 - Comparison of performances of the moment-resisting frame and braced frame under varying mean wind speeds

Mean wind speed (m/s)	Number of Analyses	Probability of exceeding performance level according to MLE method (%)					
		Braced frame			Moment-resisting frame		
		IO	LS	CP	IO	LS	CP
40	100	0.00	0.00	0.00	0.00	0.00	0.00
50	100	0.00	0.00	0.00	11.51	0.32	0.01
70	100	0.00	0.00	0.00	91.75	53.10	25.86
80	100	2.25	0.83	0.02	99.21	88.31	70.37
100	100	44.62	0.00	0.00	100.00	100.00	100.00
150	100	100.00	58.89	21.18	100.00	100.00	100.00
210	100	100.00	100.00	98.72	100.00	100.00	100.00
220	100	100.00	100.00	100.00	100.00	100.00	100.00

Table 6 - Quantity calculation for moment-resisting frame

Steel section type	Number of steel section used	Cross sectional area (m^2)	Total length (m)	Density (kg/m^3)	Total weight of steel used (kg)	Total weight of structure (kg)
W14*53	60	0.010064	300	7849.1	23698	87451
W21*111	70	0.021097	385	7849.1	63753	
W14*53	60	0.010064	300	7849.1	23698	
W21*111	70	0.021097	385	7849.1	63753	

Table 7 - Quantity calculation for braced frame

Steel section type	Number of steel section used	Cross sectional area (m^2)	Total length (m)	Density (kg/m^3)	Total weight of steel section used(kg)	Total weight of structure (kg)
W14*53	60	0.010064	300	7849.1	23698	176439
W21*111	70	0.021097	385	7849.1	63753	
W8*67	120	0.01271	892	7849.1	88988	
W14*53	60	0.010064	300	7849.1	23698	

Performances of moment-resisting frame and braced frame under varying mean wind speeds are compared in Table 5. According to this table, moment-resisting frame exceeds the performance levels IO, LS and CP with 100% probability for 100 m/s mean wind speed. Braced frame exceeds the IO performance level with 100% probability for 150 m/s mean wind speed, LS performance level with 100% probability for 210 m/s mean wind speed, and CP performance level with 100% probability for 220 m/s mean wind speed. In addition, the performance level IO, LS and CP for the moment-resisting frame is exceeded at the same mean wind speed. This indicates that the moment resisting frame, which is addressed in this study, performs more brittle behavior than the other structure. Finally, quantities of both frame types were calculated in order to form an opinion in terms of cost-performance. As a result of the quantity calculations, the total weight of the moment-resisting frame was found to be 87451 kg, and the total weight of the braced frame was found to be 176439 kg (Tables 6-7).

The sample size-a crucial boundary condition parameter for Monte Carlo simulations-has a significant effect on having smoother fragility curves calculated in the article. In this context, increasing the sample size used in each fragility curve calculation would have made the results more stable. However, in spite of this benefit, a serious drawback would have also come to light. This drawback was that increasing the sample size would significantly increase both the workload and the amount of time required for the fragility analyses [58]. However, as can be understood from the title of this study, this article is actually about the comparison of the performances of different structure types under wind load, and the fragility curves have been used as only a tool for these comparisons. In this regard, the authors think that the sample size used for these comparisons is sufficient for its objective. As a matter of fact, the literature also contains several studies with smaller sample sizes than the sample size utilized in this study.

4. CONCLUSIONS

In this study, the efficiency of of braces was investigated by comparing the fragility curves of moment-resisting and braced frames under wind loads. As a result of these comparisons, it has been seen that using diagonal members is of great importance in terms of improving structural performance. At the different performance levels (IO, LS, CP), the fragility curves of the braced frame have a broader distribution feature than those of the moment resisting frame in respect to the mean wind speed values.

In addition to all these, yielding starts and then collapse occurs in the mean wind speed range of 40-100 m/s in the moment-resisting frame, while yielding starts and then collapse occurs in the wind speed range of 70-220 m/s in the braced frame. Considering that hurricanes have a variable wind speed range, it can be stated that it is more advantageous if the process between yielding and collapse of structures takes place in a higher wind range.

When the total weight of the two frame types used is compared, it is seen that braced frames are two times heavier than moment-resisting frames (Tables 6-7). However, the mean wind speed required to cause heavy damage to the structural members (LS performance level) with 100% probability for the braced frame is more than twice that for the moment-resisting frame. Similarly, the mean wind speed needed to cause collapse to the structural members (CP performance level) with 100% certainty is over twice as high for the braced frame

compared to the moment-resisting frame. While infrequent, these severe wind speeds have the potential to result in significant loss of life and property. Thus, it is important to consider these average wind speeds while designing buildings in hurricane-prone areas.

Symbols

K_d wind directionality factor

K_{zt} topographic factor

G impact factor

GC_{pi} internal pressure coefficient

V wind speed

D dead load

L live load

S snow load

E earthquake load

$S_{Vw}(\omega)$ wind spectral density

C surface roughness coefficient

V_w mean wind speed at specific height

F_g gust factor

V_i^G Gaussian variable

σx_i mean

μx_i variance

$P(C \mid IM = x)$ is the possibility of collapse the structure for wind speed corresponding to IM = x

IM intensity measure

θ mean fragility curve

β standard deviation of ln(IM)

z_j number of occurring collapses

n_j is the number of wind speed

x_j is the level of intensity measure

Acknowledgements

This research did not receive any specific grant from funding agencies in the public, commercial, or not-for-profit sectors.

References

[1] 3TIER, Global Mean Wind Speed at 80 m, University of Utah (2011). https://www.inscc.utah.edu/~krueger/5270/3tier_5km_global_wind_speed.pdf (accessed September 25, 2022).

[2] American Society of Civil Engineers, ASCE/SEI 7-10: Minimum design loads for buildings and other structures, 3rd ed., American Society of Civil Engineers, Virginia, 2013.

[3] W. Cui, L. Caracoglia, Exploring hurricane wind speed along US Atlantic coast in warming climate and effects on predictions of structural damage and intervention costs, Eng Struct 122 (2016) 209–225. https://doi.org/10.1016/J.ENGSTRUCT.2016.05.003.

[4] R.K. Tessari, H.M. Kroetz, A.T. Beck, Performance-based design of steel towers subject to wind action, Eng Struct 143 (2017) 549–557. https://doi.org/10.1016/J.ENGSTRUCT.2017.03.053.

[5] Y.J. Cha, J.W. Bai, Seismic fragility estimates of a moment-resisting frame building controlled by MR dampers using performance-based design, Eng Struct 116 (2016) 192–202. https://doi.org/10.1016/J.ENGSTRUCT.2016.02.055.

[6] M. Ansari, A. Safiey, M. Abbasi, Fragility based performance evaluation of mid rise reinforced concrete frames in near field and far field earthquakes, Structural Engineering and Mechanics 76 (2020) 751. https://doi.org/10.12989/SCS.2020.76.6.751.

[7] P. Liu, Z.-H. Li, W.-G. Yang, Seismic fragility analysis of sliding artifacts in nonlinear artifact-showcase-museum systems, Structural Engineering and Mechanics 78 (2021) 333. https://doi.org/10.12989/SEM.2021.78.3.333.

[8] D.G. Lignos, E. Karamanci, Drift-based and dual-parameter fragility curves for concentrically braced frames in seismic regions, J Constr Steel Res 90 (2013) 209–220. https://doi.org/10.1016/J.JCSR.2013.07.034.

[9] A. Gürbüz, M. Tekin, Farklı Tip Betonarme Binalar İçin Geliştirilmiş Hasar Tahmin Yöntemleri, Teknik Dergi 28 (2017) 8051–8076. https://doi.org/10.18400/TEKDERG.334196.

[10] M. Salameh, M. Shayanfar, M.A. Barkhordari, Seismic Performance of a Hybrid Coupled Wall System Using different Coupling Beam Arrangements, Teknik Dergi 33 (2022) 12401–12428. https://doi.org/10.18400/TEKDERG.782642.

[11] C. Ciftci, S.R. Arwade, B. Kane, S.F. Brena, Analysis of the probability of failure for open-grown trees during wind storms, Probabilistic Engineering Mechanics 37 (2014) 41–50. https://doi.org/10.1016/J.PROBENGMECH.2014.04.002.

[12] J. Shin, K. Lee, S.H. Jeong, J. Lee, Probabilistic performance assessment of gravity-designed steel frame buildings using buckling-restrained knee braces, J Constr Steel Res 104 (2015) 250–260. https://doi.org/10.1016/J.JCSR.2014.10.019.

[13] S. Sakurai, B.R. Ellingwood, S. Kushiyama, Probabilistic study of the behavior of steel frames with partially restrained connections, Eng Struct 23 (2001) 1410–1417. https://doi.org/10.1016/S0141-0296(01)00052-9.

[14] C.M. Ramirez, D.G. Lignos, E. Miranda, D. Kolios, Fragility functions for pre-Northridge welded steel moment-resisting beam-to-column connections, Eng Struct 45 (2012) 574–584. https://doi.org/10.1016/J.ENGSTRUCT.2012.07.007.

[15] A.K. Kazantzi, D. Vamvatsikos, D.G. Lignos, Seismic performance of a steel moment-resisting frame subject to strength and ductility uncertainty, Eng Struct 78 (2014) 69–77. https://doi.org/10.1016/J.ENGSTRUCT.2014.06.044.

[16] A.E. Özel, E.M. Güneyisi, Effects of eccentric steel bracing systems on seismic fragility curves of mid-rise R/C buildings: A case study, Structural Safety 33 (2011) 82–95. https://doi.org/10.1016/J.STRUSAFE.2010.09.001.

[17] S.H. Kim, M. Shinozuka, Development of fragility curves of bridges retrofitted by column jacketing, Probabilistic Engineering Mechanics 19 (2004) 105–112. https://doi.org/10.1016/J.PROBENGMECH.2003.11.009.

[18] S. Bobby, S.M.J. Spence, E. Bernardini, A. Kareem, Performance-based topology optimization for wind-excited tall buildings: A framework, Eng Struct 74 (2014) 242–255. https://doi.org/10.1016/J.ENGSTRUCT.2014.05.043.

[19] F. Mazza, M. Fiore, Vibration control by damped braces of fire-damaged steel structures subjected to wind and seismic loads, Soil Dynamics and Earthquake Engineering 83 (2016) 53–58. https://doi.org/10.1016/J.SOILDYN.2016.01.003.

[20] Y. Gong, Y. Xue, L. Xu, Optimal capacity design of eccentrically braced steel frameworks using nonlinear response history analysis, Eng Struct 48 (2013) 28–36. https://doi.org/10.1016/J.ENGSTRUCT.2012.10.001.

[21] A. Arablouei, V. Kodur, A fracture mechanics-based approach for quantifying delamination of spray-applied fire-resistive insulation from steel moment-resisting frame subjected to seismic loading, Eng Fract Mech 121–122 (2014) 67–86. https://doi.org/10.1016/J.ENGFRACMECH.2014.03.003.

[22] A. Imanpour, K. Auger, R. Tremblay, Seismic design and performance of multi-tiered steel braced frames including the contribution from gravity columns under in-plane seismic demand, Advances in Engineering Software 101 (2016) 106–122. https://doi.org/10.1016/J.ADVENGSOFT.2016.01.021.

[23] J. Iyama, H. Kuwamura, Probabilistic advantage of vibrational redundancy in earthquake-resistant steel frames, J Constr Steel Res 52 (1999) 33–46. https://doi.org/10.1016/S0143-974X(99)00012-7.

[24] Y.C. Lin, Steel sliding-controlled coupled beam modules: Development and seismic behavior for a moment resisting frame, Eng Struct 99 (2015) 726–736. https://doi.org/10.1016/J.ENGSTRUCT.2015.05.008.

[25] D.B. Merczel, J.M. Aribert, H. Somja, M. Hjiaj, Plastic analysis-based seismic design method to control the weak storey behaviour of concentrically braced steel frames, J Constr Steel Res 125 (2016) 142–163. https://doi.org/10.1016/J.JCSR.2016.05.008.

[26] M. Pirizadeh, H. Shakib, Probabilistic seismic performance evaluation of non-geometric vertically irregular steel buildings, J Constr Steel Res 82 (2013) 88–98. https://doi.org/10.1016/J.JCSR.2012.12.012.

[27] P. Sultana, M.A. Youssef, Seismic performance of steel moment resisting frames utilizing superelastic shape memory alloys, J Constr Steel Res 125 (2016) 239–251. https://doi.org/10.1016/J.JCSR.2016.06.019.

[28] J. Alam, D. Kim, B. Choi, Seismic risk assessment of intake tower in Korea using updated fragility by Bayesian inference, Structural Engineering and Mechanics 69 (2019) 317. https://doi.org/10.12989/SEM.2019.69.3.317.

[29] JavadMoradloo, K. Naserasadi, H. Zamani, Seismic fragility evaluation of arch concrete dams through nonlinear incremental analysis using smeared crack model, Structural Engineering and Mechanics 68 (2018) 747. https://doi.org/10.12989/SEM.2018.68.6.747.

[30] P. Liu, H.X. Zhu, P.P. Fan, W.G. Yang, A reliability-based fragility assessment method for seismic pounding between nonlinear buildings, Structural Engineering and Mechanics 77 (2021) 19–35. https://doi.org/10.12989/SEM.2021.77.1.019.

[31] G. Craighead, High-Rise Security and Fire Life Safety, 3rd ed., Butterworth-Heinemann, Boston, 2009.

[32] J.-W. Lai, S.A. Mahin, Strongback System: A Way to Reduce Damage Concentration in Steel-Braced Frames, Journal of Structural Engineering 141 (2014) 04014223. https://doi.org/10.1061/(ASCE)ST.1943-541X.0001198.

[33] T. Okazaki, M.D. Engelhardt, Cyclic loading behavior of EBF links constructed of ASTM A992 steel, J Constr Steel Res 63 (2007) 751–765. https://doi.org/10.1016/J.JCSR.2006.08.004.

[34] S. Kazemzadeh Azad, C. Topkaya, A review of research on steel eccentrically braced frames, J Constr Steel Res 128 (2017) 53–73. https://doi.org/10.1016/J.JCSR.2016.07.032.

[35] D.M. Patil, K.K. Sangle, Seismic Behaviour of Different Bracing Systems in High Rise 2-D Steel Buildings, Structures 3 (2015) 282–305. https://doi.org/10.1016/J.ISTRUC.2015.06.004.

[36] R. Sabelli, S. Mahin, C. Chang, Seismic demands on steel braced frame buildings with buckling-restrained braces, Eng Struct 25 (2003) 655–666. https://doi.org/10.1016/S0141-0296(02)00175-X.

[37] Computers and Structures Inc., Sap2000 v19.0.0, (2016).

[38] T. Uçar, M. Düzgün, Betonarme Binalar İçin Artımsal İtme Analizi Esaslı Analitik Hasargörebilirlik Eğrilerinin Oluşturulması, Teknik Dergi 24 (2013) 402. https://dergipark.org.tr/tr/pub/tekderg/issue/12741/155127 (accessed July 18, 2024).

[39] American Society of Civil Engineers, ASCE/SEI 7-10: Minimum design loads for buildings and other structures, 3rd ed., American Society of Civil Engineers, Virginia, 2013.

[40] R. Bjorhovde, The 2005 American steel structures design code, J Constr Steel Res 62 (2006) 1068–1076. https://doi.org/10.1016/J.JCSR.2006.06.011.

[41] M. Haddad, Cyclic behavior and finite element modeling of wide flange steel bracing members, Thin-Walled Structures 111 (2017) 65–79. https://doi.org/10.1016/J.TWS.2016.11.006.

[42] C.G. Salmon, J.E. Johnson, F.A. Malhas, Steel Structures Design and Behavior, 5th ed., Prentice Hall, New Jersey, 2008.

[43] J. Szalai, F. Papp, On the probabilistic evaluation of the stability resistance of steel columns and beams, J Constr Steel Res 65 (2009) 569–577. https://doi.org/10.1016/J.JCSR.2008.08.006.

[44] CSi Knowledge Base, Time-History Analysis, Computers and Structures Inc. (2014). https://wiki.csiamerica.com/display/kb/Time-history+analysis (accessed September 25, 2022).

[45] CSi Knowledge Base, Ritz vs. Eigen Vectors, Computers and Structures Inc. (2014). http://wiki.csiamerica.com/display/kb/Ritz+vs.+Eigen+vectors (accessed September 25, 2022).

[46] American Institute of Steel Construction, Manual of Steel Construction: Load and Resistance Factor Design, 3rd ed., American Institute of Steel Construction, İllinois, 2001.

[47] American Institute of Steel Construction, Steel Construction Manual, 15th ed., American Institute of Steel Construction, İllinois, 2017.

[48] L.-X. Li, H.-N. Li, C. Li, Seismic fragility assessment of self-centering RC frame structures considering maximum and residual deformations, Structural Engineering and Mechanics 68 (2018) 677. https://doi.org/10.12989/SEM.2018.68.6.677.

[49] Y. Lu, L. Zhang, Z. He, F. Feng, F. Pan, Wind-induced vibration fragility of outer-attached tower crane to super-tall buildings: A case study, Wind and Structures 32 (2021) 405. https://doi.org/10.12989/WAS.2021.32.5.405.

[50] S. Li, Z. Zuo, C. Zhai, L. Xie, Comparison of static pushover and dynamic analyses using RC building shaking table experiment, Eng Struct 136 (2017) 430–440. https://doi.org/10.1016/J.ENGSTRUCT.2017.01.033.

[51] M. Bocciarelli, G. Barbieri, A numerical procedure for the pushover analysis of masonry towers, Soil Dynamics and Earthquake Engineering 93 (2017) 162–171. https://doi.org/10.1016/J.SOILDYN.2016.07.022.

[52] K. Kamath, S. Hirannaiah, J.C.K.B. Noronha, An analytical study on performance of a diagrid structure using nonlinear static pushover analysis, Perspect Sci (Neth) 8 (2016) 90–92. https://doi.org/10.1016/J.PISC.2016.04.004.

[53] American Society of Civil Engineers, ASCE/SEI 41-13: Seismic Evaluation and Retrofit of Existing Buildings, 1st ed., American Society of Civil Engineers, Virginia, 2014.

[54] F.N. Kudu, Ş. Uçak, G. Osmancikli, T. Türker, A. Bayraktar, Estimation of damping ratios of steel structures by Operational Modal Analysis method, J Constr Steel Res 112 (2015) 61–68. https://doi.org/10.1016/J.JCSR.2015.04.019.

[55] A. V. Papageorgiou, C.J. Gantes, Equivalent modal damping ratios for concrete/steel mixed structures, Comput Struct 88 (2010) 1124–1136. https://doi.org/10.1016/J.COMPSTRUC.2010.06.014.

[56] M.S. Kırçıl, E.Ç. Kocabey, Examination of the Efficiency of Retrofitting Methods through Fragility Analysis, Teknik Dergi 30 (2019) 9243–9260. https://doi.org/10.18400/TEKDERG.408126.

[57] Baker Research Group, Efficient Analytical Fragility Function Fitting Using Dynamic Structural Analysis, Stanford University (2014). http://web.stanford.edu/~bakerjw/publications.html (accessed September 25, 2022).

[58] C. Çiftçi, A Methodology for Fast and Accurate Analytical Fragility Analysis of Linear Structural Systems during Wind Storms: ALFA, Erciyes Üniversitesi Fen Bilimleri Enstitüsü Fen Bilimleri Dergisi 39 (2023) 508-520.

Turkish Journal of Civil Engineering, 2025, 29-51, Paper 798, ***Research Article***

Intensity Characteristics of Seismograms Recorded During the February 6, 2023, M7.8 Türkiye-Kahramanmaraş-Pazarcık Earthquake

Kemal Onder CETIN[1*]
Alaa ELSAID[2]
A. Arda ÖZACAR[3]

ABSTRACT

The strong ground motion intensity levels recorded during the February 6, 2023, Türkiye-Kahramanmaraş-Pazarcık earthquake (M7.8) were compared with the ones predicted by the four ground motion models of 2014 NGA WEST-2 Ground Motion Prediction Equations (GMPEs), and by the Turkish Earthquake Design Code (TEC, 2018). These comparisons revealed that Adana, Malatya, and Gaziantep cities were shaken by peak ground acceleration (PGA) levels less intense than the ones predicted by GMPEs. Contrary to these cities, ordered from the highest to lowest positive residuals, Şanlıurfa, Hatay, Kahramanmaraş, and Elazığ cities were shaken by higher levels of PGA than those predicted by the GMPEs. The TEC DD-1 and DD-2 seismic scenario PGA levels were exceeded at 5 and 22 out of 71 stations, respectively. The residuals for the stations on the Anatolian plate side exhibited a more correlated residual trend with the recorded PGA levels. The stations of exceeded seismic PGA demands are site class ZC or softer. PGA levels for DD-1 were exceeded at stations in the city of Hatay. The highest positive residual is also estimated for the Defne-Hatay station #3135, where the most structural damage was concentrated. The spectral acceleration residuals were also assessed. The spectral acceleration levels in all period ranges were higher than those predicted by Abrahamson, Silva and Kamai (2014), Campbell and Bozorgnia (2014) GMPE models. For spectral periods longer than 0.06 and 0.3 seconds, respectively, Chiou and Youngs (2014), and Boore, Stewart, Seyhan and Atkinson (2014) medial predictions were exceeded. Additionally, the structures with spectral periods of 0.7 seconds and longer were estimated to be subjected to approximately 20 to 30 % higher seismic

Note:
- This paper was received on August 23, 2023 and accepted for publication by the Editorial Board on September 6, 2024.
- Discussions on this paper will be accepted by May 31, 2025.
- https://doi.org/10.18400/tjce.1348206

1 Middle East Technical University, Department of Civil Engineering, Ankara, Türkiye
ocetin@metu.edu.tr - https://orcid.org/0000-0003-0540-2247

2 Middle East Technical University, Department of Civil Engineering, Ankara, Türkiye
elsd.alaa@gmail.com - https://orcid.org/0000-0003-0369-0417

3 Middle East Technical University, Department of Geological Engineering, Ankara, Türkiye
ozacar@metu.edu.tr - https://orcid.org/0000-0001-9700-4400

* Corresponding author

demands, as defined by TEC for DD-2 design basis scenario. This is listed as one of the factors among many, contributing to the concentrated damage observed in residential buildings with number of stories higher than 5 to 7.

Keywords: Intensity, GMPEs, Turkish Earthquake code, Kahramanmaraş earthquake, Pazarcık earthquake.

INTRODUCTION

On February 6, 2023, two earthquakes, with moment magnitudes M7.8 and M7.6, occurred in southeastern Türkiye on the East Anatolian Fault Zone (EAFZ), at local times of 04:17 and 13:24, respectively. The induced damage scattered widely, affecting numerous provinces, including Kahramanmaraş, Gaziantep, Şanlıurfa, Diyarbakır, Adana, Adıyaman, Osmaniye, Hatay, Kilis, Malatya, and Elazığ, as shown in Figure 1.

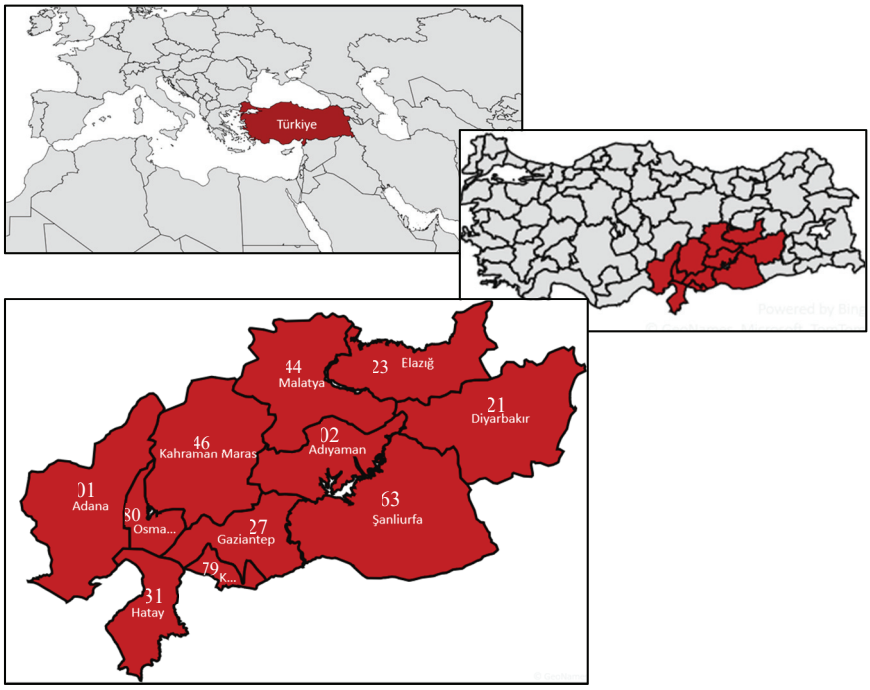

Figure 1 - The cities affected by the February 6, 2023, Türkiye-Kahramanmaraş-Pazarcık Earthquake M7.8

The resulting impact encompassed substantial casualties, injuries, and extensive infrastructure devastation. Referred to as the earthquake doublet, the cumulative effect of these events resulted in documented fatalities exceeding 50,000 in Türkiye, and 7,200 in Syria. Moreover, an estimated 15 million individuals were affected by these catastrophic events. The seismic activity also reportedly led to the destruction of around 520,000 residential units in Türkiye (Çetin et al., 2023a-b; Çetin and Ilgaç, 2023).

The second event occurred approximately 9 hours later at a focal depth of 7.0 km in Kahramanmaraş-Elbistan-Ekinözü, 100 km north of the first event's epicenter, on an east-west-striking northern strand of the EAFZ: more specifically on the Sürgü-Misis fault zone (SMFZ). Focal mechanism solutions offered by various agencies - AFAD (Disaster and Emergency Management Presidency), CMT (The Global Centroid-Moment-Tensor), USGS (United States Geological Survey), and GFZ (German Research Sciences for Geosciences) – consistently suggest strike-slip faulting as the prevailing source mechanisms for both events. This aligns harmoniously with both regional tectonics and the distinctive attributes of the EAFZ, on which both seismic events were located.

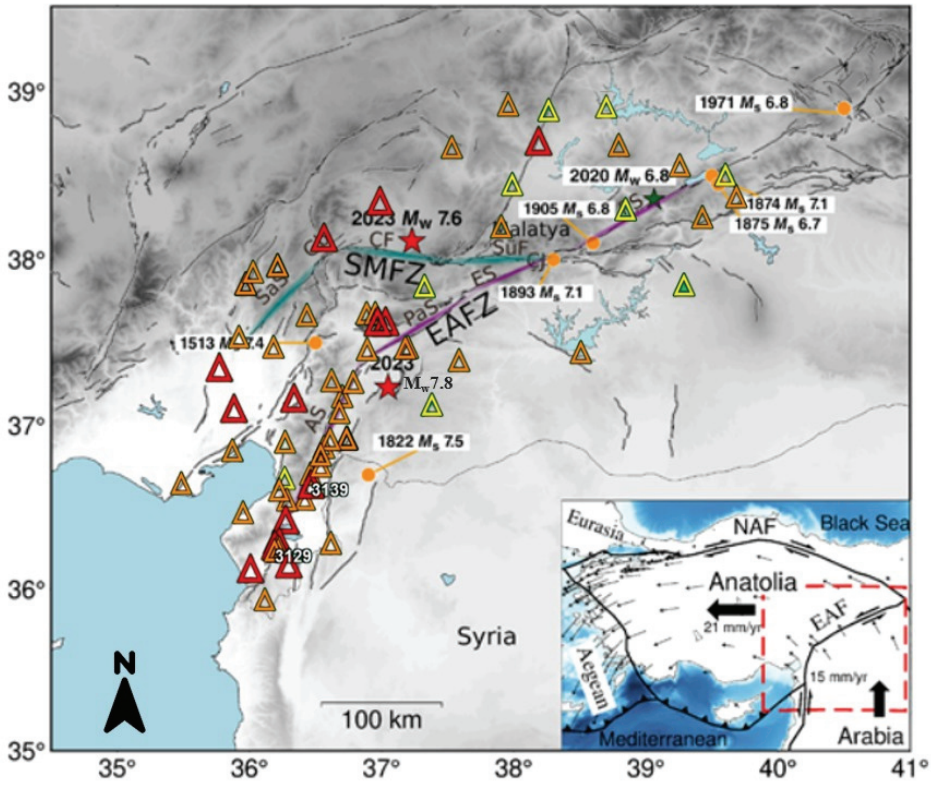

Figure 2 - Map of the region showing fault systems (Duman and Emre, 2013) and major historical earthquakes (orange circles; Ambraseys, 1989) along EAFZ. Kahramanmaraş-Pazarcık earthquake ruptured the main segments of the EAFZ (magenta) and Kahramanmaraş-Elbistan-Ekinözü earthquake ruptured the Sürgü-Misis fault zone (SMFZ; cyan). Red stars show epicenters of the events. EAFZ fault segments are labeled as AS, Amanos; Cj, Çelikhan junction; ES, Erkenek; PaS, Pazarcık;PS, Pütürge. SMFZ segments: CF, Çardak fault; Gb, Göksun bend; SaS, Savrun segment; and SüF, Sürgü fault (Duman and Emre, 2013). The triangles show the locations of the SGMSs: site class ZD: red, ZC: orange, ZB: yellow. The overview map provided in the lower right corner illustrates the main tectonic elements and their relative movement. Plate convergence rates are adopted from McClusky et al. (2000). The figure is adapted from Petersen et al. (2023).

As shown in Figure 2, the epicenter of the first event, which has a focal depth of 8.6 km, is in Kahramanmaraş-Pazarcık. Kahramanmaraş-Pazarcık earthquake initiated approximately 20 km southeast of the main strand of the EAFZ along a splay fault, more specifically along Narlı fault, which is oriented in the northeast-southwest direction (Melgar et al., 2023; Okuwaki et al., 2023, Petersen et al., 2023). The rupture nucleated on the splay fault propagated towards the north to the main strand of the EAFZ, rupturing a series of segments namely, Amanos, Pazarcık and Erkenek, during a multi-phased segmented rupture process (Okuwaki et al., 2023; Zahradník et al., 2023, Petersen et al., 2023). A series of elevated seismic activities were recorded in the region within a period of 10 months before the events (Kwiatek et al., 2023; Picozzi and Iaccarino, 2023). After the mainshock, more than 400 aftershocks with $M \geq 5$ were recorded in the period of February 6 to March 1, within 200 km radii of the epicenter.

STRONG GROUND MOTION DATA

Available strong ground motion records within 100 km from the fault rupture were accessed from Turkish Disaster and Emergency Management Presidency (AFAD) web portal, accessible at https://tadas.afad.gov.tr (accessed August 2023). These strong ground motion records were already processed by AFAD. Given the methodological similarities between AFAD and NGA WEST-2 ground motion data processing protocols, additional signal processing was deemed unnecessary for comparison purposes. Both protocols encompass baseline correction, band-pass filtering, and time windowing to mitigate noise and enhance data integrity. While AFAD's protocol is tailored for regional specifics, it shares core principles with the ITACA protocol, including instrument response removal, baseline adjustment, and spectral filtering (Luzi et al., 2016). For more detailed information, please refer to the AFAD web portal (https://tadas.afad.gov.tr), the Italian Accelerometric Archive (ITACA) (Pacor et al., 2011; Massa et al., 2010), and the Engineering Strong-Motion Database (Luzi et al., 2016). The signal processing was performed in an automated manner, which was further adjusted manually when needed.

The strong ground motion stations (SGMSs), located within 100 km of the fault rupture plane ($R_{rup} \leq 100$ km) are shown in Figure 2. The stations outside this zone, or with invalid recordings, were excluded from further consideration, resulting to a total number of 71 stations in the database. The applicability/validity limits of GMPEs were checked. Only SGMS # 4404, which has a shear wave velocity measurement representing the upper 30 meters (i.e.: V_{s30}) value of 1380 m/s, violated the ASK (Abrahamson, Silva and Kamai, 2014) $V_{s30}<1000$ m/s requirement. Hence it was excluded for the comparisons with ASK predictions. Among the remaining SGMSs, 51 of them have shear wave velocity (V_s) profiles, which are also accessible at https://tadas.afad.gov.tr. V_{s30} values range from 210 m/s to 1380 m/s. For the strong ground motion stations with missing values, V_{s30} were estimated based on V_{s30} model of Türkiye utilizing geology, topography, terrain and water saturation levels (Okay and Özacar, 2023). Table 1 provides a comprehensive summary of the employed strong ground motion station characteristics, encompassing essential parameters, including their coordinates, rupture distances, V_{s30} values, and the recorded peak ground acceleration (PGA) levels.

Table 1 - A summary of SGMS characteristics, and the recorded and predicted PGA levels (data accessed from AFAD web portal in August, 2023).

City	Station #	Longitude	Latitude	R_{rup} (km)	V_{s30} (m/s)	$PGA_{recorded}$ (g)			$PGA_{NGA\ WEST-2\ GMPE}$ (g)			PGA_{TEC} (g)		PGA recorded exceeded?	
						E-W	N-S	U-D	ASK	CB	CY	DD-1	DD-2	DD-1	DD-2
Adana	0119	35.39000	36.56800	83.8	485	0.045	0.044	0.026	0.078	0.075	0.084	0.633	0.310	No	No
	0120	35.79005	36.77006	59.6	439	0.118	0.115	0.105	0.114	0.103	0.118	0.778	0.356	No	No
	0122	35.82021	37.43390	86.1	501	0.053	0.058	0.034	0.075	0.072	0.081	0.601	0.315	No	No
	0125	35.79577	37.01519	69.8	216	0.085	0.131	0.036	0.121	0.100	0.128	0.506	0.331	No	No
	0127	35.92044	37.81618	95.8	583	0.052	0.056	0.040	0.062	0.061	0.068	0.555	0.283	No	No
	0130	35.67104	37.25186	90.3	358	0.070	0.083	0.036	0.081	0.073	0.088	0.519	0.326	No	No
	0131	36.11535	37.85660	84.7	631	0.163	0.149	0.051	0.069	0.070	0.074	0.599	0.306	No	No
	0132	36.11487	37.85589	84.7	631	0.033	0.039	0.030	0.069	0.070	0.074	0.600	0.306	No	No
	0133	35.86403	37.74550	96.3	631	0.076	0.079	0.040	0.060	0.059	0.065	0.591	0.298	No	No
	0134	35.86448	37.74427	96.2	631	0.047	0.070	0.039	0.060	0.059	0.065	0.592	0.299	No	No
Diyarbakır	2104	39.75900	38.26440	99.7	417	0.090	0.064	0.044	0.068	0.062	0.075	0.674	0.363	No	No
	2107	39.48379	38.14594	74.7	455	0.114	0.076	0.045	0.090	0.085	0.096	0.670	0.360	No	No
Elazığ	2302	39.67541	38.39231	95.6	907	0.224	0.201	0.112	0.051	0.054	0.054	0.786	0.413	No	No
	2308	39.31020	38.45063	68.9	450	0.167	0.329	0.408	0.098	0.091	0.103	1.326	0.722	No	No
	2309	38.72728	38.79913	74.2	860	0.036	0.038	0.026	0.069	0.074	0.071	0.460	0.229	No	No
	2310	38.82453	38.57266	51.4	426	0.052	0.062	0.050	0.130	0.116	0.135	0.792	0.412	No	No

Gaziantep	2703	37.35000	37.05800	51.4	758	0.163	0.153	0.082	0.104	0.103	0.105	0.394	0.214	No	No
Hatay	2708	36.64837	37.09933	4.0	523	1.111	0.828	0.996	0.474	0.477	0.546	1.232	0.610	No	Yes
	2711	37.56036	37.31736	35.2	555	0.099	0.109	0.063	0.160	0.148	0.165	0.356	0.208	No	No
	2712	36.73283	37.18400	1.0	599	0.614	0.566	0.350	0.543	0.537	0.635	1.144	0.562	No	Yes
	2715	36.68562	36.85536	9.8	468	0.347	0.466	0.078	0.353	0.349	0.411	1.028	0.534	No	No
	2716	36.68833	36.85643	10.0	431	0.233	0.260	0.168	0.353	0.344	0.414	1.023	0.531	No	No
	2717	36.69100	36.85548	10.3	455	0.120	0.141	0.082	0.346	0.340	0.403	1.018	0.528	No	No
	2718	36.62660	37.00777	1.7	421	0.656	0.716	0.596	0.534	0.499	0.651	1.257	0.635	No	Yes
	3115	36.16459	36.54634	19.1	424	0.215	0.280	0.219	0.256	0.237	0.286	0.685	0.362	No	No
	3116	36.20661	36.61618	18.7	868	0.169	0.164	0.166	0.203	0.223	0.219	0.522	0.276	No	No
	3123	36.15973	36.21423	14.4	470	0.606	0.668	0.885	0.292	0.282	0.334	1.013	0.501	No	Yes
	3124	36.17220	36.23870	11.7	283	0.650	0.584	0.589	0.333	0.301	0.391	0.826	0.448	No	Yes
	3125	36.13264	36.23808	14.6	448	1.145	0.839	1.158	0.293	0.280	0.335	0.967	0.482	Yes	Yes
	3126	36.13750	36.22020	15.4	350	1.049	1.234	1.091	0.295	0.269	0.338	0.830	0.448	Yes	Yes
	3129	36.13430	36.19117	17.9	447	1.223	1.394	0.842	0.263	0.246	0.295	1.042	0.511	Yes	Yes
	3131	36.16328	36.19121	16.2	567	0.346	0.356	0.147	0.262	0.260	0.292	1.040	0.511	No	No
	3132	36.17159	36.20673	14.4	377	0.524	0.525	0.361	0.302	0.281	0.349	1.017	0.504	No	Yes
	3133	36.57360	36.24320	27.9	471	0.146	0.223	0.089	0.198	0.181	0.211	0.822	0.405	No	No
	3134	36.20485	36.82763	28.2	374	0.208	0.251	0.143	0.208	0.183	0.224	0.609	0.332	No	No
	3135	35.88310	36.40886	36.4	460	1.394	0.755	0.601	0.166	0.149	0.173	0.540	0.300	Yes	Yes
	3136	36.24722	36.11593	21.6	344	0.402	0.544	0.225	0.248	0.219	0.274	0.712	0.418	No	Yes
	3137	36.48852	36.69293	1.0	688	0.859	0.461	0.509	0.525	0.543	0.604	1.303	0.666	No	No
	3138	36.51119	36.80262	2.0	618	0.761	0.906	1.089	0.520	0.526	0.588	1.332	0.678	No	Yes
	3139	36.41439	36.58383	0.3	272	0.514	0.588	0.386	0.499	0.442	0.661	1.028	0.516	No	Yes
	3140	35.94982	36.08155	38.3	210	0.223	0.198	0.180	0.186	0.150	0.196	0.744	0.424	No	No
	3141	36.21973	36.37260	6.9	338	0.869	0.963	0.631	0.408	0.385	0.489	0.838	0.449	Yes	Yes
	3142	36.36612	36.49797	0.4	539	0.761	0.660	0.513	0.555	0.533	0.682	1.180	0.581	No	Yes
	3143	36.55714	36.84891	0.4	445	0.358	0.389	0.420	0.555	0.515	0.705	1.394	0.699	No	No
	3144	36.48574	36.75691	2.1	535	0.779	0.623	0.461	0.525	0.516	0.611	1.345	0.685	No	Yes
	3145	36.40640	36.64536	3.7	533	0.710	0.611	0.673	0.482	0.485	0.553	1.282	0.644	No	Yes

	3146	36.22695	36.49076	11.5	439	0.353	0.491	0.347	0.331	0.321	0.385	0.945	0.471	No	No
	3147	36.06436	35.90236	48.8	558	0.048	0.058	0.030	0.124	0.115	0.126	0.851	0.439	No	No
Malatya	4404	38.87385	38.19588	22.3	1380	0.139	0.138	0.098	0.146	0.169	0.168	1.032	0.568	No	No
	4405	37.93960	38.81070	94.5	579	0.129	0.092	0.079	0.064	0.062	0.069	0.467	0.253	No	No
	4406	37.97378	38.34388	47.5	815	0.134	0.111	0.051	0.108	0.108	0.108	0.745	0.329	No	No
	4407	38.26406	38.78066	78.4	735	0.034	0.044	0.020	0.070	0.073	0.073	0.877	0.398	No	No
	4408	37.88732	38.09616	27.0	654	0.140	0.102	0.099	0.183	0.177	0.190	1.023	0.531	No	No
	4409	37.49076	38.56063	88.9	462	0.029	0.039	0.029	0.075	0.071	0.081	0.371	0.198	No	No
	4412	38.18385	38.59685	63.5	356	0.070	0.065	0.057	0.115	0.101	0.120	0.695	0.380	No	No
	4611	37.28426	37.74720	18.5	731	0.327	0.356	0.177	0.221	0.231	0.240	0.819	0.430	No	No
	4612	36.48187	38.02395	79.7	246	0.125	0.144	0.055	0.104	0.090	0.111	0.601	0.344	No	No
	4613	36.35737	37.57010	48.8	434	0.157	0.150	0.076	0.135	0.120	0.139	0.658	0.334	No	No
Kahramanmaraş	4615	37.13803	37.38676	10.3	484	0.592	0.595	0.677	0.343	0.341	0.398	1.000	0.514	No	Yes
	4616	36.83836	37.37547	2.3	390	0.516	0.627	0.406	0.518	0.483	0.629	1.047	0.530	No	Yes
	4617	36.83030	37.58551	22.2	574	0.117	0.148	0.113	0.217	0.209	0.233	0.717	0.374	No	No
	4620	36.89845	37.58568	19.3	484	0.327	0.306	0.189	0.247	0.234	0.274	0.778	0.407	No	No
	4624	36.91765	37.53610	13.7	280	0.326	0.364	0.165	0.312	0.279	0.362	0.774	0.441	No	No
	4625	36.98187	37.53872	11.1	346	0.494	0.457	0.374	0.342	0.319	0.403	0.861	0.470	No	Yes
	4628	36.92281	38.24120	81.9	337	0.084	0.093	0.057	0.092	0.083	0.099	0.480	0.306	No	No
	NAR	37.15740	37.39190	10.7	450	0.117	0.120	0.040	0.065	0.070	0.066	0.263	0.141	No	No
Şanlıurfa	6303	39.32910	37.75240	74.7	986	0.243	0.215	0.091	0.102	0.092	0.108	0.377	0.176	No	Yes
	6304	38.51316	37.36509	70.7	376	0.207	0.247	0.342	0.289	0.273	0.330	0.852	0.444	No	No
Osmaniye	8002	36.56195	37.19156	15.2	430	0.189	0.144	0.143	0.187	0.160	0.197	0.580	0.354	No	No
	8003	36.26936	37.08417	34.2	350	0.182	0.172	0.073	0.112	0.101	0.117	0.610	0.324	No	No
	8004	36.09763	37.37989	61.2	426	0.626	0.781	0.492	0.341	0.333	0.397	0.988	0.509	No	Yes

The seismic shaking levels recorded at SGMS #3139 and # 3129 are particularly important due to their proximity to the fault rupture plane. The locations of both stations are shown in Figure 2. SGMS # 3139, underlain by medium stiff soil layers with a shear wave velocity (V_{s30}) of 272 m/s, is in Kırıkhan-Hatay. It is 300 m away from the fault rupture plane (i.e.: R_{rup} =300 m), and is the nearest station, which provided a reliable set of seismograms. The recorded PGA values in the east-west (E-W), north-south (N-S), and vertical directions (U-D) are 0.584 g, 0.514 g, and 0.360 g, respectively. SGMS # 3129 is in Defne-Hatay, and recorded the highest PGA levels during this event. It is a medium stiff soil site with a V_{s30} value of 447 m/s. The recorded PGA values in the E-W, N-S, and U-D directions are 1.125 g, 1.138 g, and 0.731 g, respectively.

COMPARATIVE ASSESSMENT OF SEISMIC INTENSITY DEMAND LEVELS

In this section, the seismic intensity predictions by 2014 NGA WEST-2 Ground Motion Prediction Equations (GMPEs) are presented. More specifically, the predictions by ASK, CB (Campbell and Bozorgnia, 2014), CY (Chiou and Youngs, 2014), and BSSA (Boore, Stewart, Seyhan and Atkinson, 2014) models are compared with the recorded peak ground acceleration (PGA) and spectral acceleration (S_A) values. Similarly, the Turkish earthquake design code (TEC) basis intensities are comparatively presented. For comparison purposes, residual (error) plots are prepared, and the variation of residual terms are shown with respect to the i) station locations, ii) distance and angular orientation relative to the fault rupture plane, iii) V_{s30}, iv) recorded intensity levels.

Comparisons of the Recorded vs. Predicted PGAs

PGA intensity levels are assessed by ASK, CB, CY and BSSA models. Then residuals are estimated for each ground motion station. The residuals (R_i) are defined as the difference between the natural logarithm of the recorded and predicted intensity measures (i.e.: IM_R and IM_{GMPE}), as given in Equation 1:

$$R_i = \ln(\mathrm{IM_i})_R - \ln(IM_i)_P \quad (1)$$

More specifically, in Equation 1, R_i represents the residual for station "*i*", and the $(IM_i)_R$ and $(IM_i)_P$ terms indicate the geometric mean of the recorded and predicted intensity measure at station *i*. These residuals are shown against Joyner-Boore distance (R_{jb}), V_{s30}, recorded PGA values, and the azimuth angle (θ). The azimuth angle (θ) is particularly selected to assess the rupture directivity and/or velocity effects.

It is important to acknowledge the role of supershear effects on ground motion characteristics. During a supershear rupture, the rupture front propagates faster than the shear wave velocity, and this can significantly amplify ground motion intensities, particularly in the fault-parallel direction. Hu et al. (2020) demonstrated that sustained supershear rupture tends to produce a clear Mach cone and amplified ground motion, especially in near-fault regions, with deeper hypocenter depths being more likely to sustain supershear rupture. Dunham & Archuleta (2004) highlighted how supershear transients, which were observed during the 2002 Denali earthquake, contributed to high ground motion intensities, particularly due to additional

Rayleigh waves along the fault surface. Bouchon et al. (2000) emphasized that such rupture dynamics, as observed in the 1999 Izmit earthquake, can lead to significantly enhanced ground shaking, especially in the direction of rupture propagation. Additionally, Song et al. (2008) found that supershear rupture impacts the amplitude and frequency content of ground motion, particularly at longer periods, which are critical for assessing seismic demand.

With the intent of assessing the directivity and supershear effects on strong ground motion records, the azimuth angle of each station is estimated. Consistent with Somerville et al. (1997), θ is defined as the azimuth angle between the fault plane and ray path, as illustrated in Figure 3. Since the rupture first initiated on a splay fault (i.e.: Narlı fault) in the southeast, then continued along the EAFZ bilaterally towards the north and south, the point where EAFZ changes strike forming a kink, is used as the modified epicenter for the calculation of azimuth angles. The kink point, and the modified epicenter is illustrated in Figure 3 (c). In our assessments we have assumed the distances for rupture and Joyner-Boore as identical (i.e.: $R_{rup} = R_{jb}$). This assumption holds for 90° degree dipping fault rupture planes reaching the ground surface which were both satisfied during the Pazarcık event (Gülerce et al., 2023). Our assessments were performed on records obtained within 100 km of the fault rupture due to significantly reduced intensities (PGA < 0.02) and widely scattered data beyond it. This limitation should be considered when interpreting the results, particularly concerning event-specific anelastic attenuation effects.

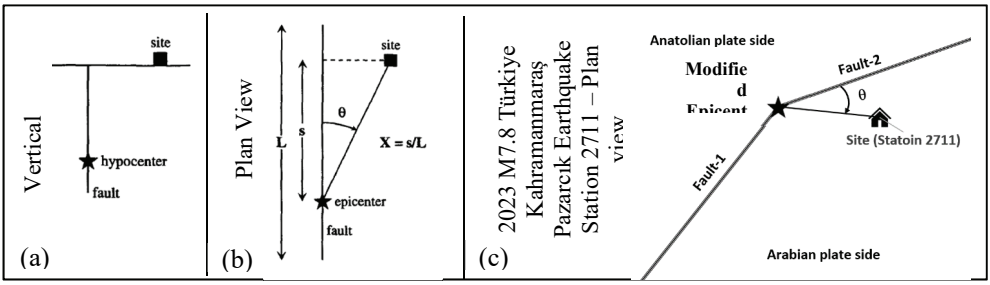

Figure 3 - Rupture directivity parameters for a strike-slip fault (after Somerville et al., 1997)

To assess possible path effects and the interaction between Arabian and Anatolian plates, SGMSs are binned as "on the eastern (on the Arabian plate)" and "on the western (on the Anatolian plate)" sides of the fault rupture. This allows to assess the dependency of residuals on SGMS's position relative to the causative plates.

Variability in PGA Residuals with Geographical Locations

The scatter in residuals is shown with respect to the geographical location of the stations. Figure 4 and Table 2 present the estimated residuals geographically grouped into city bins. On Figure 4, gray dashed lines show the mean, and mean plus and minus one standard deviation (σ) residuals estimated for the overall database. Similarly, mean, and mean ± σ residuals for each city bin, are shown in red solid lines. Circles and dots represent the

estimated mean residuals for the stations located on the Anatolian and Arabian plates, respectively. Table 2 presents a summary of the statistics of the residuals for each city.

The interpretation of Figure 4 and Table 2 reveals that Diyarbakır and Osmaniye cities had the most accurate predictions across all models, with the lowest mean residuals. For the other cities, the four GMPEs suggest that Adana, Malatya, and Gaziantep experienced PGA levels that were less intense than those predicted by them. In contrast, ordered from the highest to lowest positive residuals, Şanlıurfa, Hatay, Kahramanmaraş, and Elazığ were shaken by higher levels of PGA than those predicted by the GMPEs. Overall, Among the four GMPEs, the BSSA model provided the least biased predictions, producing the lowest overall mean residual. The overall mean ± σ residuals for the stations located east (Arabian plate side) and west (Anatolian plate side) of the fault rupture plane are estimated as 0.20 ± 0.66 and 0.14 ± 0.62, respectively. Hence, stations located on the Arabian plate side of the rupture demonstrate more pronounced overpredicted residuals, whereas those situated on the Anatolian plate side of the fault exhibit a slightly better fit with less overpredictions by these four models. The highest positive residual value is estimated for SGMS # 3135 in Hatay, where intense structural damage was reported.

The observed variability in ground motion data for Hatay can be attributed to a combination of site effects, including soil-site, basin, directivity and supershear effects, particularly those associated with the Amik Plain basin. The larger scatter in intensity recordings is also further influenced by the higher number of available Strong Ground Motion stations located on variable site conditions in Hatay. In contrast, Osmaniye exhibits a smaller spread, which can be attributed to under sampling of strong ground motion variability (i.e.: only two strong ground motion stations) or relatively homogeneous nature of geological setting.

Table 2 - A summary of mean ± σ residuals estimated for each city bin

City	ASK	CB	CY	BSSA
Şanlıurfa	0.70 ± 0.10	0.71 ± 0.19	0.66 ± 0.08	0.52 ± 0.06
Adana	-0.08 ± 0.39	-0.03 ± 0.39	-0.15 ± 0.39	-0.31 ± 0.4
Kahramanmaraş	0.21 ± 0.31	0.27 ± 0.29	0.10 ± 0.29	0.07 ± 0.32
Elazığ	0.21 ± 0.96	0.23 ± 0.94	0.16 ± 0.95	0.02 ± 0.95
Malatya	-0.25 ± 0.44	-0.24 ± 0.42	-0.31 ± 0.44	-0.40 ± 0.46
Hatay	0.42 ± 0.61	0.48 ± 0.62	0.29 ± 0.61	0.31 ± 0.6
Osmaniye	0.03 ± 0.31	0.13 ± 0.32	-0.04 ± 0.34	-0.13 ± 0.27
Gaziantep	-0.02 ± 0.50	0.00 ± 0.50	-0.15 ± 0.51	-0.13 ± 0.51
Diyarbakır	0.07 ± 0.04	0.14 ± 0.05	-0.01 ± 0.01	-0.18 ± 0.01
OVERALL	0.17 ± 0.58	0.22 ± 0.57	0.07 ± 0.57	0.02 ± 0.58

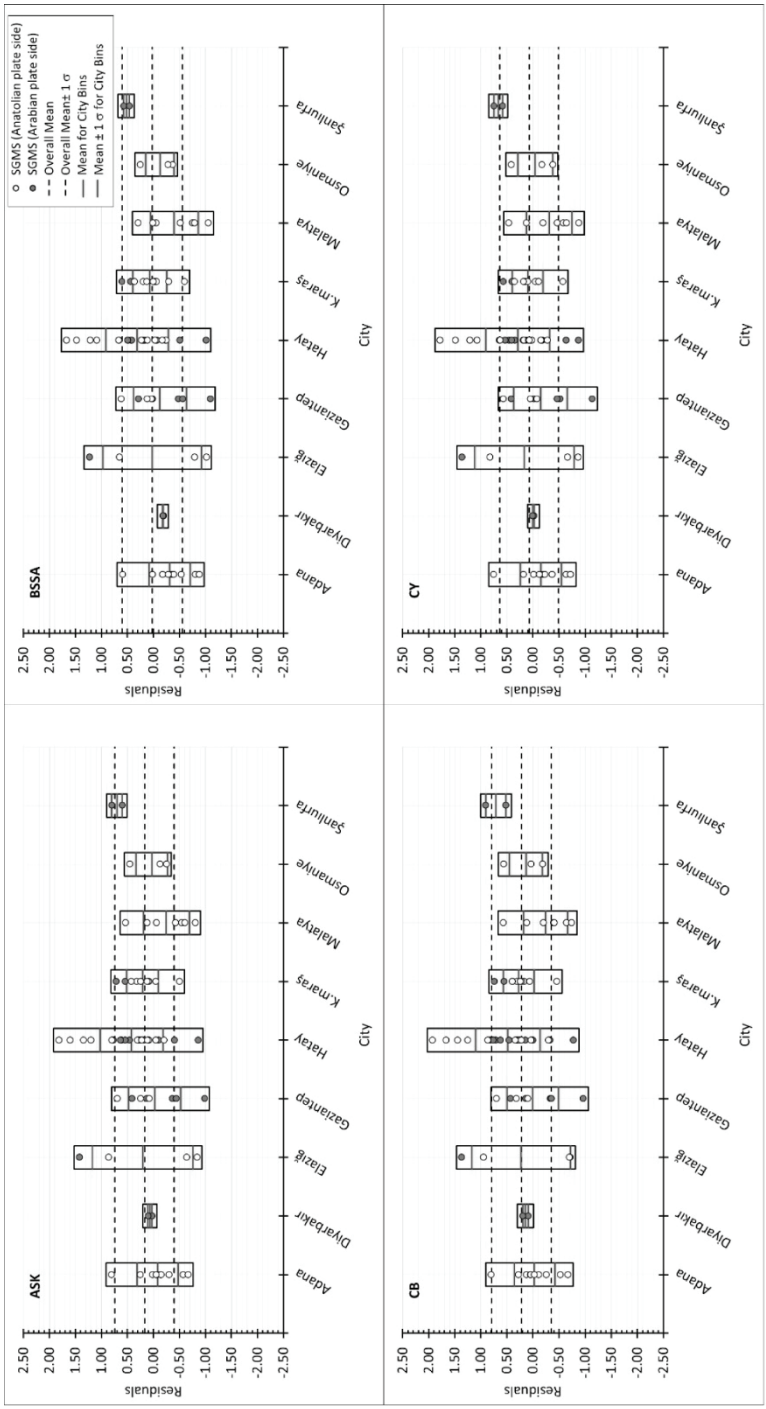

Figure 4 - PGA residuals estimated by the four GMPEs and their distribution with respect to the cities, where SGMSs are located.

Variability in PGA Residuals with Distances to the Rupture Plane

In Figure 5, PGA residuals are presented against R_{jb} distances, and SGMSs, located on the Anatolian and Arabian plate sides of the rupture, are shown by circles and dots, respectively. The trend lines for their residuals are shown by red and green lines, respectively. Table 3 presents a summary of mean ± σ residuals estimated separately for three R_{jb} bins: less than or equal to 10 km, in between 10 and 50 km, and greater than 50 km. Various bin thresholds were tested to identify meaningful trends in the data. After evaluating several options, these thresholds were selected due to their superior observed trends. These bins were also observed to be consistent with the distance attenuation response expected during a M7.8 event.

Table 3 - A summary of mean ± 1 σ residuals estimated separately for three different bins: i) $R_{jb} \leq 10$ km, ii) 10 km < $R_{jb} \leq 50$ km and iii) $R_{jb} > 50$ km

GMPE	$R_{jb} \leq 10$ km	10 km< $R_{jb} \leq 50$ km	$R_{jb} > 50$ km
ASK	0.15 ± 0.43	0.29 ± 0.61	0.05 ± 0.57
CB	0.18 ± 0.42	0.35 ± 0.63	0.1 ± 0.57
CY	-0.02 ± 0.44	0.19 ± 0.6	-0.01 ± 0.57
BSSA	0.06 ± 0.43	0.18 ± 0.61	-0.17 ± 0.58

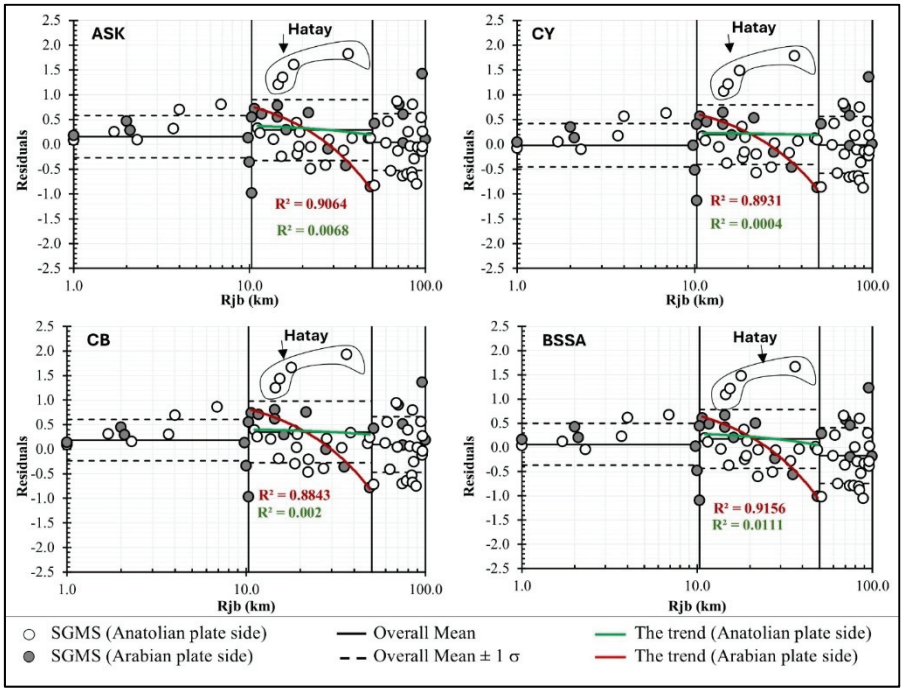

Figure 5 - PGA residuals for the four GMPEs and their distribution with respect to Rjb distances. The dashed lines in each plot show mean ± σ limits. Separated into three different bins: i) Rjb ≤ 10 km, ii) 10 km< Rjb ≤ 50 km and iii) Rjb > 50 km

Both Figure 5 and Table 3 reveal that the scatter in residuals increases for distances greater than 50 km, with a standard deviation around 0.6, indicating greater variability in predictions at longer distances. In contrast, distances less than 10 km show less scatter, with a standard deviation around 0.4, suggesting more consistent predictions close to the fault.

Additionally, the trend lines in Figure 5 show a strong decreasing trend in residuals with increasing R_{jb} for SGMSs on the Arabian plate side, particularly for stations located between 50 and 100 km. On the Anatolian plate side, the trend is very weak, with the highest residuals found at SGMSs stations 3135, 3129, 3126, and 3125, marked as outliers in Figure 5. These outliers are located in Hatay, where intense structural damage was observed. The differences in residual trends emphasize the significance of path effects on the recorded intensity levels.

Variability in PGA Residuals with V_{s30}

V_{s30} term is commonly used as a parameter to represent the effects of site response on the seismic demand levels. Figure 6 and Table 4 present the estimated residuals for each station grouped in terms of their V_{S30} values. On Figure 6, residuals are grouped into three bins, consistent with Turkish earthquake code-based soil site classifications scheme: ZB, ZC and ZD. It should be noted that TEC soil site classification scheme is almost identical with the one of NEHRP, and groups soil sites with $180 \leq V_{s30} < 360$, $360 \leq V_{s30} < 760$, and $760 \leq V_{s30} < 1500$ m/s, with site class symbols of ZD, ZC and ZB, respectively. Table 4 presents a summary of the statistics of the residuals estimated for each V_{S30} bin. Interpretation of Figure 6 and Table 4 reveals that the mean PGA residuals estimated by GMPES do not vary significantly with V_{S30}. The scatter (i.e.: standard deviation) in residuals is observed to be higher in stiffer sites ZC and ZB (i.e.: site class C and B in NEHRP), as compared to site class ZD.

Table 4 - A summary of mean ± 1 standard deviation residuals estimated separately for site class ZB, ZC and ZD by using NGA WEST-2 GMPEs

GMPE Model	$180 \leq V_{S30} < 360$ m/s ZD	$360 \leq V_{S30} < 760$ m/s ZC	$760 \leq V_{S30} < 1500$ m/s ZB
ASK	0.24 ± 0.46	0.15 ± 0.59	0.21 ± 0.66
CB	0.37 ± 0.44	0.19 ± 0.59	0.13 ± 0.67
CY	0.13 ± 0.44	0.05 ± 0.58	0.15 ± 0.66
BSSA	0.07 ± 0.49	0.00 ± 0.6.	0.11 ± 0.63

Variability in PGA Residuals with Azimuth Angle, θ

As discussed earlier, instead of the epicenter of the earthquake, the kink point of the fault rupture on the EAFZ, is used to assess the azimuth angle, θ, of the SGMSs. Figure 7 illustrates the dependency of the residuals on θ. An overall trend is evident across all GMPEs considered, wherein the residuals increase with decreasing θ angles. As the θ angle increases,

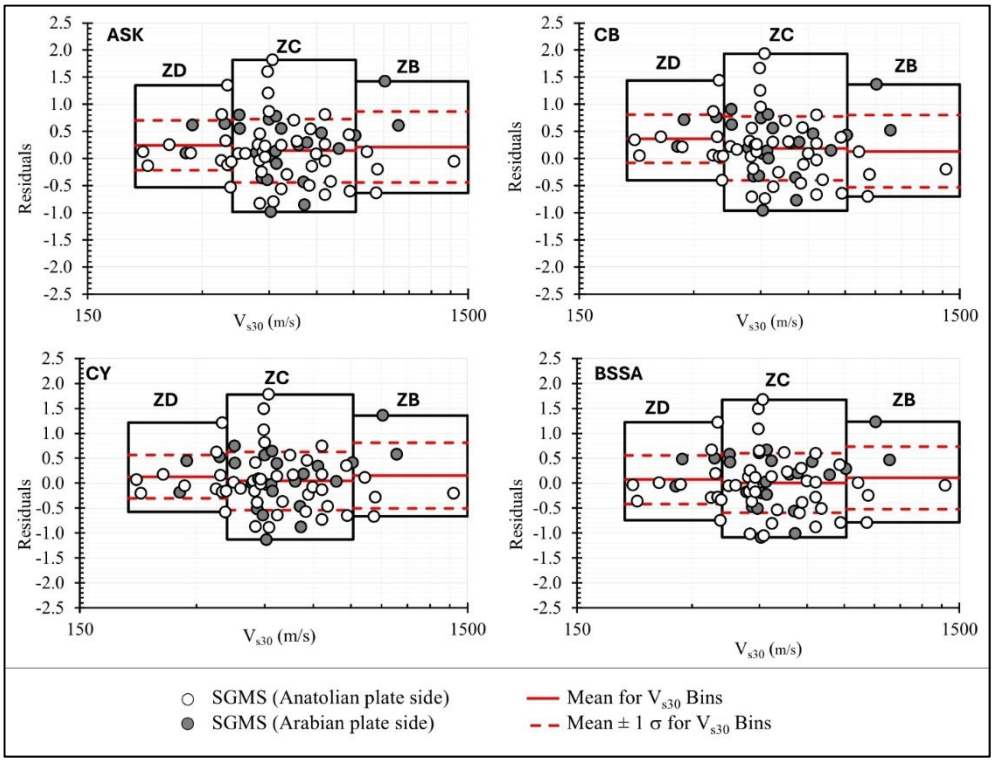

Figure 6 - PGA residuals for the NGA WEST-2 GMPEs, and their distributions with respect to VS30. The dashed lines in each plot show mean ± σ limits.

the scatter in residuals also decreases. In the literature, both directivity and rupture velocity (super vs. sub shear) effects are attempted to be represented by the azimuth angle between the fault plane and ray path rupture (Wang et al., 2016). Again, in the literature directivity effects are commonly accepted to affect longer period intensity levels but not PGAs (Somerville et al., 1997). Hence, the weak trend of PGA residuals increasing with decreasing θ is preliminarily attributed to rupture shear effects (speculated as super shear) as opposed to the directivity ones. However, this conclusion is premature and deserves further in-depth assessments, which is not within the scope of our preliminary reconnaissance evaluations.

Moreover, Supplementary Figures S.1 through S.4 provide a detailed geographical distribution of both the recorded PGA and the calculated residuals for each of the four GMP models. In these figures, the numbers shown at each SGMS represent the observed PGA value alongside the corresponding residual term, formatted as ($PGA_{recorded}$, $GMPE_{residual}$). This allows for a clear comparison between the recorded seismic activity and the predictions made by the ground motion models, highlighting areas where the models either underpredicted or overpredicted the actual ground motion.

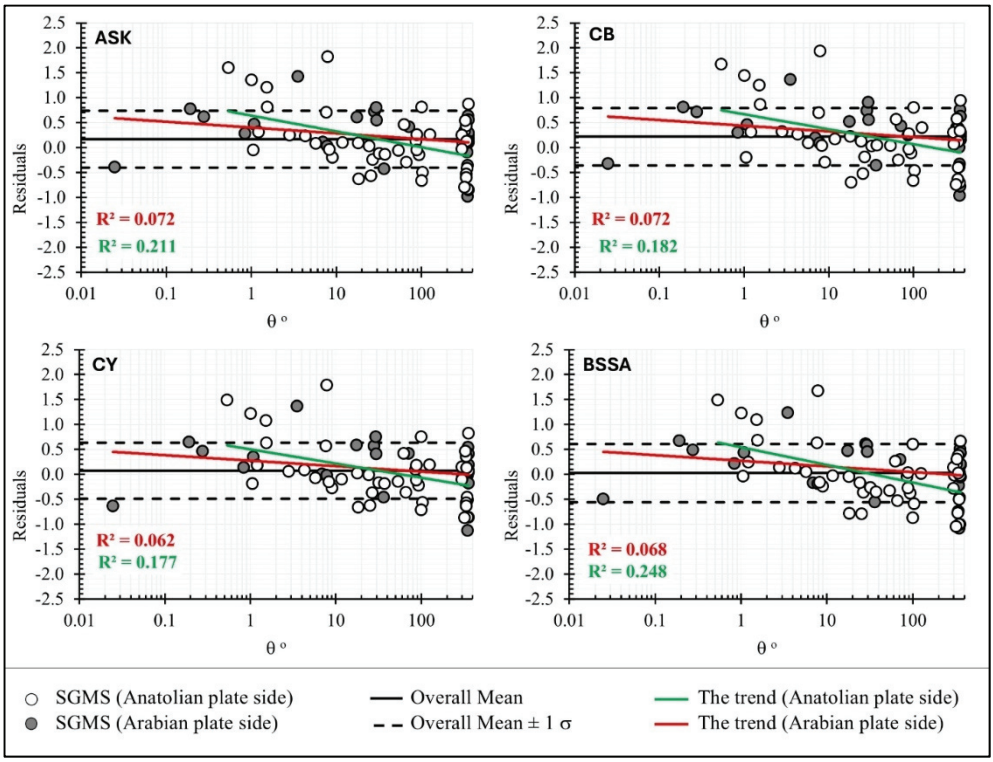

Figure 7 - PGA residuals for the NGA WEST-2 GMPEs, and their distribution with respect to ± σ The dashed lines in each plot show mean ± σ limits

Variability in PGA Residuals with Recorded PGAs

Figure 8 presents the estimated residuals varying with the recorded PGA levels. On the same figure the linear and nonlinear trends are shown separately for the stations located on the Anatolian and Arabian plate sides of the rupture. Valid for all four GMPE models, residuals increase with increasing recorded PGA levels. In simpler terms, the employed three GMPEs overpredicted lower PGA levels and underpredicted the higher ones. The residuals for the stations on the Anatolian plate side exhibited a more correlated residual trend with the recorded PGA intensity levels.

Comparisons of the Recorded vs. Predicted S_A's

The spectral acceleration (S_A) residuals were assessed consistent with Equation 1. The scatter in residuals is shown with respect to spectral period, T, in Figure 9. On the figure, black solid lines show the mean values. As revealed by Figure 9, ASK consistently underestimated the spectral acceleration demand in all period ranges. CY and BSSA GMPE models underpredicted the spectral acceleration demand for period longer than 0.2 and 0.06 seconds,

respectively. CB GMP model has approximately residuals 0 up to a period of 0.06s afterward the model starts to underpredict the spectral acceleration. The underpredictions and overpredictions reach as high as 30 % in T=1 second in CY.

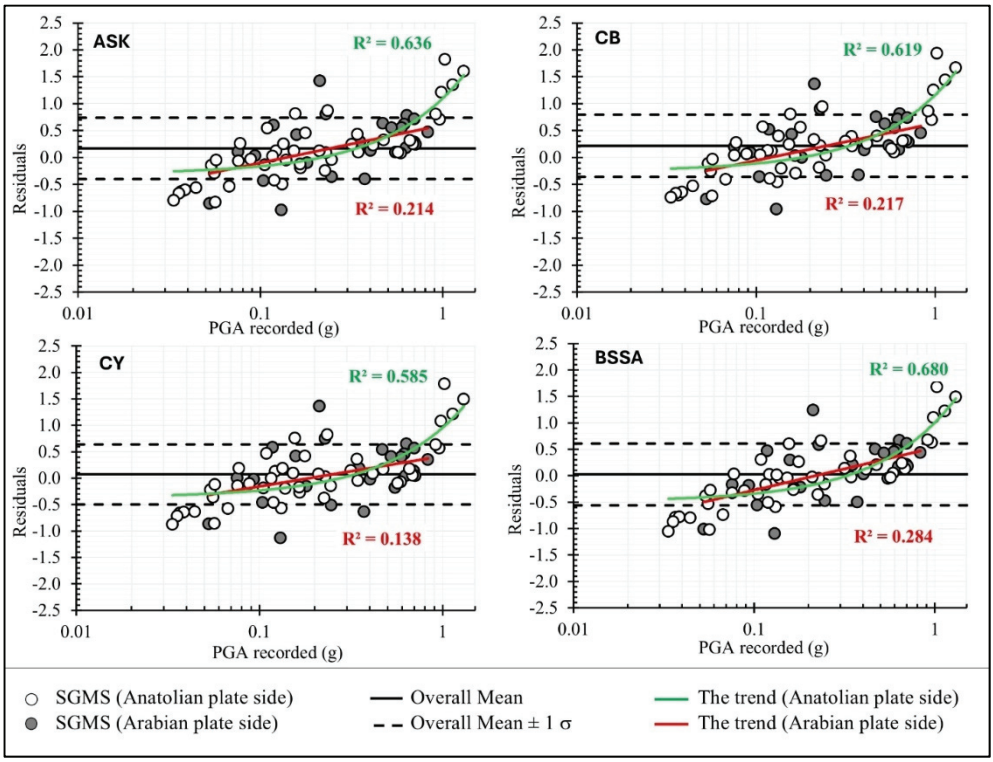

Figure 8 - PGA residuals for the NGA WEST-2 GMPEs and their distribution with respect to recorded PGAs. The dashed lines in each plot show mean ± σ limits

Comparisons of the Recorded vs. PGA and S_A Levels Recommended by Turkish Earthquake Code

Consistent with the Turkish Earthquake Design Code (TEC), the peak ground and spectral acceleration values were assessed for the design scenarios of DD-1 and DD-2, which correspond to the return periods of 2475 and 475 years, respectively. These values are compared with the recorded seismic demand levels at SGMS sites during the Kahramanmaraş-Pazarcık event. The results, as presented in Figure 10, and summarized in Table 2, reveal that the Turkish Earthquake Design Code DD-1 and DD-2 PGA levels were exceeded at 5 and 22, out of 71 stations, respectively. The exceedance of the design code could be attributed to site-specific conditions including soil-site, basin, directivity and rupture velocity effects, and the buildup of strain energies beyond design basis levels due to historical seismic gaps in the region. The stations, where the seismic PGA demand were exceeded, are class ZC or softer sites. PGA levels for the DD-1 seismic scenario were exceeded at SGMS

3135, 3125, 3129, 3126, and 3141, which are all located in the city of Hatay. The extensive structural damage levels witnessed in this city consistently supports this conclusion (Çetin et al., 2023a; Çetin and Ilgaç, 2023). On the basis of the residual trends provided in Figure 11, structures with spectral periods of 0.7 seconds and longer, were subjected to approximately 20 to 30 % higher seismic demands than the ones defined by TEC for the DD-2 design basis scenario. This is listed as one of the factors among many, contributing to the concentrated damage observed in residential buildings with number of stories higher than 5 to7 (Çetin et al., 2023a; Çetin and Ilgaç, 2023). While comparisons of recorded PGA levels with design values provide some context for the concentrated damage, it is also important to note that a single parameter alone is not sufficient to fully assess complex structural seismic responses, which may require multi-dimensional evaluations and involvement of experts from different disciplines. In the literature S_A and peak ground velocity (PGV) are suggested as the parameters better correlating with seismic structural performance, as they offer a more comprehensive understanding of the damage mechanisms (Avcil et al., 2023; Pinzón et al., 2024).

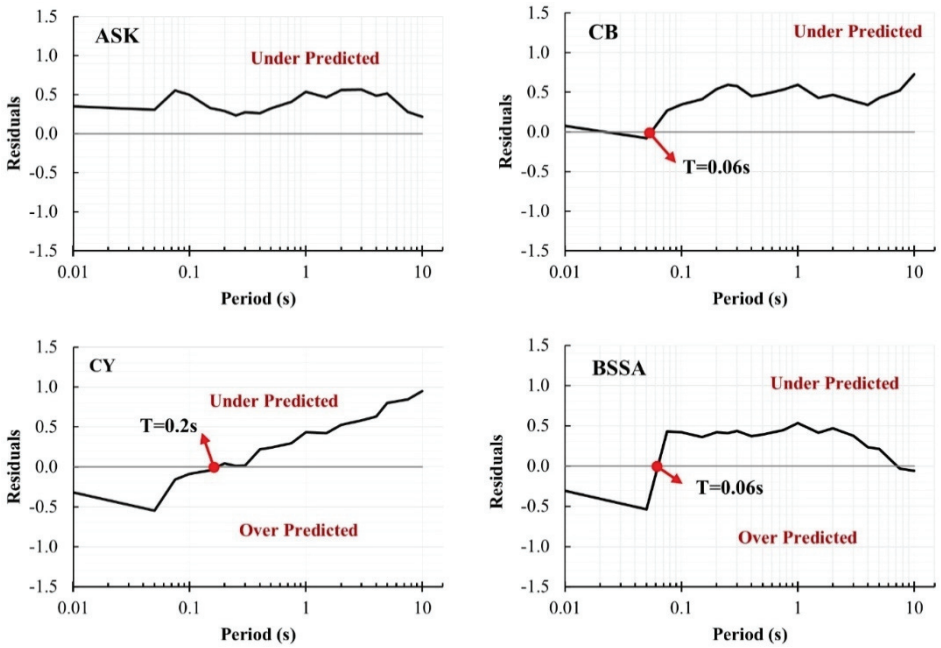

Figure 9 - SA residuals for the NGA WEST-2 GMPEs and their distribution with respect to spectral period (s).

Consistent with this discussion, Figure 11 represents the average spectral acceleration residuals of all stations calculated separately for each period. However, to provide a more detailed understanding, specific stations were selected for individual plotting on a detailed map, rather than averaging all SGMS spectral accelerations and comparing the average with the Turkish Earthquake Design Code. As mentioned earlier, several SGMS stations in Hatay

were identified as outliers, specifically stations 3135, 3125, 3129, and 3126, as shown in Figure 5. All of these stations are located on medium stiff soil, with shear wave velocities ranging from 350 m/s to 460 m/s. SGMS #3135 in Arsuz-Hatay recorded PGA values of 0.755 g (E-W), 0.601 g (N-S), and 0.166 g (U-D). SGMS #3125 in Antakya-Hatay recorded PGA values of 1.145 g (E-W), 0.839 g (N-S), and 1.158 g (U-D). SGMS #3129 in Defne-Hatay, which recorded the highest PGA levels during the event, reported values of 1.125 g (E-W), 1.138 g (N-S), and 0.731 g (U-D). SGMS #3126, also in Antakya-Hatay, recorded PGA values of 1.049 g (E-W), 1.234 g (N-S), and 1.091 g (U-D).

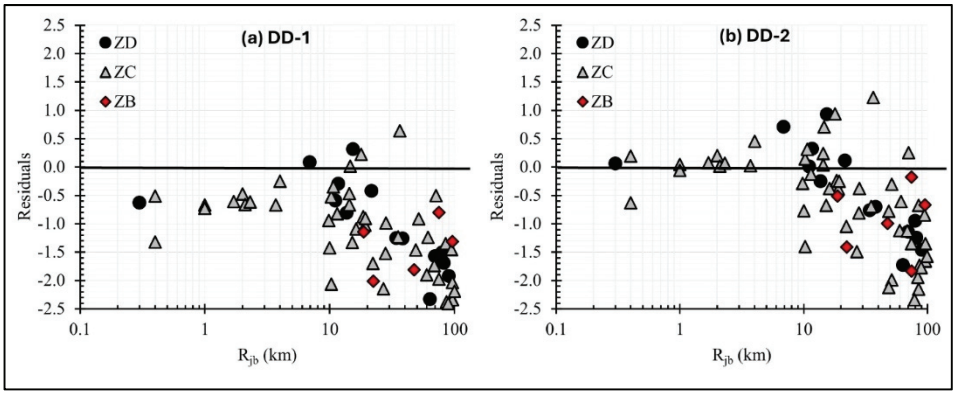

Figure 10 - PGA residuals estimated for the (a) TEC DD-1 (corresponds to a return period of 2475 years) and (b) TEC DD-2 (corresponds to a return period of 475 years) seismic scenario levels.

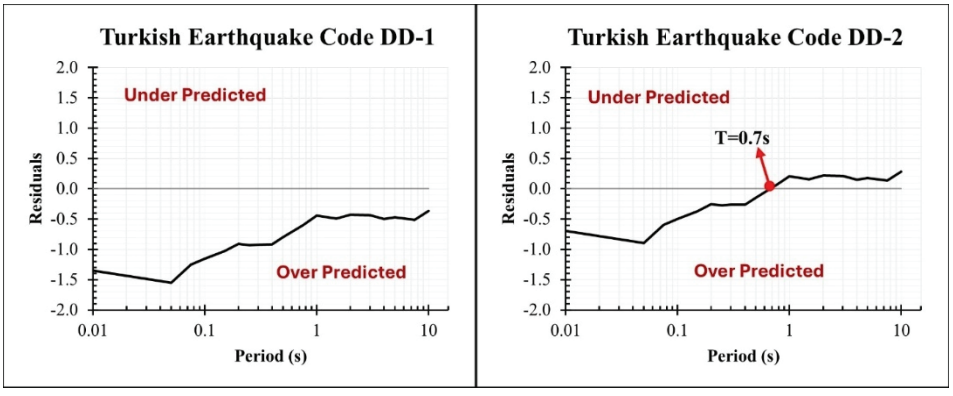

Figure 11 - SA residuals estimated for (a) TEC DD-1 (corresponds to a return period of 2475 years) and (b) TEC DD-2 (corresponds to a return period of 475 years) seismic scenario levels.

To better understand the underlying factors, elastic response spectra for these stations are shown in Figure 12. In this figure, the observed acceleration spectra are represented by solid

lines (black for the E-W spectral acceleration and red for the N-S), while the Turkish Earthquake Design Code spectra are indicated with blue dashed lines (DD-1 design-based scenario with a dashed line and DD-2 design-based scenario with a dash-dotted line). The map shows station locations with dots representing soil site class. It can be seen from the figure that at all four stations, the DD-2 design-based scenario was significantly exceeded. Notably, stations 3126 and 3129 exceeded the DD-1 scenario between the periods of 0.1-0.15 seconds, where the design spectra were approximately doubled. The significant deviations observed in these outlier stations underscore the influence of local site conditions and rupture dynamics on the seismic demands recorded in Hatay.

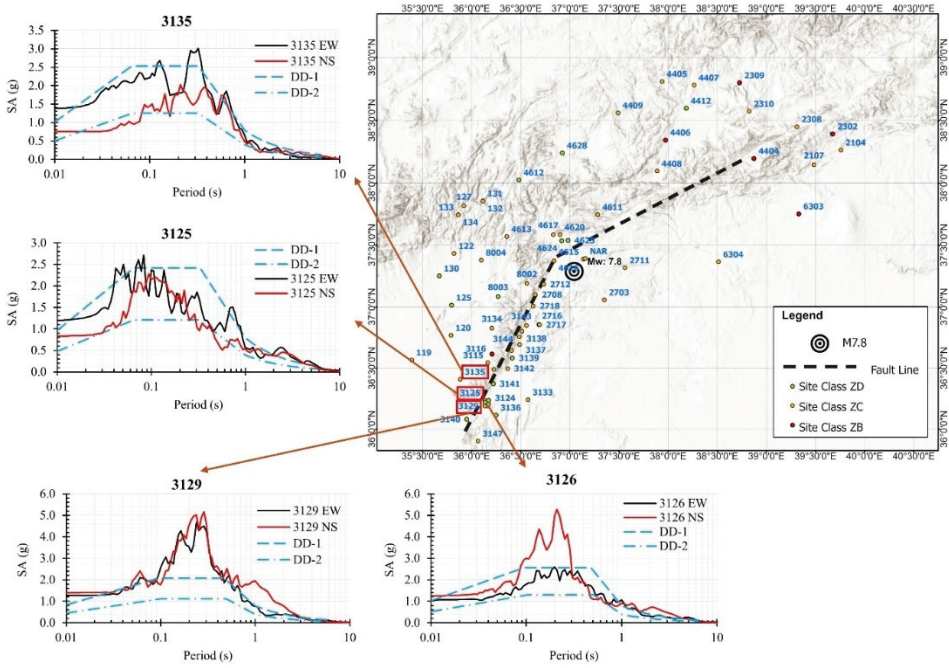

Figure 12 - Elastic response spectra for 3125, 3126, 3129 and 3135 SGM stations plotted on a map in relation to Turkish Earthquake Design Code.

SUMMARY AND CONCLUSION

This manuscript presents the findings of preliminary evaluations, which aim to comparatively assess the recorded spectral acceleration intensity levels during the February 6, 2023 Türkiye-Kahramanmaraş-Pazarcık earthquake, M7.8, with the ones i) predicted by four ground motion models from the 2014 NGA WEST-2 Ground Motion Prediction Equations (GMPEs): ASK, CB, CY, and BSSA.and ii) recommended by the Turkish Earthquake Design Code (TEC) for return periods of 475 and 2475 years.

Across all models, the most accurate predictions were made for the cities of Diyarbakır and Osmaniye. The cities of Adana, Malatya, and Gaziantep were shaken by PGA levels less intense than those predicted by the GMPEs. Contrary to these cities, ordered from the highest

to lowest positive residuals, Şanlıurfa, Hatay, Kahramanmaraş, and Elazığ were shaken by higher levels of PGA than what were predicted by the GMPEs. In the overall, among others, BSSA model provided the least unbiased predictions, producing the lowest overall mean residual. The overall mean ± σ residuals for the stations located on the east (Arabic plate side) and west (Anatolian plate side) of the fault rupture plane are estimated as 0.20 ± 0.66 and 0.14 ± 0.62, respectively. Hence, stations located on the Arabian plate side of the rupture are concluded to demonstrate more pronounced overpredicted residuals, whereas those situated on the Anatolian plate side of the fault exhibit a slightly better fit with less overprediction by the four GMPE models. The highest positive residual value is estimated for SGMS # 3135 in Hatay, where the most structural damage was concentrated.

The PGA residuals exhibited trends suggesting a strong decreasing trend in residuals with increasing R_{jb} for SGMSs on the Arabian plate side, particularly for stations located between 50 and 100 km. On the Anatolian plate side, the trend is very weak, with the highest residuals found at SGMSs stations 3135, 3129, 3126, and 3125, marked as outliers in Figure 5. These outliers are located in Hatay, where intense structural damage was observed.

In general, PGA residuals are observed to decrease with increasing rupture distances. The mean residuals among different GMPEs do not vary significantly with V_{S30}. The scatter (i.e.: standard deviation) in residuals, though, is observed to be the highest for site class ZC (i.e.: site class C in NEHRP). Valid for all four GMPE models, the PGA residuals increase with increasing recorded PGA levels. In simpler terms, the employed four GMPEs overpredicted lower PGA levels and underpredicted the higher ones. The residuals for the stations on the Anatolian plate side exhibited a more correlated residual trend with the recorded PGA levels. The dependency of the residuals on azitmuth angle, θ, was also assessed. An overall trend is evident across all GMPEs considered, wherein the residuals increase with lower θ angles, and as the θ angle increases, the residual PGAs decrease, and the scatter is reduced.

The spectral acceleration residuals were also assessed. The spectral acceleration demand across all period ranges was underestimated by ASK GMPE model. The CY and BSSA models provided underpredicted spectral intensities for periods longer than 0.2 and 0.06 seconds, respectively. The CB GMPE model had near-zero residuals up to 0.06 seconds, but underpredicted spectral acceleration values beyond it. The magnitude of underpredictions reach as high as 30 % at T=1 second for the predictions by CY.

The peak ground and spectral acceleration values were assessed for the Turkish Earthquake Design Code seismic scenarios of DD-1 and DD-2, which correspond to return periods of 2475 and 475 years, respectively. DD-1 and DD-2 PGA levels were exceeded at 5 and 22 out of 71 stations, respectively. The stations, where the seismic PGA demand was exceeded are all site class ZC or softer sites. PGA levels for the DD-1 seismic scenario were exceeded at stations 3135, 3125, 3129, 3126, and 3141, which are in all located in the city of Hatay. This is listed as one of the factors among many, contributing to the concentrated damage observed in Hatay City (Çetin et al., 2023a; Çetin and Ilgaç, 2023). While comparisons of recorded strong ground motion intensity levels with design values provide some context for assessing the observed damage levels, it is not sufficient to fully understand the underlying list of other factors. It is important to note that the structural seismic performance assessments require complex, multi-dimensional evaluations, and the involvement of engineering experts from a wide range of disciplines. Moreover, there may be other seismic demand parameters such as

PGV, which may correlate better with structural performance than PGA or S_A parameters. Hence, over-generalizations of our preliminary conclusions are discouraged.

Statement and Declarations

Acknowledgements

We would like to acknowledge the partial funding provided for the fieldwork by The Scientific and Technological Research Institution of Türkiye (TÜBİTAK) "1002-C Natural Disasters-Focused Fieldwork Emergency Support Program (Doğal Afetler Odaklı Saha Çalışması Acil Destek Programı)".

Funding: This work is partially supported by The Scientific and Technological Research Institution of Türkiye (TÜBİTAK) "1002-C Natural Disasters-Focused Fieldwork Emergency Support Program (Doğal Afetler Odaklı Saha Çalışması Acil Destek Programı)".

Competing Interests: The authors have no relevant financial or non-financial interests to disclose.

Author Contributions: Material preparation, data collection and analyses were performed by Kemal Önder Çetin and Alaa Elsaid and A. Arda Özacar. The manuscript was drafted by Kemal Önder Çetin, and Alaa Elsaid and A. Arda Özacar commented on the draft. All authors read and approved the final version of the manuscript.

Data availability: The datasets generated during and/or analyzed during the current study are available in the provided references and can also be provided by the corresponding author upon reasonable request.

References

[1] Abrahamson, N., and W. Silva (2008). Summary of the Abrahamson & Silva NGA Ground-Motion Relations, Earthquake Spectra 24, no. 1, 67–97, doi: 10.1193/1.2924360.

[2] AFAD - TADAS (n.d.): <https://tadas.afad.gov.tr>.

[3] Ambraseys, N. N. (1989). Temporary seismic quiescence: SE Turkey, *Geophysical Journal International* 96, no. 2, 311–331, doi: 10.1111/j.1365-246x.1989.tb04453.x.

[4] Avcil, F. et al. (2023) Effects of the February 6, 2023, Kahramanmaraş earthquake on structures in Kahramanmaraş City', Natural Hazards, 120(3), pp. 2953–2991. doi:10.1007/s11069-023-06314-1.

[5] Campbell, K. W., and Y. Bozorgnia (2023). Ground-motion model for the standardized version of cumulative absolute velocity, *Earthquake Spectra* 39, no. 1, 634–652, doi: 10.1177/87552930221144063.

[6] Chiou, B. S.-J., and R. R. Youngs (2014). Update of the Chiou and Youngs NGA Model for the Average Horizontal Component of Peak Ground Motion and Response Spectra, *Earthquake Spectra* 30, no. 3, 1117–1153, doi: 10.1193/072813eqs219m.

[7] Chiou, B., R. Darragh, N. Gregor, and W. Silva (2008). NGA Project Strong-Motion Database, *Earthquake Spectra* 24, no. 1, 23–44, doi: 10.1193/1.2894831.

[8] Çetin, K. Ö., M. Ilgaç , and E. Çakır (2023a). Preliminary Reconnaissance Report on February 6, 2023, Pazarcık Mw=7.7 and Elbistan Mw=7.6, Kahramanmaraş-Türkiye Earthquakes, METU/EERC 2023-01. doi: 10.13140/RG.2.2.32975.97446, Middle East Technical University Earthquake Engineering Research Center (METU EERC).

[9] Çetin, K. Ö., J. Bray , A. Frost , E. Miranda , R. Moss , and J. Stewart (2023b). February 6, 2023 Türkiye Earthquakes: Report on Geoscience and Engineering Impacts, https://10.18118/G6PM34, GEER Association Report 082.

[10] Çetin, K. Ö., and M. Ilgaç (2023). Reconnaissance Report on February 6, 2023 Kahramanmaraş-Pazarcık (Mw=7.7) and Elbistan (Mw=7.6) Earthquakes, 10.13140/RG.2.2.15569.61283/1., Türkiye Earthquake Reconnaissance and Research Alliance, Türkiye.

[11] Duman, T. Y., and Ö. Emre (2013). The East Anatolian Fault: geometry, segmentation and jog characteristics, *Geological Society, London, Special Publications* 372, no. 1, 495–529, doi: 10.1144/sp372.14.

[12] Kwiatek, G., P. Martínez-Garzón, D. Becker, G. Dresen, F. Cotton, G. Beroza, D. Acarel, S. Ergintav, and M. Bohnhoff (2023). Months-long preparation of the 2023 MW 7.8 kahramanmaraş earthquake, Türkiye, *Research Square preprint* , doi: 10.21203/rs.3.rs-2657873/v1.

[13] Massa, M., Pacor, F., Luzi, L., Bindi, D., Milana, G., Sabetta, F., Gorini, A., & Marcucci, S. (2010). The Italian Accelerometric Archive (ITACA): processing of strong-motion data. Bulletin of Earthquake Engineering, 8, 1175–1187. DOI: 10.1007/s10518-009-9152-3

[14] McClusky, S., S. Balassanian, A. Barka, C. Demir, S. Ergintav, I. Georgiev, O. Gurkan, M. Hamburger, K. Hurst, H. Kahle, *et al.* (2000). Global Positioning System constraints on plate kinematics and dynamics in the eastern Mediterranean and Caucasus, *Journal of Geophysical Research* 105, no. B3, 5695–5719, doi: 10.1029/1996jb900351.

[15] Melgar, D., T. Taymaz, A. Ganas, B. Crowell, T. Öcalan, M. Kahraman, V. Tsironi, S. Yolsal-Çevikbil, S. Valkaniotis, T. S. Irmak, *et al.* (2023). Sub- and super-shear ruptures during the 2023 Mw 7.8 and Mw 7.6 earthquake doublet in SE Türkiye, *Seismica* 2, no. 3, doi: 10.26443/seismica.v2i3.387.

[16] Luzi, L., Puglia, R., Russo, E., D'Amico, M., Felicetta, C., Pacor, F., Lanzano, G., Çeken, U., Clinton, J., Costa, G., Duni, L., Farzanegan, E., Gueguen, P., Ionescu, C., Kalogeras, I., Özener, H., Pesaresi, D., Sleeman, R., Strollo, A., & Zare, M. (2016). The Engineering Strong-Motion Database: A Platform to Access Pan-European Accelerometric Data. Bulletin of Earthquake Engineering.

[17] Okay, H. B., & Özacar, A. A. (2023). A Novel VS30 Prediction Strategy Taking Fluid Saturation into Account and a New VS30 Model of Türkiye. Bulletin of the Seismological Society of America, 114(2), 1048–1065. https://doi.org/10.1785/0120230032

[18] Okuwaki, R., Y. Yagi, T. Taymaz, and S. P. Hicks (2023). Multi-Scale Rupture Growth With Alternating Directions in a Complex Fault Network During the 2023 South-Eastern Türkiye and Syria Earthquake Doublet, *Geophysical Research Letters* 50, no. 12, doi: 10.1029/2023gl103480.

[19] Pacor, F., Paolucci, R., Luzi, L., Sabetta, F., Spinelli, A., Gorini, A., Nicoletti, M., Marcucci, S., Filippi, L., & Dolce, M. (2011). Overview of the Italian strong motion database ITACA 1.0. Bulletin of Earthquake Engineering, 9, 1723–1739. DOI: 10.1007/s10518-011-9327-6

[20] Petersen, G. M., P. Büyükakpinar, F. O. Vera Sanhueza, M. Metz, S. Cesca, K. Akbayram, J. Saul, and T. Dahm (2023). The 2023 Southeast Türkiye Seismic Sequence: Rupture of a Complex Fault Network, *The Seismic Record* 3, no. 2, 134–143, doi: 10.1785/0320230008.

[21] Picozzi, M., and A. Iaccarino (n.d.). The preparatory process of the 2023 MW 7.8 Turkey earthquake, *preprint*, doi: 10.21203/rs.3.rs-2619572/v1.

[22] Avcil, F. et al. (2023) Effects of the February 6, 2023, Kahramanmaraş earthquake on structures in Kahramanmaraş City, Natural Hazards, 120(3), pp. 2953–2991. doi:10.1007/s11069-023-06314-1.

[23] Somerville, P. G., N. F. Smith, R. W. Graves, and N. A. Abrahamson (1997). Modification of Empirical Strong Ground Motion Attenuation Relations to Include the Amplitude and Duration Effects of Rupture Directivity, *Seismological Research Letters* 68, no. 1, 199–222, doi: 10.1785/gssrl.68.1.199.

[24] Turkish Building Earthquake Code (2018), T.C. Resmi Gazete. , Ankara, Türkiye.

[25] Wang, D., J. Mori, and K. Koketsu (2016). Fast rupture propagation for large strike-slip earthquakes, *Earth and Planetary Science Letters* 440, 115–126, doi: 10.1016/j.epsl.2016.02.022.

[26] Zahradník, J., F. Turhan, E. Sokos, and F. Gallovič (2023). Asperitylike (segmented) structure of the 6 February 2023 Turkish earthquakes, *preprint*, doi: 10.31223/x5t666.

Turkish Journal of Civil Engineering, 2025, 53-80, Yazı 799, ***Araştırma Makalesi***

Moment Aktaran Kaynaklı Birleşimlerde Kullanılan Kaynak Yöntemlerinin Birleşim Performansına Etkisi

Hüdai KAYA[1*]
Barlas Özden ÇAĞLAYAN[2]

ÖZ

Özellikle moment aktaran yüksek sünek yapısal çelik çerçevelerde hedeflenen enerji sönüm seviyelerine ulaşılabilmesi, birleşimi oluşturan tüm elemanların tasarlandığı şekilde çalışmaları ile mümkündür. Bu araştırmaya konu olan deneysel çalışma, ülkemizde yapısal çelik sektöründe çoğunlukla tercih edilen üç farklı kaynak yöntemi üzerinde yapılmış ve yapısal çelik tasarım, imalat ve montaj konularında çalışan tüm meslektaşlarımız için halihazırdaki gri alanların azaltılmasına yönelik bir farkındalık oluşturmak amacı ile gerçekleştirilmiştir. İki farklı boyda üçer numuneden toplamda 18 adet tam ölçekli numune testini takiben mevcut yönetmeliğin ilgili tanım ve şartlarında iyileştirmeler ve değişiklikler yapılmasını işaret eden sonuçlar elde edilmiş bu anlamda daha ileri seviyede araştırma yapılmasının gereklilik olduğu kanaatine varılmıştır.

Anahtar Kelimeler: Yapısal çelik, kaynak, süneklik, tam ölçekli test, moment aktaran çerçeve, deprem, tekrarlı yükleme.

ABSTRACT

Influence of Welding Methods on the Performance of Welded Moment Frame Connections

Achieving the targeted levels of energy dissipation, especially in ductile structural steel moment frames, is possible by ensuring that all components forming the assembly function as designed. The experimental study discussed in this research was conducted on three different welding methods, which are widely preferred in the structural steel sector in Türkiye. The aim was to create awareness and reduce existing uncertainties for all our colleagues working in structural steel design, manufacturing, and assembly. Following the

Not: Bu yazı
- Yayın Kurulu'na 24 Temmuz 2024 günü ulaşmıştır. 19 Eylül 2024 günü yayımlanmak üzere kabul edilmiştir.
- 31 Mayıs 2025 gününe kadar tartışmaya açıktır.

- https://doi.org/10.18400/tjce.1521635

1 İstanbul Teknik Üniversitesi, İnşaat Mühendisliği Bölümü, İstanbul, Türkiye
kayah18@itu.edu.tr - https://orcid.org/0000-0002-4221-4408

2 İstanbul Teknik Üniversitesi, İnşaat Mühendisliği Bölümü, İstanbul, Türkiye
caglayan@itu.edu.tr - https://orcid.org/0000-0002-8986-9188

* Sorumlu yazar

testing of 18 full-scale specimens, improvements and changes were indicated in the relevant definitions and conditions of the existing regulations, suggesting the necessity for further advanced research in this regard.

Keywords: Structural steel, weld, ductility, full scale test, moment frame, earthquake, cyclic loading.

1. GİRİŞ

Kaynak teknolojisindeki gelişmelerle birlikte bulon ve perçine göre daha hızlı ve ekonomik bir birleşim aracı olması sebebi ile kaynağın günümüzde yapısal çelik sistemlerde diğer iki birleşim elemanına göre daha çok tercih edildiğini görmekteyiz. Ancak kullanılan metot, detay, imalat ve montaj teknikleri ile çevresel şartlar sebebi ile oluşan veya süreksizlik, çatlak, artık gerilme yığılmaları, mekanik veya metalürjik kusurlar gibi bırakılan hasar sebebi ile ilgili elemanın tasarlanan taşıma gücüne, enerji yutabilme ve plastik mafsal oluşturabilme yeteneğine ulaşmadan yerel ya da tamamen göçtüğü diğer bir değişle sihirli ve mükemmel bir birleşim aracı olmadığı defalarca ispatlanmış ve tecrübe edilmiştir.

Sünek yapı kabulünün tek başına ve münferiden kolon ve kiriş olarak ilgili yapı elemanı veya elemanlarının sünek olma özelliği ile veya tasarımda kabul edilen parametreler ile sağlanamayacağı 1994 yılında A.B.D. Northridge bölgesinde meydana gelen ve sadece 10 sn süren 6,7 büyüklüğündeki deprem ile ortaya çıkmıştır. Depremin hemen sonrasındaki ilk kontrollerde çelik yapılarda önemli bir hasar oluşmadığı izlemini olmuş ancak o dönemdeki yapı yönetmeliği doğrultusunda yaygın olarak kullanılan kolon-kiriş birleşimlerinin özellikle kiriş başlıklarını kolon başlığına bağlayan kaynak dikişleri civarında çatlaklar oluştuğu gözlenmiş ve Northridge depremi öncesi bir çok deneysel ve analitik çalışmalar sonucu kabul görerek tasarım yönetmeliklerine giren ve kullanılması önerilen bu birleşim detayı, deprem sonrasında yayınlanan acil bir raporla, yönetmeliklerden çıkarılmıştır [1].

Ülkemizde yapılmakta olan yapısal çelik yapıların birleşim detay imalatlarında ağırlıklı olarak 3 tip kaynak yöntemi kullanılmakta, proje özel şartnamesi doğrultusunda da bu kaynak yöntemlerinin alt parametreleri tayin edilmektedir. Söz konusu yöntemlerin ve bunların alt parametrelerinin seçimi, ilgili kaynak nüfuziyetini ve sünekliğini tayin edeceğinden, doğrudan birleşimin sünekliğini ve düşük çevrimli yorulma ömrünü etkilemektedir. Bu sebeple sünek bir birleşimden bahsediliyorsa sadece o birleşimde bir araya gelen elemanların sünekliği değil, bir bütün olarak birleşimin sünekliğinden bahsedilme zorunluluğu ve gerekliği sebebi ile kolon ve kirişin dışında ilgili birleşimde yer alan kaynağın da birleşimin bir eleman olarak kabul edilerek tayini, tasarımı ve teşkili önem taşımaktadır.

Kaynak metodu ve alt sınıfının seçimi çoğu kez atölyenin inisiyatifine bırakılmakla birlikte, nadiren ve özellik teşkil eden bazı yapılar için proje özel teknik şartnamesinin bir alt başlığı olarak yapısal çelik proje müellifi tarafından tayin edilmektedir.

Atölye inisiyatifine bırakılan kaynaklarda ise atölyenin, mühendislik detayının gereksinimlerinden bihaber olarak, maliyet merkezli, minimum malzeme bedeli, minimum işçilik ile maksimum iş prensibi doğrultusunda seçim yapılmasını beklemek hiç de zor değildir.

Bu araştırma için 2018 yılı Türkiye Bina Deprem Yönetmeliği [2] kapsamında "Tam Dayanımlı Bulonlu Alın levhalı Birleşimler" Madde 9B.2' de yer alan rijitlik levhasız, 4 bulonlu, alın levhalı birleşim referans alınarak test numuneleri üretilmiş, iki farklı boyda, her boy ve her kaynak tipi için 3'er numune olmak üzere toplam 18 adet numune test edilmiştir. Numunelerin üretimi için kullanılan kaynak metotlarına ait detaylar "Test Planlaması" başlığı altındaki ikinci bölümde verilmiştir.

Araştırma kapsamında yapılan literatür incelemesi sırasında, bir birleşim elemanı olarak kullanılan kaynak metoduna veya kaynak metodunun performansına ait bir çalışmaya rastlanmamıştır.

Konu çevresinde yapılan araştırmalar tipik olarak; kaynak erişim deliğinin geometrisi ve boyutu, panel bölgesinin deformasyon kontrolü, kiriş gövde kaynağının birleşim performansına katkısı ve bunların inelastik performans üzerindeki katkıları [3], farklı gerilme hızları altında küt ve köşe kaynakların dinamik davranışları [4], S355 yapı çeliğinin HAZ ve kaynak metali bölgelerinin muhtelif gerilme hızlarında yarı statik ve dinamik çekme testleri altındaki davranışları [5], moment çerçevesinde yer alan kirişin başlıklarındaki tek berkitmenin plastik dönmeye katkısı [6], kaynaklı moment çerçevelerinde et kalınlığı yönünden kolon flanşının yüksek ısı girişli kaynak altında yüksek gerilme hızları ile kolon flanşındaki üç eksenli gerilme durumu [7], moment çerçevelerinde kaynaklı kolon kirş birleşimlerinin çelik sınıfı, yükleme hızı, köşe kaynak, tek ve çift eğimli düz kaynaklar açısından monolitik ve çevrimsel yükleme altındaki davranışları [8], 1994 Northridge depremi sonrası kaynaklı moment çerçevelerin sismik performanslarının yükseltilmesi ve iyileştirilmesi [1], moment çerçevelerinde yer alan kaynaklı kolon kiriş birleşimlerinin farklı kiriş flanş berkitme plakaları ile davranışları [9], moment bağlantılarının mukavemetini ve sünekliğini etkileyen kaynak metali kırılma tokluğu, kaynak erişim deliğinin geometrisi ve boyutu ile panel bölgesi deformasyon kontrolü [10], 1994 Northridge ve 1995 Hyogoken-Nanbu depremleri sonrasında Amerika ve Japonya'daki mevcut moment çerçeveli yapıların hasarlarının gözden geçirilmesi ve karşılaştırması [11], moment çerçevelerinde kaynaklı flanş bağlantılı kirişlerin inelastik davranışları ve süreklilik plakalarının etkinliği [12], 1994 Northridge depremi sonrası kaynaklı bağlantıların kırılgan hasarlarının incelenmesi ve sünekliğin artırılması [13] konularında yoğunlaşmış, ilgili sayısal ve deneysel çalışmalara ait yayınlar incelenmiştir.

Üretilen tüm numuneler için ilgili imalat standardı [14] doğrultusunda imalat öncesinde, imalat sırasında ve sonrasında atölye, işçilik ve malzeme sertifikasyonları, çekme, kimyasal kompozisyon, sertlik, kaynak pasoları arası sıcaklık, çatlak kontrol, nüfuziyet ve kaynak hatalarına karşı radyografi testleri içeren kalite kontrol testleri akredite bir laboratuvar, sertifikalı ekipman ve lisanslı inspektörler aracılığı ile yapılmış, kayda alınmıştır

Her üç grup test numunesi için FEMA350/SAC2000 [15] yükleme protokolü kullanılmış, elde edilen sonuçlar karşılaştırmalı olarak irdelenmiştir.

1.1. Kaynak ve Kaynak Metotları

İki veya daha fazla parçanın ısı, basınç veya her ikisi birden kullanılarak birleştirilmesi işlemine kaynak adı verilmektedir. Bu, metal ve metal dışı tüm malzemeleri kapsayan

oldukça geniş bir tanım olup bu çerçevede onlarca farklı yöntem ve usulde kaynak işlemi mümkündür.

Yapısal çelik mühendisliği açısından yaklaşılacak olursa, ülkemizdeki imalat ve montajlarda aşağıda kısa tanımları verilen üç ana tip kaynak yöntemi kullanılmaktadır.

a) Gazaltı Ark Kaynağı

Gaz Metal Ark Kaynağı / Gas Metal Arc Welding / Metal Inert Gas (GMAW/MIG), kaplamasız sürekli bir tel elektrod ile ana metal malzeme (iş parçası) arasında koruyucu gaz altında elektrik arkı oluşturularak ana malzemenin eriyip birleşmesini sağlayan bir kaynak yöntemidir. Kaynak banyosunun içerisinde kullanılan elektrod da ergimiş olarak yer alır. Koruyucu atmosfer olarak asal veya yarı asal gazlar kullanılmaktadır.

Koruyucu atmosfer olarak Argon (Ar), Helyum (He) gibi soygazların kullanılması durumunda yöntem adı MIG, CO_2 gibi aktif gaz veya CO_2-Ar, CO_2-Ar-O_2 gibi karışım gazlar kullanılması halinde yöntem Metal Aktif Gaz / MAG olarak adlandırılır.

Gaz altı kaynağı ana başlığı altında bir başka bir yöntem de Özlü Tel Ark Kaynağı / Flux Cored Arc Welding (FCAW) olarak adlandırılan ve kullanılan tel dışında diğer tüm özellikleri MIG ile aynı olan bir kaynak yöntemidir. Kullanılan telin içi dolgulu olup MIG yöntemine göre tek pasoda daha fazla kaynak dolgusu bırakır. Kaynak banyosuna sağladığı enerji girişi daha yüksektir. Teknik olarak aynı gazlar, koruyucu atmosfer olarak kullanılabilir. Alternatif olarak, atmosferik korumaya ihtiyaç duymayan kendinden korumalı FCAW-S tipi tel kullanımı da mevcuttur.

Yine gazaltı kaynağı ana başlığı altına değerlendirilebilecek diğer bir yöntem de Gaz Tungsten Ark Kaynağı / Gas Tunsten Arc Welding (GTAW) veya Tunsten Inert Gas (TIG) olarak adlandırılan ve ince et kalınlıkları, paslanmaz çelik ve demir dışı metal kaynaklarında tercih edilen kaynak türüdür. Burada elektrod olarak tungsten, koruyucu atmosfer olarak ise Argon veya Helyum gibi asal gaz kullanılır. GMAW yönteminin aksine tungsten elektrod kaynak banyosu içerisine dahil olmaz. Kaynak banyosuna enerji girdisi daha düşüktür. İşçiliği diğer yöntemlere göre daha fazla özen ve hassasiyet ister.

Tekniği gereği soğukta şekil verilmiş ince cidarlı çelik eleman, ince et kalınlıklı boru, kutu veya paslanmaz çelik imalatlarında kullanılmaktadır.

b) Örtülü Elektrod Ark Kaynağı

Günümüzde Örtülü Metal Ark Kaynağı / Shielded Metal Arc Welding (SMAW) ismi ile literatüre geçen ve Elektrik Kaynağı, Elektrod Kaynağı gibi kısaltılmış isimler ile kullanılan kaynak yönteminde, kaynak dikişinin mekanik parametrelerini iyileştirmek amacıyla kullanılan bir örtü tabakası çubuk elektrod parçası üzerinde sarma, daldırma veya günümüz teknolojisinde daha çok tercih edilen ekstrüzyon tekniği ile kaplanmış olarak kullanılmaktadır.

Elektrik enerjisi kullanılarak ana metal ile elektrod arsında ark oluşturularak yoğun bir ısı transferi ile ergitilmiş olan ana metale kaynak banyosuna elektrod da eriyerek dahil olmaktadır.

Kaynak banyosunun fiziksel ve mekanik özellikleri, örtü cinsine bağlı olarak değişmektedir. Kaynak dikişinin ana metal içerisine yapacağı nüfuziyet derinliği, kırılma tokluğu, çentik

darbe mukavemeti, akma ve kopma mukavemetleri, yığılan kaynak metali miktarı, birleşime etki eden enerji miktarı, kaynak dikişinin fiziksel görünümü gibi birçok husus örtü bileşiminin etkisi altındadır.

Örtüyü meydana getiren maddeleri birer başlık olarak görmek, örtünün kaynak banyosuna yukarıda sayılan fiziki ve mekanik etkileri nasıl oluşturduğu hakkında fikir vermesi açısından önemlidir.

1. Curuf teşkil eden maddeler
   A. Karbonatlar
   B. Silikatlar
   C. Oksitler
2. Arkı stabilize eden maddeler
3. Gaz atmosferi meydana getiren maddeler
4. Ekstrüzyon işlemini kolaylaştırıcı maddeler
5. Deoksidasyon ve alaşım maddeleri

Yukarıda ana başlıklar olarak verilen element ve bileşiklerin farklı oranlarda kullanılması ile örtünün karakteri değiştirilerek elektrodun kaynak banyosuna fiziki ve mekanik katkısı belirlenmekte, rutil, bazik, asit, oksit, zirkon bazik, selülozik karakterli örtülü elektrodlar bu üretimleri bu şekilde gerçekleştirilmektedir.

c) Tozaltı Ark Kaynağı

Tozaltı ark kaynak / Submerged Arc Welding (SAW) yöntemi tekniği bakımından gazaltı ark kaynağına benzer olup koruyucu atmosfer gaz yerine örtülü elektrodun manto/örtü tabakasını oluşturan maddelerden teşkil toz granül (flux) örtü malzemesi kaynak banyosu üzerine kaynak arkı oluşmadan önce serilmeye başlar. Arkı oluşturan ve eriyerek kaynak banyosu içerisine dahil olan elektrod bu granül örtü tabakası altında atmosferik etkilerden uzak olarak çalışır. Granül örtünün bir kısmı, kaynak işlemi sırasında oluşan ısı sebebi ile örtülü elektrod ark kaynağında olduğu gibi cüruf olarak katılaşır. Reaksiyona girmeyen ve toz halini koruyan örtü malzemesi ise vakumlu bir uç tarafından toplanır.

Gazaltı ark kaynağından diğer bir farkı da kullanılan elektrod çapının gazaltı tekniğinde kullanılanlara göre daha yüksek olmasıdır. Böylelikle kaynak metali yığılması daha fazla, yapılan işe oran ile iş parçasına girdi olarak verilen enerjiye daha az olmaktadır.

Yapısal çelik imalatlarında tercih edilen ve yukarıda özet olarak açıklanan bu yöntemlerin ilgili proje için hangisinin veya hangilerinin tercih edileceği projenin detayına, mühendislik ihtiyacına, imalat ve montaj şartlarına ve atmosferik şartlara bağlıdır. Bu hususlar bir bütün olarak değerlendirilip uygun yöntem, uygulamadaki avantaj ve dezavantajları göz önünde bulundurularak tayin edilmelidir.

1.2. Kaynaklanabilirlik

Kaynak kullanılarak yapılan imalat veya birleşimin güvenliği, kalitesi ve ömrü tek başına ne seçilen kaynak yöntemine ne de kaynak metalinin türüne bağlıdır. Bu noktada birçok parametre, yapılan birleşimin kalitesini, emniyetini ve ömrünü belirlemektedir. Ancak

bunların arasında, birleştirilen ana malzemelerin ergime noktasına kadar çıkarılıp nispeten kısa bir sürede soğutulduğu bir ısıl işlem olması sebebi ile sıcaklığın dağılımı ve değişimi ana parametre olarak öne çıkmaktadır.

Bu aralıkta kısa sürede değişen sıcaklık ana metalde iç yapı değişikliklerine neden olduğu gibi bu ortamda bir araya gelen kaynak metali (elektrod), varsa cüruf, ana metal ve atmosfer arasında bazı kimyasal ve metalurjik reaksiyonlar meydana gelir.

Kaynak işlemi sırasında oluşan elektrik arkı sebebi ile kaynak metali ile ana metal eriyerek oluşan eriyik banyosunda (kaynak banyosu) karışırlar. Bu işlem sırasında ana malzemenin kaynak dikişi bölgesine komşu kısımlarında kaynak banyosu eriyik sıcaklığı ile atmosferik sıcaklığı kadar değişen sıcaklıklarda bir geçiş bölgesi oluşur. Bu bölgeye "Isı Tesiri Altındaki Bölge (ITAB) / Heat Affected Zone (HAZ)" ismi verilir.

Kaynak bölgesindeki ısı dağılımı ve ana metal yapısındaki değişimi gösteren karakteristik grafik Şekil 1.1'de gösterilmiştir.

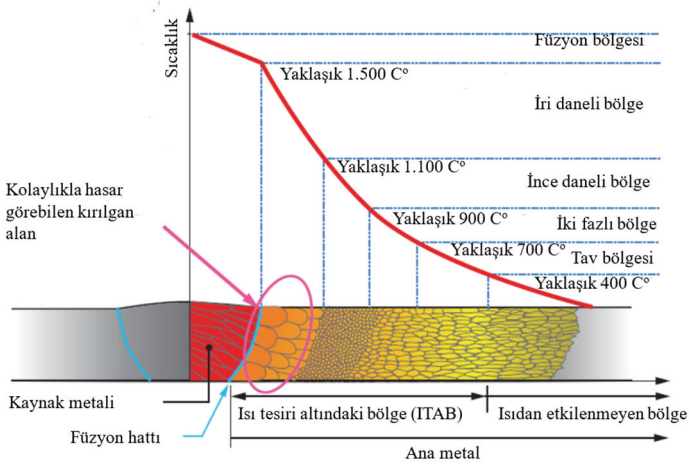

Şekil 1.1 - Ergime ve ısı tesiri altındaki bölge [16].

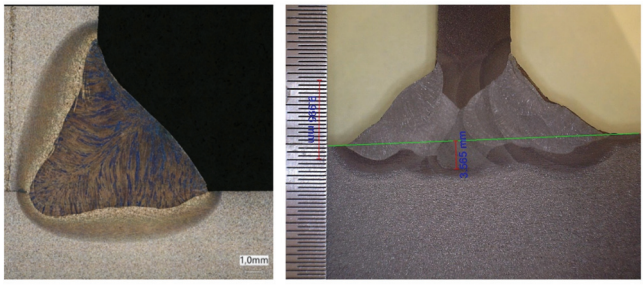

Şekil 1.2 - Tek ve çok pasolu kaynakta ITAB ve ergime bölgesi.

Ergime bölgesi kaynak metali ve ana metalin karışımından oluşur. Tek pasolu kaynak dikişlerinde bu karışım oldukça homojen bir bileşim gösterir. Ancak çok pasolu kaynaklarda her pasonun ana metal ile karışma oranı farklıdır (Şekil 1.2). Hatta belirli et kalınlıklarından sonra iç pasolarda ana metale rastlanmayabilir. Ergime bölgesindeki ana metalin kaynak metaline oranı, uygulanan kaynak yöntemi, paso sayısı ve aktarılan enerjiye göre geniş bir aralık içerisinde değişir.

Kaynak sırasında birçok alaşım elementleri kayba uğrar. Bu kayıpları azaltmak ve kaynak bölgesinin fiziki, kimyasal ve metalurjik yapısını iyileştirmek için bu bölge kaynak anında atmosferik etkilerden korunur.

Sıvı haldeki kaynak banyosu içerisinde atomlar serbest haldedirler. Sıcaklık metal veya alaşımın katılaşma noktasına doğru düştükçe, atomlar kristal kafesleri meydana getirmek üzere birleşmeleri ile çekirdek oluşumu başlar. Soğuma devam ettikçe çekirdekler daneleri oluşturmak üzere yeni atom ve kristal kafesleri ile büyümeye devam eder. Katılaşma anında ortaya çıkan ergime ısısı doğal soğuma ısısını etkileyerek danelerin fazla büyümesini önler. Kaynak sırasında ısının büyük kısmı ergime bölgesinden kondüksiyonla ana metale iletilir. Bu nedenle soğuma yönüne paralel oldukça büyük silindirik daneler oluşur. Kaynak sırasında ısı girdisinin artması, parçanın yüksek sıcaklıkta daha uzun süre tutulması, ön tav uygulanması ergime bölgesinde danelerin irileşmesine neden olur. Tam ters olarak, kaynak bölgesinde soğutma hızının artması dane yapısının incelmesine sebep olur. Bu durum ise gevrek ve kırılgan bir yapı oluşumuna sebep olacağı için arzu edilmez.

ITAB' da ortaya çıkan iç yapısal değişiklikler, ulaşılan sıcaklığın fonksiyonu olarak ana metalin türüne, bileşimine, kalınlığına, ısıl işlem ve üretim sürecine bağlı olarak oldukça çeşitlidir. Ana metal olarak çeliğin içerdiği karbon ve diğer alaşım elementleri kaynak metalinin sertliğini ve sertleşebilme yeteneğini dolayısıyla uygulanması gereken ön tav sıcaklığını etkiler. Sertlik genel bir ifade ile çeliğin içerdiği karbon miktarının bir fonksiyonudur. Sertleşebilme yeteneği ise çeliğin ostenit bölgesinden itibaren ani olarak soğutulması sonucu ortaya çıkan martenzitik yapının oluşma kolaylığının bir ölçüsüdür.

Sertleşebilme yeteneği düşük olan çeliklerin martenzit yapı oluşturabilmeleri için kaynak işlemi sonrasında çok hızlı bir şekilde soğutulmaları gerekir. Sertleşebilme yeteneği yüksek çelikler ise kaynak sonrasında çok yavaş bir şekilde soğutulmaları halinde bile sert martenzitik yapı oluştururlar. Bu açıdan bakıldığında sertleşebilme kabiliyeti, çeliğin kaynak sonrası kaynak bölgesinde göstereceği sertliğin bir bakıma ölçüsüdür.

Sıcaklık değişiminin ve değişim hızının yapı içerisinde sebebiyet verdiği değişikliklere ait daha fazla detay, profesyonel olarak yapı mühendisliği alanı dışında olduğundan bu çalışmada bu noktadan daha ileri bir detay seviyesine girilmeyecektir. "Demir Karbon Denge Diyagramı" içeriği ve detayları için çeşitli referans kaynaklar mevcuttur [19].

Isının tesiri altındaki bölgede yukarıda anlatılan nedenlerle sert ve kırılgan bir yapının ortaya çıkması, yapı içerisinde çatlakların oluşmasına neden olmaktadır. Gevrekleşen kaynak bölgesinde kaynaktan sonra ortaya çıkan iç gerilmelerin, dış yükler altında oluşan gerilmelerin ve kaynak banyosundan yayılan hidrojenin etkilerinin bir araya gelmesi ile kontrolsüz bir şekilde kılcal çatlaklar oluşmakta, statik veya değişken dış yükler sebebi ile bu çatlaklar ani kırılmalara sebep olmaktadır.

Kaynak bölgesindeki sıcaklık dağılımını ve değişimini matematiksel olarak formüle etmek oldukça güç olmakla birlikte Rosenthal ve Rykalin tarafından belirli yakınsamalar ile kabul edilebilir sonuçlar alınmıştır. Ancak uygulamada daha pratik bir yöntem olarak "Karbon Eşdeğeri" yöntemi geliştirilmiştir.

Karbon ve manganez çeliğin sertleşme eğilimini ve çatlak oluşum olasılığını arttırdığından birçok şartnamede yapısal çelik olarak kullanılabilecek çelikler için bu iki elementin miktarları sınırlandırılmıştır.

Karbon eşdeğeri büyüdükçe kaynaktan sonra soğumanın yavaşlatılması gerekmektedir. Bu amaçla parçaya kaynaktan önce ön tavlama uygulanarak soğuma hızı yavaşlatılmaktadır.

Uygulamada en fazla tercih edilen amprik karbon eşdeğer formülleri aşağıda verilmiştir;

Dearden ve Neill formülü

$$C_{eş} = C + \frac{Mn}{6} + \frac{Ni}{15} + \frac{Cr}{5} + \frac{Mo}{4} + \frac{V}{5} \tag{1.1}$$

Kihara, Suzuki Otani ve Tamura formülü

$$C_{eş} = C + \frac{Mn}{6} + \frac{Si}{24} + \frac{Ni}{15} + \frac{Cr}{5} + \frac{Mo}{4} + \frac{Cu}{13} + \frac{P}{2} \tag{1.2}$$

Fransız Ulusal Demiryolu şirketinin kullandığı formül

$$C_{eş} = C + \frac{Mn}{6} + \frac{P}{2} + \frac{Cr}{5} + \frac{Cu}{13} + \frac{Mo}{4} + \frac{Ni}{15} \tag{1.3}$$

Uluslararası Kaynak Enstitüsü'nün kullandığı formül

$$C_{eş} = C + \frac{Mn}{6} + \frac{Cr}{5} + \frac{Mo}{5} + \frac{V}{5} + \frac{Ni}{15} + \frac{Cu}{15} \tag{1.4}$$

Görüleceği gibi yukarıdaki bütün formüllerde karbon ve mangan haricindeki tüm elementlerin katkıları farklı değerlendirilmektedir. Bu da yukarıda bahsedilen karbon ve mangan içeriğinin kısıtlanması konusunu açıklamaktadır.

Isı tesiri altındaki bölge sertliği için Uluslararası Kaynak Enstitüsü'nün tavsiyesi 350 Vickers'i aşmaması yönündedir. Bu amaçla yukarıda açıklandığı üzere soğuma hızı kontrol altında tutulmalı, çok pasolu kaynaklarda pasolar arası sıcaklık kontrol edilmelidir.

Karbon eşdeğerine göre yapı çeliklerinde uygulanacak ön tavlama sıcaklıklarına ait bilgiler literatürde mevcuttur [16].

Çeliklerin kaynaklanabilirliğini etkileyen diğer bir faktör de çelik üretimi sırasında yapılan gaz giderme işlemidir. Bazı üretim usullerinde çelikte segregasyon bölgesinde fosfor (P) ve kükürt (S) toplanır. İngotun haddelenmesi veya dövülmesi bu segregasyon bölgelerini yok etmez ve bunlar profil haddesi sırasında profilin boyun bölgelerinde kalır. Profil enkesitinin kaynaklanması gereken durumlarda boyun bölgelerinde biriken fosfor ve kükürt kaynak banyosuna karışarak gözenek ve çatlak oluşumuna sebep olur. Günümüz imalat şartnamelerinde bu tip enkesit kaynaklarında "Kaynak Erişim Deliği" olarak belirli formlarda kesim yapılıp bu bölgenin uzaklaştırılmasının sebeplerinden biri de budur [16], [17].

2. TEST PLANLAMASI

Söz konusu araştırma kapsamında ulusal ve uluslararası standartlar uyarınca ülkemizde faaliyet gösteren sertifikalı yapısal çelik atölyelerinde, proje şartnamesine, imalatı yapılan detaya ve eleman geometrisine bağlı olarak gazaltı ark kaynağı (GMAW), örtülü elektrod ark kaynağı (SMAW), sürekli ve boy kaynaklarında ise tozaltı ark kaynağı (SAW) olmak üzere üç tip ana kaynak metodu kullanıldığı gözlemlenmiştir.

Bu doğrultuda, iki farklı açıklığa sahip test kirişi ve detaya uygun üç kaynak yöntemi için FEMA350/SAC2000 yükleme protokolü (Şekil 2.1) uygulanacak süneklik testlerine ait 18 adet tam ölçekli numune imalatı planlanmıştır. Numune setinin imalatlarında teste muhatap kiriş alın levhası kaynaklarına ait yöntem detayları aşağıda paylaşılmıştır.

Birinci grup numuneler; GMAW metodu ile TS EN ISO 14341-A ile AWS A5.18 Standartlarına uygun ve sırasıyla G 42 3 C G4Si1/G42 3 M G4 Si1 ve ER70S6 sınıflarında, Akma Dayanımı 470 MPa, Çekme Dayanımı 570 MPa, Çentik Darbe Dayanımı -30 ˚C' de 60 J olan bakır kaplı yüksek manganlı kaynak teli ve koruma gazı olarak da %100 CO_2 kullanılan alın levhalı kaynaklı kirişlerden,

İkinci grup numuneler; SMAW metodu ile TS EN ISO 2560-A ile AWS A5.1 Standartlarına uygun ve sırasıyla E 46 B32 H5, E7018-1 H4 sınıflarında, Akma Dayanımı 480 MPa, Çekme Dayanımı 580 MPa, Çentik Darbe Dayanımı -20˚C' de 180 J, -50 ˚C' de 120 J olan bazik karakterli bir elektrod kullanılan alın levhalı kaynaklı kirişlerden,

Üçüncü grup numuneler ise; GMAW metodu ile TS EN ISO 17632-A ile AWS SFA – 5.20 Standartlarına uygun ve sırasıyla T46 2 P C 1 ve E71T-1C sınıflarında, Akma Dayanımı 500 MPa, Çekme Dayanımı 560 MPa, Çentik Darbe Dayanımı -20 ˚C' de 70 J olan rutil özlü, bakır kaplı kaynak teli ve koruma gazı olarak da %20 CO_2 + %78-79 Argon karışımı kullanılan alın levhalı kaynaklı kirişlerden imal edilmiştir.

2.1. Numune Tasarımı

Kiriş kesiti olarak IPE270 S275JR seçilmiş rijitlik levhasız, dört bulonlu, alın levhalı birleşim detayı referans alınmıştır. Test düzeneği bu doğrultuda tasarlanmış ve boyutlandırılmıştır.

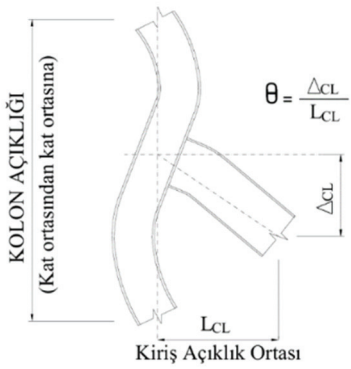

Kat Öteleme Oranı (%)	Tekrar Sayısı
0,375	6
0,500	6
0,750	6
1,000	4
1,500	2
2,000	2
3,000	2
4,000	2
5,000	2
6,000	2

Şekil 2.1 - Dönme açısı ve FEMA350/SAC2000 yükleme protokolü

Süneklik düzeyi yüksek moment aktaran çelik çerçevelerin kolon-kiriş birleşimlerinde yönetmeliğimiz minimum kriter olarak göreli kat ötelemesi açısı için 0.04 Radyan değerini vermektedir (TBDY Md 9.3.4). Dolayısıyla, birleşim detayı içerisinde olan tüm elemanlar bu minimum değeri sağlamak, teyit etmek durumunda olmalıdır.

Çevrim testlerinin uygulanacağı test kirişi için TBDY 2018 Tablo 9B.1' de verilmiş olan uygulama sınırlarının kontrolü aşağıda yapılmıştır.

Plastik mafsalın kolon yüzünden uzaklığı;

$l_h=min(d_b/2, 3b_{bf})$
$l_h=min(270/2, 3x135) l_h=135mm$

Alın levhası kalınlığı;

$t_p=30mm$ $12 \leq t_p \leq 60mm$

Alın levhası genişliği;

$b_p=255mm$ $160 \leq b_p \leq 300$

Bulonlar arasındaki yatay uzaklık;

$g=155mm$ $100 \leq g \leq 155mm$

P_f (P_{fi} ve P_{fo});

$P_{fi}=49.8mm$, $P_{fo}=50mm$ $40 \leq P_f \leq 115mm$

Kiriş enkesit yüksekliği;

$d_b=270mm$ $270 \leq d_b \leq 1400mm$

Kiriş başlık kalınlığı;

$t_{bf}=10.2mm$ $10 \leq t_{bf} \leq 25mm$

Kiriş açıklığı / enkesit yüksekliği oranı;

$L_1=1890/270=7$

$L_2=2580/270=9.56$

Kolon enkesit yüksekliği;

$dc=360mm$ $d_c \leq 920mm$

Bulon sınıfı;

8.8 *(8.8 veya 10.9)*

Bulon öncekme koşulları;

Tam öncekme *(Tam öncekme)*

Alın levhası malzeme sınıfı;

S355JR *(S235, S275 veya S355)*

Başlık levhası kaynağı;

CJP *(Tam penetrasyonlu küt kaynak)*

Yönetmelik uygulama sınırlarına uygunluğu teyit edilen numunenin ön boyutlandırması için IdeaStatica V24 [18] sonlu elemanlar yazılımı kullanılmış, hidrolik veren, LVDT ve Strain Gauge özellik ve kapasiteleri bu doğrultuda seçilmiştir (Şekil 2.2 ve 2.3). İlaveten, sayısal analiz ile elde edilen gerilme ve öteleme değerlerinin deneyden elde edilenler ile uyumlu olduğu gözlemlenmiştir.

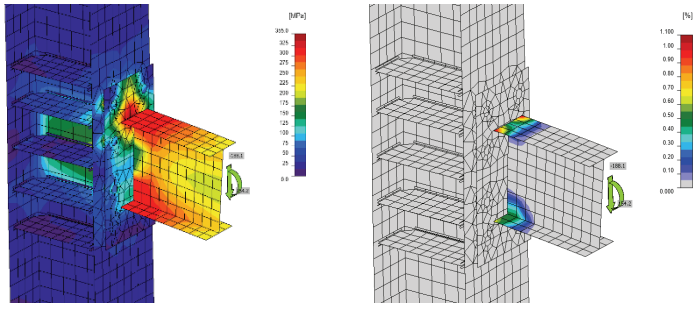

Şekil 2.2 - Kiriş-Kolon Birleşimi sonlu eleman analizleri – Gerilme ve Birim Şekil Değiştirme

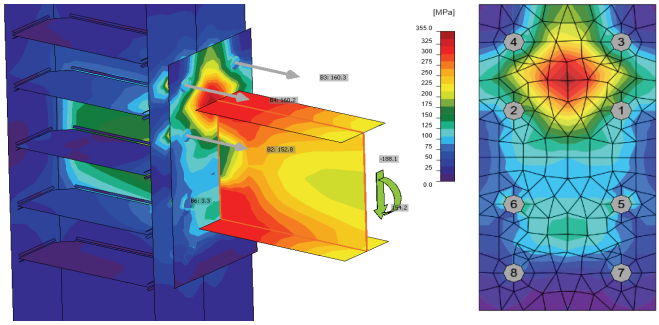

Şekil 2.3 - Bulon kuvvetleri ve alın levhası gerilme dağılımı.

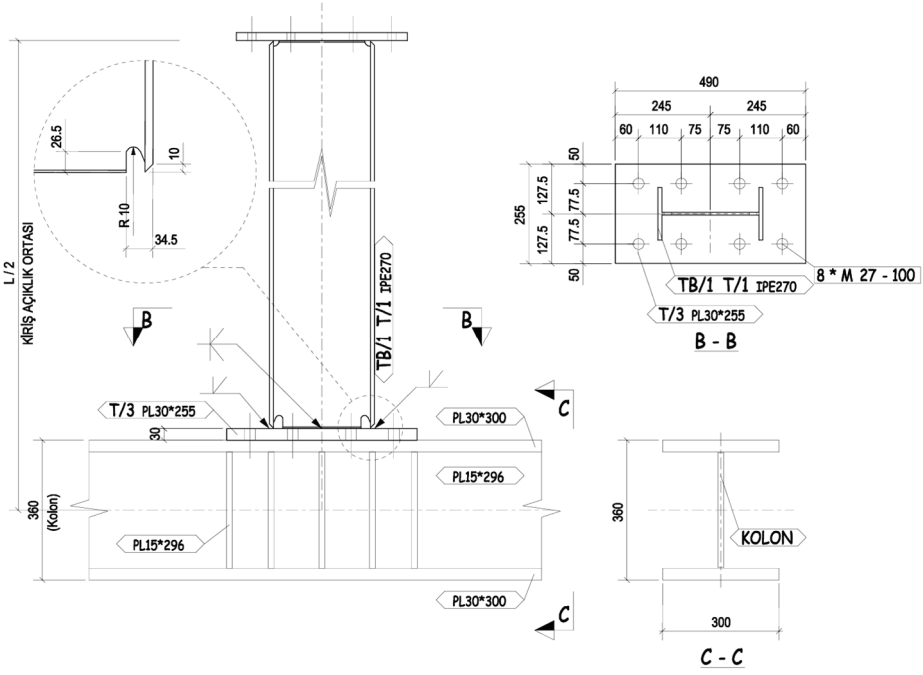

Şekil 2.4 - Test kirişi.

2.2 Numune Üretimi ve Test Düzeneği

Üretilen tüm numuneler için (Şekil 2.4) imalat öncesinde, imalat sırasında ve sonrasında atölye, işçilik ve malzeme sertifikasyonları, çekme, kimyasal kompozisyon, sertlik, kaynak pasoları arası sıcaklık, çatlak kontrol, nüfuziyet ve kaynak hatalarına karşı radyografi testleri içeren kalite kontrol testleri hem imalat atölyesi iç denetimi tarafından hem de bağımsız akredite bir laboratuvar, sertifikalı ekipman ve lisanslı denetimciler aracılığı ile yapılmış, kayda alınmıştır (Şekil 2.5, 2.6, 2.7, 2.8 ve 2.9).

Numuneler, TS ISO 9001:2015 Kalite Yönetim Sistemi, EN ISO 3834-2 Kaynaklı İmalat Yeterlik, EN 1090-2 EXC4 Akreditasyon, TS EN ISO 14001:2015 Çevre Yönetim Sistemi ile TS EN ISO 45001:2018 İSG Yönetim Sistemi belgelerine sahip çelik atölyesinde, onaylı Kaynak Prosedür Şartnamesi (WPS Welding Procedure Specification) ve Kaynak Yöntem Onay (WPQR Weld Procedure Qualification Record) dokümanları doğrultusunda, kalite sertifikaları EN10204 Type 3.1 uyarınca takip edilebilir malzemeler ile TS ISO 9606-1:2014 Kaynakçı Belgelendirme standardı kapsamında sertifikalandırılmış kaynakçılar ile üretilmiş, atölyenin iç denetiminin dışında ISO 9001:2015 Kalite Yönetim Sistemi , TS EN ISO/IEC 17020 ve TS EN ISO/IEC 17025 akreditasyon belgelerine sahip bağımsız bir laboratuvar tarafından denetlenmiştir ve test edilmiştir.

IPE270 kirişlerin alın levhasına kaynaklanacak deneylerimizin odağını oluşturan ucunda flanş ve gövdelerine tam nüfuziyetli küt kaynak teşkili için kaynak ağzı, gövde-flanş birleşimlerine de AWS D1.8'e [17] uygun kaynak erişim delikleri açılmış, çatlak oluşumu ve ilerlemesi için başlangıç sınır durumu oluşturabilecek kılcal çatlak olup olmadığı penetrant test (PT) yöntemi ile test edilmiştir.

Şekil 2.5 - Kaynak erişim delikleri için penetrant test uygulaması.

Şekil 2.6 - Kök paso sonrası temizlik ve pasolar arası sıcaklık ölçümleri.

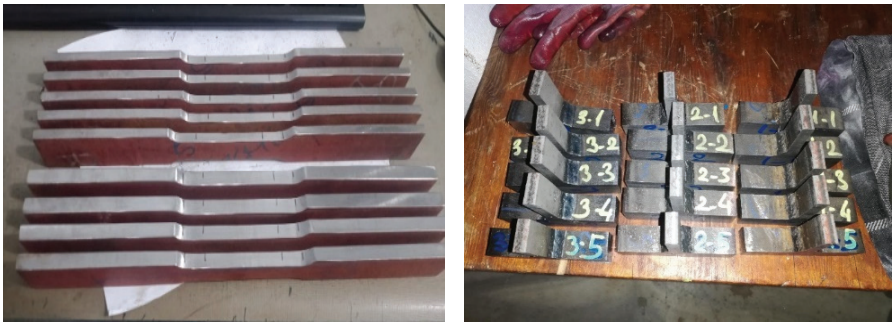

Şekil 2.7 - IPE270 S275JR kiriş gövde ve flanş için çekme numuneleri ile kaynak makro test numuneleri

Test kirişinin gövde ve başlıklarından alınan 9 adet çekme testi numunesinden (Şekil 2.7) elde edilen ortalama değerler Çizelge 2.1' de, her kaynak metodundan hazırlanan 5 set numune (Şekil 2.7) için yapılan Makro testlerin ortalama sonuçları ise Çizelge 2.2'de verilmiştir.

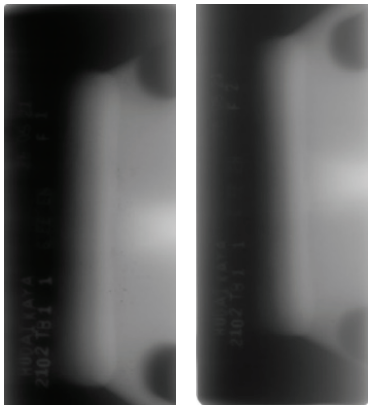

Şekil 2.8 - Tüm numune kaynakları için kaynak sonrası radyografi (RT) ile kalite kontrol.

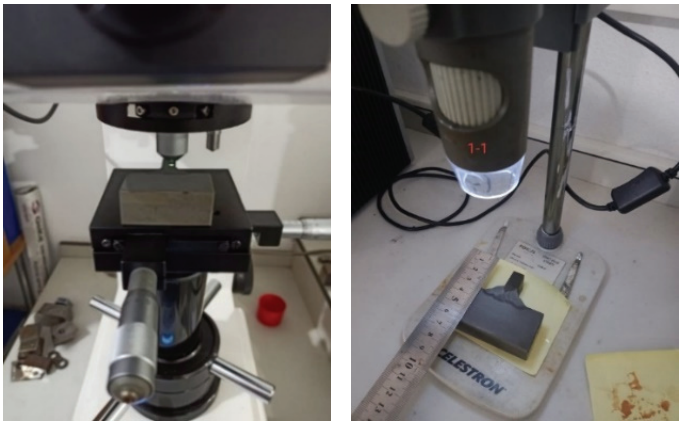

Şekil 2.9 - Kaynak bölgesi Vickers sertlik ve kaynak nüfuziyet ölçümleri.

Çizelge 2.1 - Çekme testi sonuçları

IPE270 S275JR	Rp %0.2 (N/mm^2)	Uzama (%)
Gövde	306.3	29.2
Başlık	306.8	30.2

Çizelge 2.2 - Makro test sonuçları

	Kaynak Sertliği Vickers H10			Kaynak Nüfuziyeti (mm)
	Ana Metal	ITAB	Kaynak	
Grup I	190	228	245	2.05
Grup II	191	223	236	3.47
Grup III	189	235	245	1.69

İmalat ve kalite kontrol testleri tamamlanan numuneler ve deney düzeneği İTÜ İnşaat Fakültesi Yapı ve Deprem Mühendisliği Laboratuvarı' na sevk edilerek hazırlanmış olan imalat ve montaj projeleri (Şekil 2.10) uyarınca kurulumu yapılmıştır.

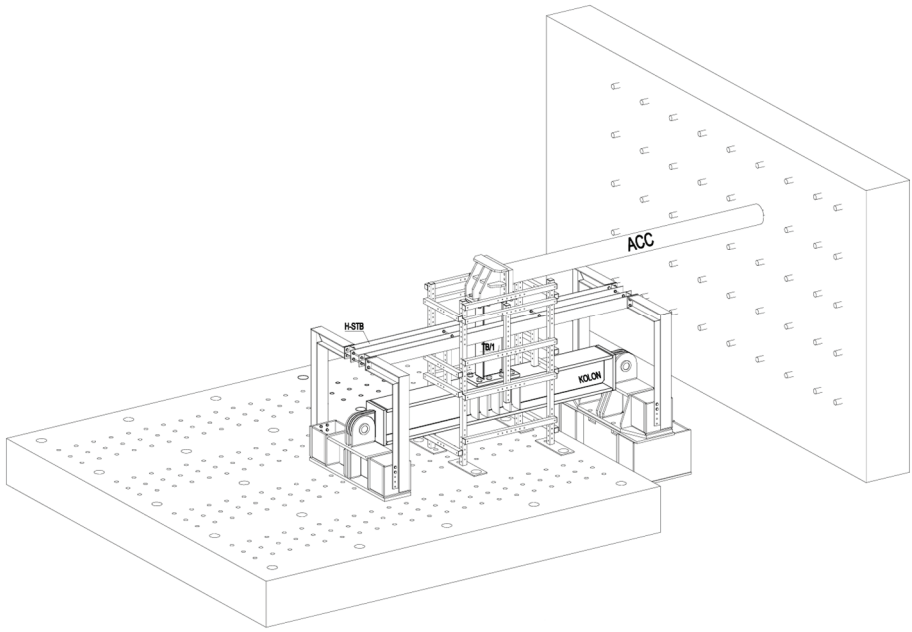

Şekil 2.10 - Test düzeneği

Planlanan testler için kat yüksekliği 3m olan, "I" kesitli kolon ve kirişten teşkil bir moment çerçeve esas alınmış (Şekil 2.4 ve 2.10 ve 2.11), Test kiriş kesiti IPE270 S275JR olarak seçilmiş, alın levhası olarak 30 mm et kalınlığında 255x490mm S355J2+N levha kullanılmıştır.

Kiriş-Kolon bağlantısı için 2x4 adet M27 bulon kullanılmıştır.

Kolon ise yapma "I" kesitinde, 30x300mm S355JR flanş ve 15x296mm S355JR gövde levhasından teşkil edilmiş ve mafsallı olarak mesnetlendirilmiştir.

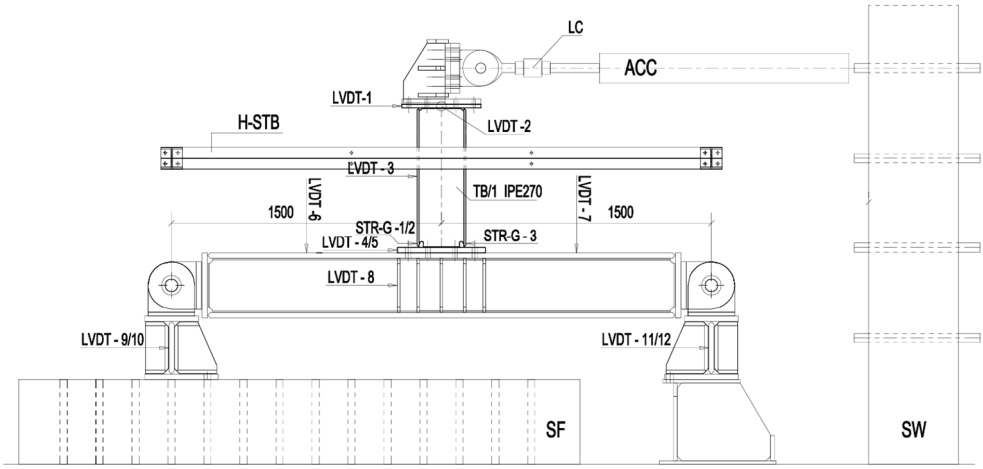

Şekil 2.11 - Test Düzeneği ve veri toplama (enstrümantasyon) noktaları

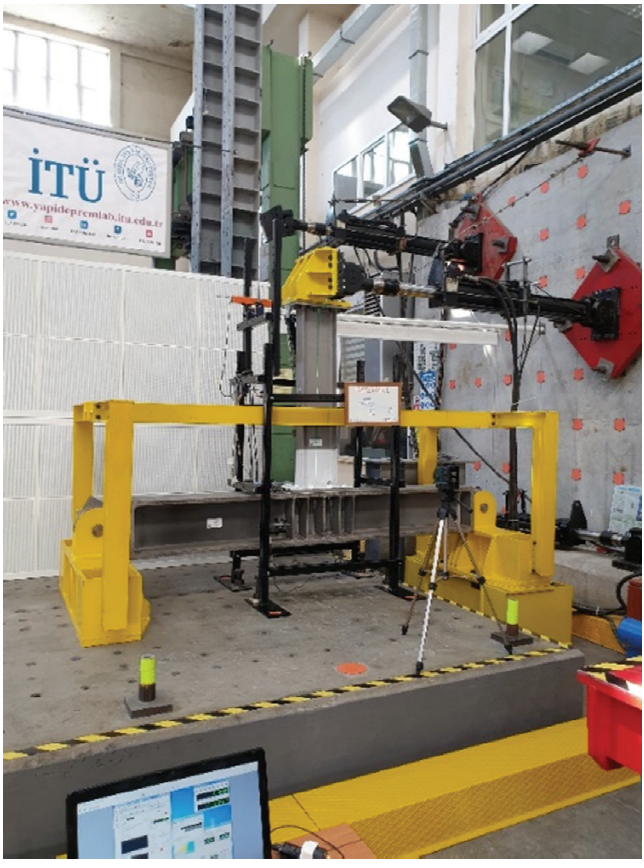

Şekil 2.12 - Genel görünüş

Test için 609.6mm dinamik, 619.8mm statik stroka sahip 250kN yükleme yapabilen MTS marka hidrolik veren (ACC) ve 250kN kapasiteli MTS marka yük hücresi (LC), veri toplama ekipmanı olarak ise kiriş, kolon ve mesnet ötelemeleri için 12 adet deplasman ölçer (LVDT), kiriş-alın levhası kaynaklarındaki gerilme ölçümleri için ise 3 adet gerinim ölçer (Strain Gauge / STR-G) kullanılmıştır (Şekil 2.11).

Düzlem dışı öteleme ve burkulma stabilitesi için test kirişi sürtünmesiz olarak kılavuzlanmıştır (H-STB) (Şekil 2.10 ve 2.11).

Her numune için ortam ve numune sıcaklıkları ölçülmüş, 17-24 °C arasındaki değerlerde testler gerçekleştirilmiştir.

Üretilen numune bilgilerini içeren matris Çizelge 2.3'de verilmiştir. İki tip kiriş numunesinin 1890mm sistem açıklığına sahip ilki (Tip I), TBDY 2018 Tablo 9B.1 doğrultusunda süneklik düzeyi yüksek çerçeve kriteri için verilen minimum kiriş açıklığı/enkesit yüksekliği oranının 7,0 değerine, 2580mm sistem açıklığına sahip ikincisi (Tip II) ise 9,56 değerine karşılık gelmektedir.

Çizelge 2.3 - Numune matrisi.

Grup		FEMA350/SAC2000 Çevrimsel Yüklemeli Süneklik Testleri			
		Tip I		Tip II	
		Etiket No	L_{Sistem} (mm)	Etiket No	L_{Sistem} (mm)
I	GMAW CO_2	TB.1.1	1890	TB.1.7.L	2580
		TB.1.2		TB.1.8.L	
		TB.1.3		TB.1.9.L	
II	SMAW Bazik	TB.1.14	1890	TB.1.17.L	2580
		TB.1.15		TB.1.18.L	
		TB.1.16		TB.1.19.L	
III	GMAW CO_2+Ar	TB.1.24	1890	TB.1.27.L	2580
		TB.1.25		TB.1.28.L	
		TB.1.26		TB.1.29.L	

3. TESTLER

3.1. Birinci grup numune testleri (GMAW + %100CO_2)

3.1.1. Birinci tip numuneler (L=1890mm)

Birinci grup, birinci tip, bir numaralı numune TB.1.1 testi;

Bir nolu testte TB.1.1 numunesinin, 0,03 Radyan dönme açısına karşılık gelen 27nci çevrimde (7. Adım, birinci çevrim) flanş kaynağı çatlamış, toplamda 28 inci çevrimde tamamen kırılmıştır. Flanş ve gövdedeki plastikleşme bölgeleri Şekil 3.3 ve Şekil 3.4'de görülmektedir.

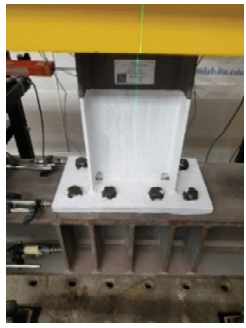

Şekil 3.1 - TB.1.1 Numunesi

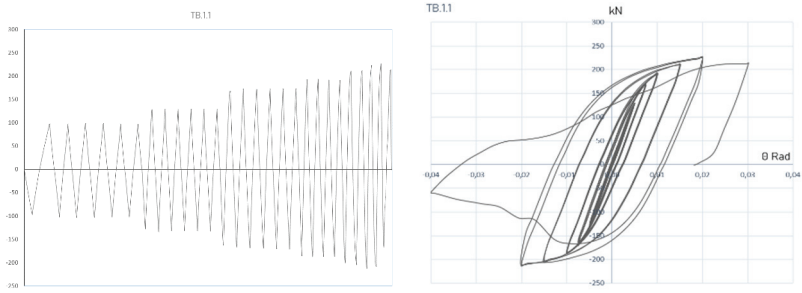

Şekil 3.2 - TB.1.1 Yükleme protokolü ve Kuvvet-Öteleme açısı döngüsü.

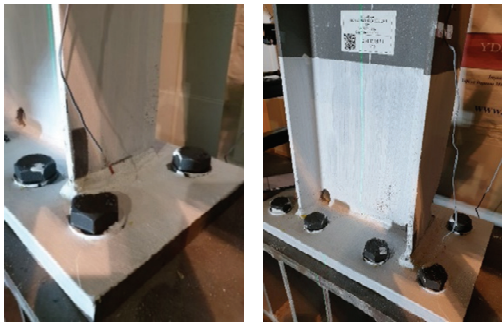

Şekil 3.3 - TB.1.1 çevrim sayısı 27, flanş kaynağında çatlak

Şekil 3.4 - TB.1.1 çevrim sayısı 27, flanş kaynağında kırılma.

Birinci grup, birinci tip, iki numaralı numune TB.1.2 testi;

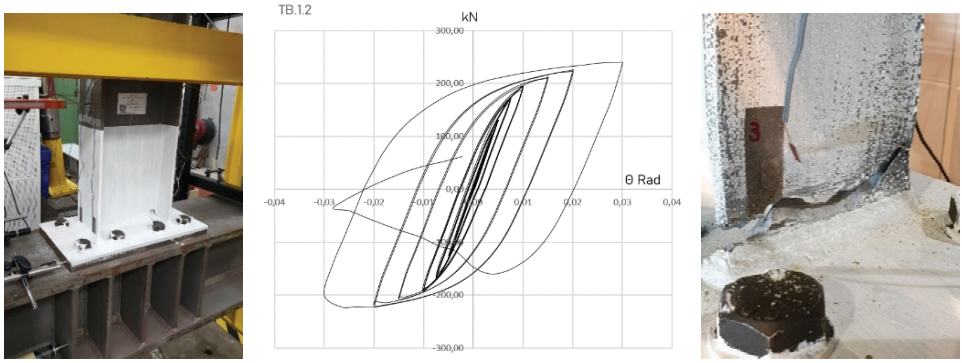

Şekil 3.5 - TB.1.2 Kuvvet-Öteleme Açısı döngüsü ve flanş kaynağında kırılma (Ç. 27)

Birinci grup, birinci tip, üç numaralı numune TB.1.3 testi;

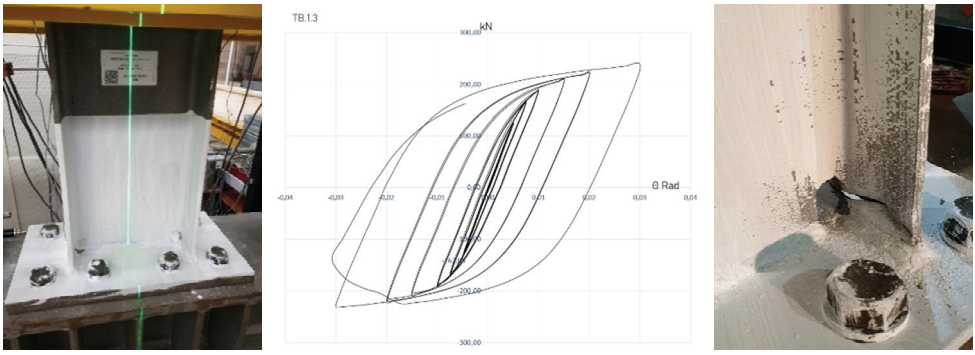

Şekil 3.6 - TB.1.3 Kuvvet-Öteleme Açısı döngüsü ve flanş kaynağında kırılma (Ç.27)

3.1.2. İkinci tip numuneler (L=2580mm)

Birinci grup, ikinci tip, bir numaralı numune TB.1.7.L testi;

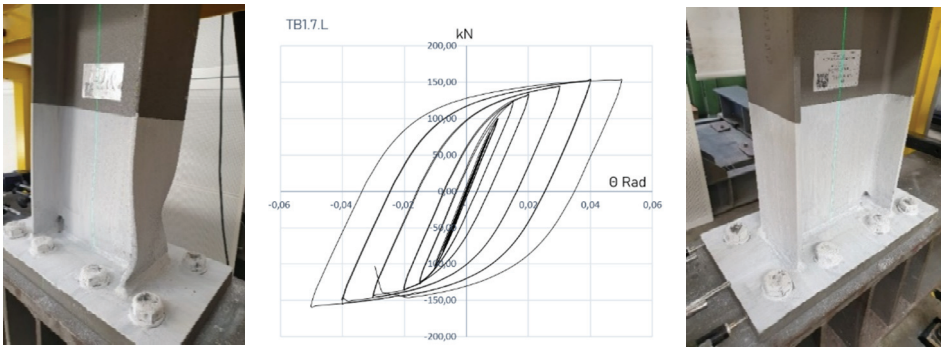

Şekil 3.7 - TB.1.7.L Kuvvet-Öteleme Açısı döngüsü ve flanş kaynağında kırılma (Ç.32).

Birinci grup, ikinci tip, iki numaralı numune TB.1.8.L testi;

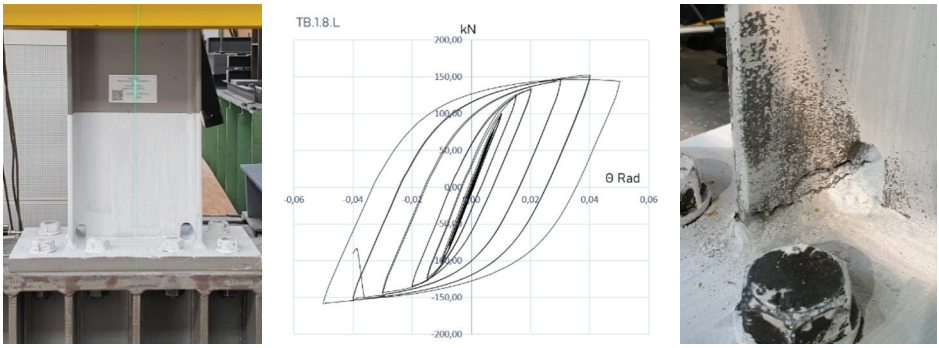

Şekil 3.8 - TB.1.8.L Kuvvet-Öteleme Açısı döngüsü ve flanş kaynağında kırılma (Ç.31).

Birinci grup, ikinci tip, üç numaralı numune TB.1.9.L testi;

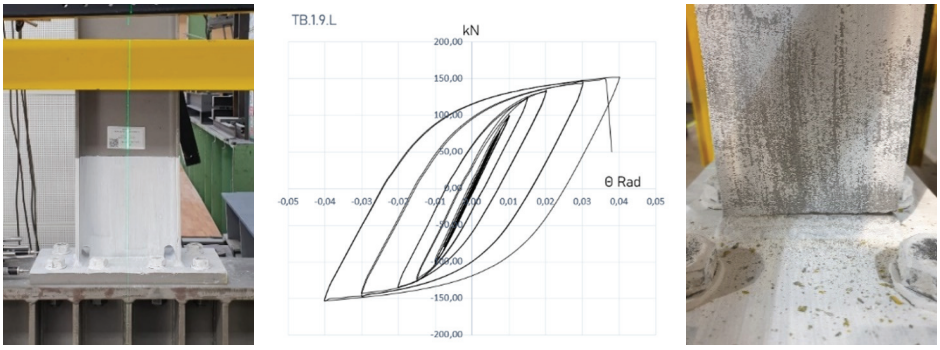

Şekil 3.9 - TB.1.9.L Kuvvet-Öteleme Açısı döngüsü ve flanş kaynağında kırılma (Ç.30).

3.2. İkinci grup numune testleri (SMAW + Bazik)

3.2.1 Birinci tip numuneler

İkinci grup, birinci tip, bir numaralı numune TB.1.14 testi;

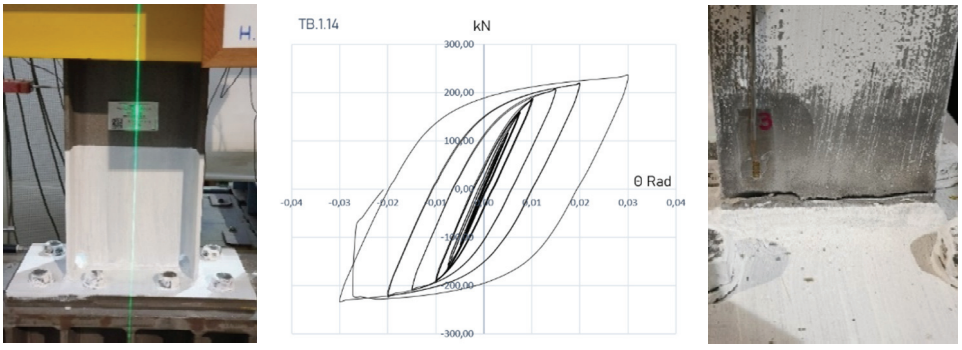

Şekil 3.10 - TB.1.14 Kuvvet-Öteleme Açısı döngüsü ve flanş kesitinde kırılma (Ç.28).

İkinci grup, birinci tip, iki numaralı numune TB.1.15 testi;

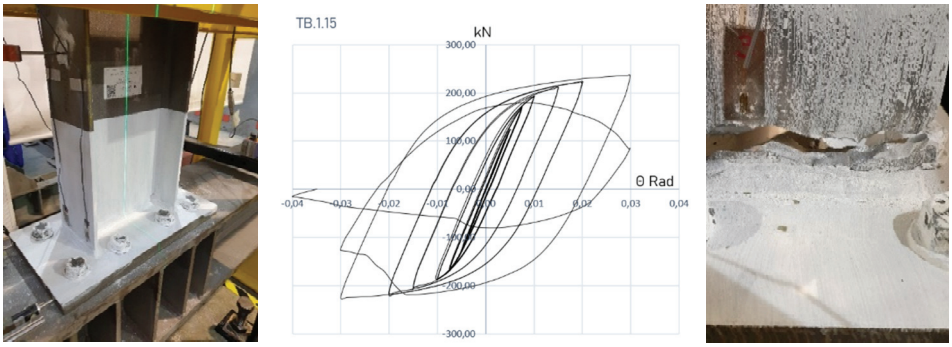

Şekil 3.11 - TB.1.15 Kuvvet-Öteleme Açısı döngüsü ve flanş kesitinde kırılma (Ç.28).

İkinci grup, birinci tip, üç numaralı numune TB.1.16 testi;

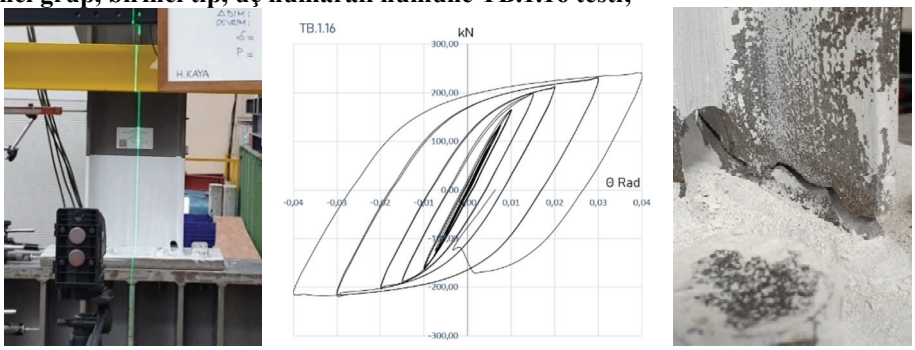

Şekil 3.12 - TB.1.16 Kuvvet-Öteleme Açısı döngüsü ve flanş kesitinde kırılma (Ç.30).

3.2.2. İkinci tip numuneler

İkinci grup, ikinci tip, bir numaralı numune TB.1.17.L testi;

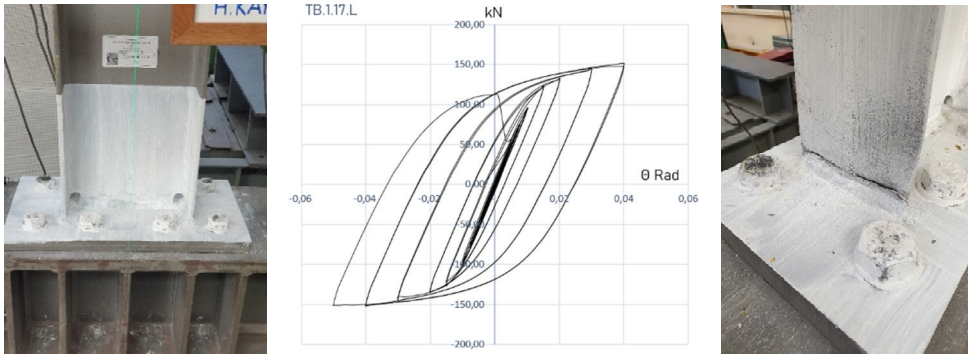

Şekil 3.13 - TB.1.17.L Kuvvet-Öteleme Açısı döngüsü ve flanş kesitinde kırılma (Ç.31).

İkinci grup, ikinci tip, iki numaralı numune TB.1.18.L testi;

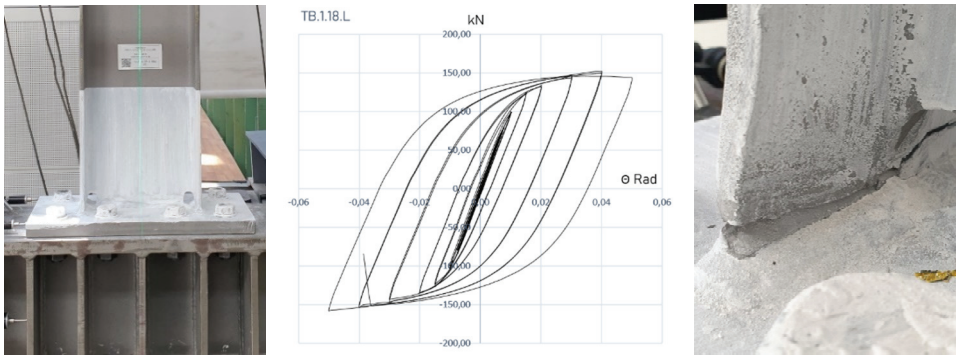

Şekil 3.14 - TB.1.18.L Kuvvet-Öteleme Açısı döngüsü ve flanş kesitinde kırılma (Ç.32).

İkinci grup, ikinci tip, üç numaralı numune TB.1.19.L testi;

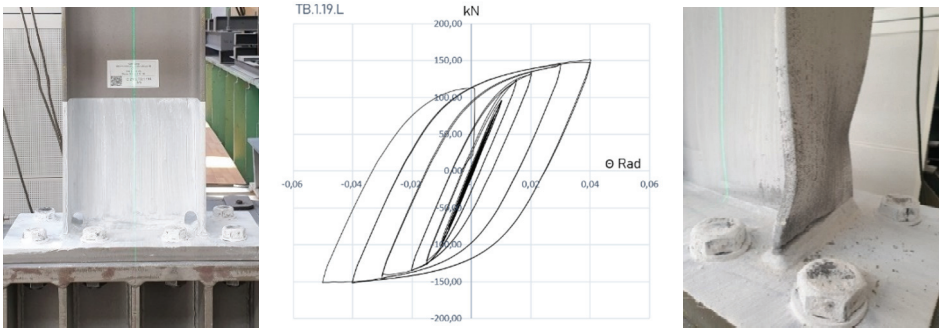

Şekil 3.15 - TB.1.19.L Kuvvet-Öteleme Açısı döngüsü ve flanş kesitinde kırılma (Ç.31).

3.3. Üçüncü grup numune testleri (GMAW +%20 CO_2 + %78-79 Ar)

3.3.1. Birinci tip numuneler

Üçüncü grup, birinci tip, bir numaralı numune TB.1.24 testi;

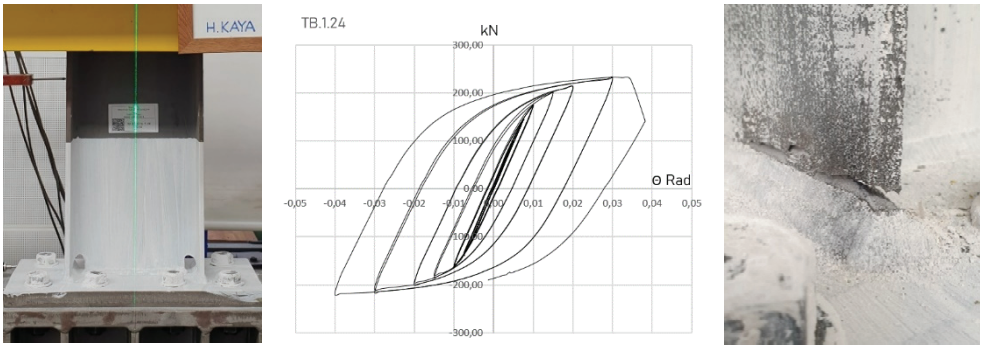

Şekil 3.16 - TB.1.24 Kuvvet-Öteleme Açısı döngüsü ve flanş kaynağında kırılma (Ç.29).

Üçüncü grup, birinci tip, iki numaralı numune TB.1.25 testi;

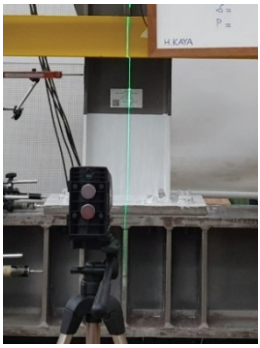

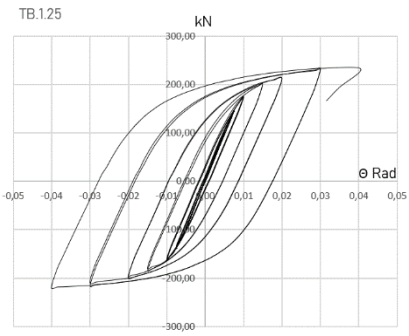

Şekil 3.17 - TB.1.25 Kuvvet-Öteleme Açısı döngüsü ve flanş kaynağında kırılma (Ç.29).

Üçüncü grup, birinci tip, üç numaralı numune TB.1.26 testi;

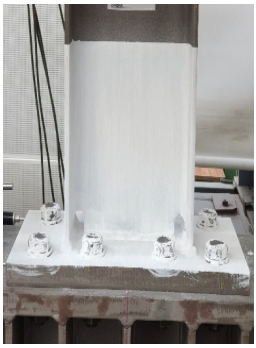

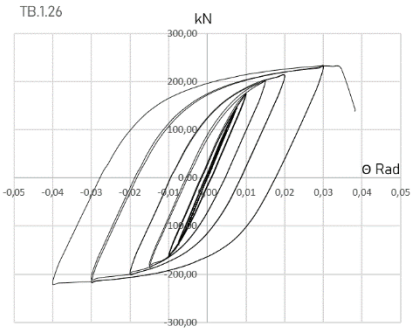

Şekil 3.18 - TB.1.26 Kuvvet-Öteleme Açısı döngüsü ve flanş kaynağında kırılma (Ç.29).

3.3.2. İkinci tip numuneler

Üçüncü grup, ikinci tip, bir numaralı numune TB.1.27.L testi;

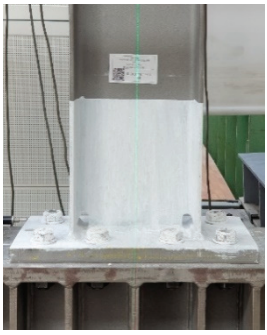

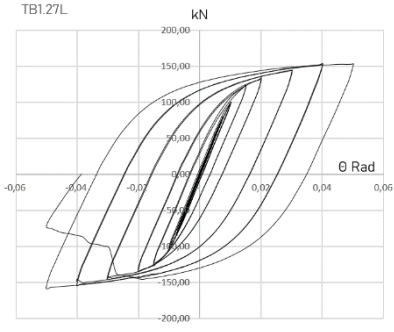

Şekil 3.19 - TB.1.27.L Kuvvet-Öteleme Açısı döngüsü ve flanş kaynağında kırılma (Ç.32).

Üçüncü grup, ikinci tip, iki numaralı numune TB.1.28.L testi;

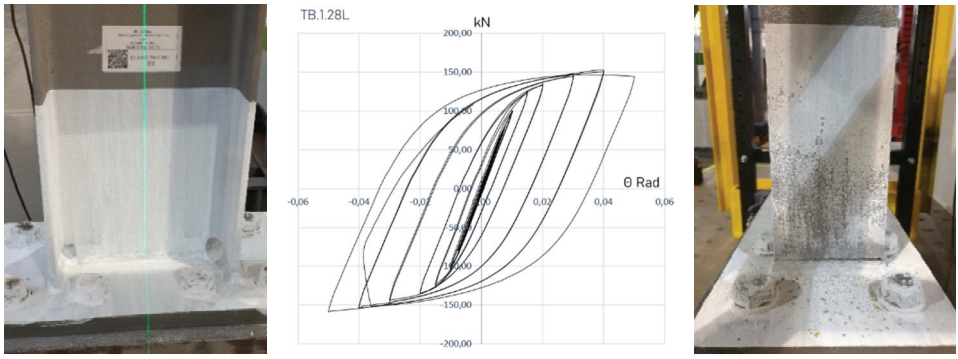

Şekil 3.20 - TB.1.28.L Kuvvet-Öteleme Açısı döngüsü ve flanş kaynağında kırılma (Ç.32).

Üçüncü grup, ikinci tip, üç numaralı numune TB.1.29.L testi;

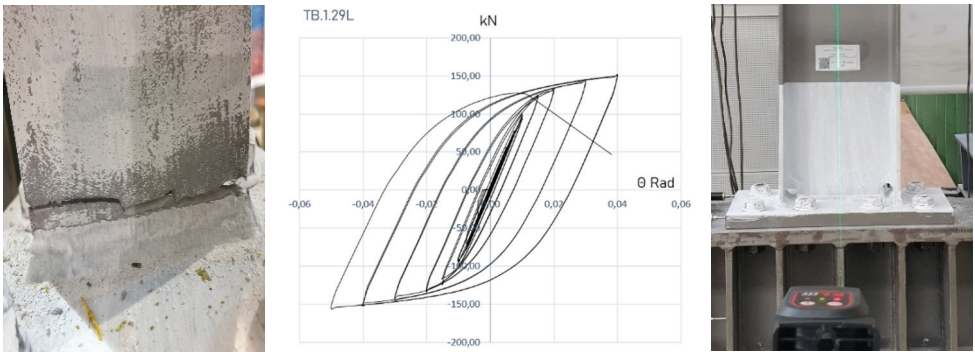

Şekil 3.21 - TB.1.29.L Kuvvet-Öteleme Açısı döngüsü ve flanş kaynağında kırılma (Ç.31).

Çizelge 3.1 - Birinci tip numuneler için çevrimsel yüklemeli süneklik testleri özeti.

Grup/Tip No	Etiket No	L_{sistem} (mm)	t (ºC)	Kırılma anındaki çevrim sayısı	Teyit edilen göreli kat ötelemesi (Radyan)	Kırılma yeri
I / 1	TB.1.1	1890	17	27	0,02	Füzyon hattı
	TB.1.2		15	27	0,02	Füzyon hattı
	TB.1.3		15	27	0,02	Füzyon hattı
II / 1	TB.1.14	1890	18	28	0,02	Kiriş
	TB.1.15		19	28	0,02	Kiriş
	TB.1.16		19	30	0,03	Kiriş
III / 1	TB.1.24	1890	21	29	0,03	Füzyon hattı
	TB.1.25		20	29	0,03	Füzyon hattı
	TB.1.26		21	29	0,03	Füzyon hattı

Çizelge 3.2 - İkinci tip numuneler için çevrimsel yüklemeli süneklik testleri özeti.

Grup/Tip No	Etiket No	L_{sistem} (mm)	t (°C)	Kırılma anındaki çevrim sayısı	Teyit edilen göreli kat ötelemesi (Radyan)	Kırılma yeri
I / 2	TB.1.7.L	2580	21	32	0,04	Füzyon hattı
	TB.1.8.L		21	31	0,04	Füzyon hattı
	TB.1.9.L		22	30	0,03	Füzyon hattı
II / 2	TB.1.17.L	2580	22	31	0,04	Kiriş
	TB.1.18.L		21	32	0,04	Kiriş
	TB.1.19.L		22	31	0,04	Kiriş
III / 2	TB.1.27.L	2580	23	32	0,04	Füzyon hattı
	TB.1.28.L		24	32	0,04	Füzyon hattı
	TB.1.29.L		24	31	0,04	Füzyon hattı

4. ELDE EDİLEN SONUÇLAR

Deprem etkileri altında büyük plastik şekil değiştirmelere maruz kalabilecek yapılar için süneklik kapasitesi toptan göçme mekanizmasının önünde en büyük güvence olarak günümüz yönetmeliklerinde yer almaktadır. Elbette bu şartları sağlayabilmek için mühendislik tasarımın başında "yüksek sünek" veya "normal sünek" kabullerinin ötesine geçip yapının tasarlandığı matematik modele uygun davranabileceği detayları seçmek, bu detayların bir bütün olarak yapı davranışına etkilerini bilmek, üretim ve montajları sırasında çıkabilecek mahsurları öngörmek mühendislik temel prensipleri itibariyle önemlidir.

Betonarme yapılara kıyasla malzeme katsayılarının daha düşük olması, modelleme, analiz, tasarım, imalat ve montaj hatalarını daha az tolore edebilme yeteneğine sahip olmaları sebebi ile odak konumuz olan çelik yapılar, doğal olarak tasarım, üretim ve montaj dönemlerindeki hatalara karşı daha hassastırlar.

Günümüzde üretim hızının yüksek, detaylarının nisbeten daha basit ve işçilik maliyetlerinin düşük olması gibi sebeplerle tercih edilen kaynağı bir birleşim aracı olarak bulon ve perçinden ayıran önemli yapısal farklılıklar bulunmaktadır. Öncesinin, kaynaklama anının ve sonrasının birer ısıl işlem olmaları sebebi ile ana malzeme kalınlığına. karbon eşdeğerine ve uygulanan metoda bağlı olarak metalürjik mikro yapıda değişiklikler oluşur. Birleşim detayında tasarım sırasında öngörüleyen artık gerilmelere sebep olabilir. Yapı değişikliği sebebi ile füzyon ve ısı tesiri altındaki bölgeler kırılma hassasiyetine sahip alanlardır.

Uygulama öncesinde, sırasında ve sonrasında gösterilmesi gereken özen ve alınması gereken tedbirler her kaynak metoduna göre farklılık gösterir. Kaynak malzemesi ve yönteminin seçimi atölye, şantiye ve atmosferik şartlar ile proje ve detayına özel olarak yapılır. Tüm bu parametre ve usüllerin seçimi, yöntemlerin belirlenmesi mühendislik hizmeti altındaki yapılar için atölye inisiyatifine bırakılmayacak kadar önemlidir.

Bu çalışmanın amacı, yönetmelik maddesi üzerinde araştırma yapmak değildir. Birinci bölümde de açıklandığı gibi ülkemiz yapısal çelik atölyelerinde tercihen kullanılan kaynak yöntemlerinin yönetmeliğimiz kapsamında performanslarını incelemektir.

Bu amaçla, yönetmelik asgari şartlarını referans alarak test düzeneği oluşturmak, aynı zamanda çalışma sonucunda elde edilecek bilgiler için kıyas veya referans düzlemi oluşturmak açısından anlam teşkil etmektedir.

Ancak, doğal olarak bu referansla üretilen test numunelerinden elde edilen sonuçlar, yönetmelik maddelerinin ülkemiz üretim şartları doğrultusunda irdelenmesi için öncü veriler oluşturmuş ve her ne kadar doğrudan amaç olmasa da dolaylı olarak yönetmelik ilgili madde ve şartları üzerinde yorum yapma imkanı ortaya çıkmıştır.

Bu araştırma için 18 Mart 2018 yılı 30364(Mükerrer) sayılı Resmi Gazete'de yayımlanarak 1 Ocak 2019 yılında yürürlüğe giren 2018 yılı Türkiye Bina Deprem Yönetmeliği, Moment Aktaran Çelik Çerçevelerde Kiriş-Kolon Birleşim Detayları Ek9B Bölümü, Md.9B.2 "Tam Dayanımlı Bulonlu Alın levhalı Birleşimler" alt bölümünde yer alan "Rijitlik Levhasız, 4 Bulonlu, Alın Levhalı Birleşim" referans alınmıştır.

Bu birleşim detayının test numunesi olarak seçilmesinin iki nedeni bulunmaktadır. Birincisi, kiriş ile alın levhası birleşiminde herhangi bir berkitme veya rijitlik levhası bulunmamaktadır. İkincisi ise ana kiriş enkesitinde Md. 9B.5 gibi bir zayıflatma ön görülmemiştir. Bu nedenle birleşim kaynağının performansının tam olarak gözlemlenebileceği öngörülmüştür.

Araştırma kapsamında gerçekleştirilen tam ölçekli deneylerde aşağıdaki bilgilere ulaşılmıştır;

1. Süneklik düzeyi yüksek çerçeveler için minimum 7 olarak alt limiti verilen kiriş açıklığı/enkesit yüksekliği oranına ait Tip I numunelerinde göreli kat ötelemesi değeri I. Grup numuneler için 0,02 Radyan, II. Grup numuneler için 0,02 ve 0,03 Radyan, III. Grup numuneler için 0,03 Radyan olarak gerçekleşmiştir. Kırılmalar I ve III. Grup kaynaklar için kaynak füzyon bölgesinde, II. Grup kaynak için kiriş flanşı enkesitinde meydana gelmiştir (Çizelge 3.1).

   Elde edilen göreli kat ötelemesine ait değerler, 0,04 Radyan olan yönetmelik minimum koşulunun altında kalmıştır.

2. Kiriş açıklığı/enkesit yüksekliği oranının 9,56 olarak tayin edildiği II. Tip numunelerinde göreli kat ötelemesi değeri I. Grup numunelerin biri 0,03 Radyan diğer ikisi 0,04 Radyan, II. Grup numuneler için 0,04 Radyan, III. Grup numuneler için 0,04 Radyan olarak gerçekleşmiştir. Kırılmalar I ve III. Grup kaynaklar için kaynak füzyon bölgesinde, II. Grup kaynak için kiriş flanşı enkesitinde meydana gelmiştir (Çizelge 3.2).

   I.Grup kaynak yöntemi için kararsız bir davranışın devam ettiği, II ve III. Grup kaynak yöntemleri için ise yönetmelik asgari şartlarını sağladıkları söylenebilir. Ancak I ve III. Grup kaynak yöntemleri ile üretilen numunelerdeki kırılmaların halen kaynak füzyon bölgesinde olduğu da ayrıca dikkat edilmesi gereken bir husus olarak tespit edilmiştir.

3. TBDY 2018 Madde 9 Tablo 9.1' de deprem yükleri etkisindeki elemanların birleşim ve eklerinde kullanılacak kaynak metali özellikleri ile ilgili olarak talep edilen minimum değerler ile bu araştırma kapsamında kullanılan kaynak metallerinin özellikleri Çizelge 4.1'de verilmiştir.

Çizelge 4.1 - Kaynak metalleri karşılaştırması.

	TBDY 2018		Araştırma kapsamındaki kaynak metalleri		
			I Grup	II Grup	III Grup
Kaynak metali sınıfı	E480	E550	G 42 3 C G4Si1 G 42 3 M G4Si1	E 46 B32 H5	T 46 2 P C 1
Karakteristik akma gerilmesi (N/mm^2)	400	470	470	480	500
Min. Çekme dayanımı (N/mm^2)	480	550	570	580	560
Min. Uzama (%)	22	19	25	30	25
Çentik tokluğu (CVN)	-18 ºC min. 27J		-30 ºC 60J	-20 ºC 180J	-20 ºC 70J

Görüleceği üzere araştırma kapsamında seçilen tüm metotlarda kullanılan kaynak metallerine ait özellikler, yönetmelik asgarisi üzerindedir.

Buradan hareketle, test sonuçlarından elde edilen veriler doğrultusunda, yönetmelik kapsamında yapılan asgari tarifin gerekli ancak tek başına yeterli olmadığı ifade edilebilir.

5. ÖNERİLER

Bu araştırma kapsamındaki testlerden elde edilen veriler incelendiğinde, özellikle sismik ve dinamik etkiler altındaki elemanlar, birleşimler veya taşıyıcı sistemler ile süneklik düzeyi yüksek çerçeveler için aşağıda verilen maddeler öne çıkmaktadır;

1. Bu tip sistemlerde derin nüfuziyetli, tam penetrasyonlu, çentik darbe tokluğu yüksek kaynak metali seçimi, olası kırılmanın kaynak yerine malzemede oluşması açısından alınması gereken bir tedbir olarak karşımıza çıkmaktadır.
2. Tasarımda, imalatta ve montajda çentik etkisi oluşturabilecek zorlanmış detaylardan ve süreksizliklerden kaçınılmalıdır.
3. Altlık veya kök plakası kullanılacak ise çentik etkisi yapabilecek metal kök plakası yerine seramik plaka tercih edilmeli, kaynak başlangıç ve bitişlerindeki krater bölgelerinin çentik etkisine sebep olacağı hususu dikkatten kaçırılmamalıdır.
4. TBDY 2018 asgari şart tanımları gerek kaynak metali gerekse de bu tip birleşimlerin uygulama sınırları açısından genişletilmeli ve ilave koşullar ile desteklenmelidir.

   Bu amaçla gerçek boyutlu numuneler üzerinde yapılacak test sayı ve tipleri artırılmalıdır.
5. Et kalınlığı yüksek levha ve profiller için düzlemine dik kuvvetler altında oluşabilecek laminer yırtılma ile ilgili kısıtlar ve kontrol mekanizmaları yönetmelik kapsamına dahil edilmelidir.

6. Kaynak bölgesine enerji girişini optimize edebilmek, artık gerilme riskini düşürmek ve birleşim bölgesinde yapısal değişimi risk oluşturmayacak seviyelerde tutabilmek açısından kaynak öncesi, kaynak sırası ve kaynak sonrası tüm işlemler ile bunların sonuçları konusunda asgari bilgi sahibi olmak ve ana metal ile kaynak metali ve yönteminin seçimi konusunda tasarımcı olarak inisiyatif alınması önem teşkil etmektedir.

   Bu amaçla, tasarımda, imalat ve montajda profesyonel olarak hizmet veren inşaat mühendisi meslektaşlarımızın, bir birleşim elemanı olarak kaynağa yaklaşımı konusunda farkındalığın artırılması önem kazanmaktadır.

Semboller

b_p : Alın levhası genişliği

$C_{eş}$: Karbon eşdeğeri

d_b : Kiriş enkesit yüksekliği

d_c : Kolon enkesit yüksekliği

E : Elastisite modülü

g : Bulonlar arası yatay uzaklık

K : Gerilme yoğunluk faktörü

l_h : Plastik mafsalın kolon yüzünden uzaklığı

M : Moment

M_p : Plastik moment

N : Tekrar sayısı

P_{fi}, P_{fo} : Kiriş flanşına bulon mesafesi

R : Dönme kapasitesi

t_{bf} : Kiriş başlık kalınlığı

t_p : Alın levhası kalınlığı

Θ_p : Plastik dönme açısı

σ : Normal gerilme

τ : Kayma gerilmesi

Kaynaklar

[1] Gross, J.L., (1998), Design Guidelines For The Seismic Modification Of Welded Steel Moment Buildings, NIST Sp 931.

[2] TBDY (2018), Türkiye Bina Deprem Yönetmeliği, Afet ve Acil Durum Yönetimi Başkanlığı, Ankara, Türkiye

[3] Changshi M., Fisher J., (2001), Effect of Local Details on Ductility of Welded Moment Connections, Journal of Structural Engineering, Vol 127, Issue 9, https://doi.org/10.1061/(ASCE)0733-9445(2001)127:9(1036)

[4] Chen Y., Huo J., Zhou X., Chen W., (2023), Dynamic Behaviors of Butt Welds and Fillet Welds Under Intermediate Strain Rate, Journal of Constructional Steel Research, Vol 201 https://doi.org/10.1016/j.jcsr.2022.107683

[5] Chen Y., Huo J., Zhou X., Chen W., (2021), Dynamic Tensile Behaviors of Welded Steel Joint Material, Journal of Constructional Steel Research, Vol 183, https://doi.org/10.1016/j.jcsr.2021.106700

[6] Chen C., Lee J., Lin M., (2003), Behavior of Steel Moment Connections with a Single Flange Rib, Engineering Structures, Vol 25, Issue 11, https://doi.org/10.1016/S0141-0296(03)00104-4

[7] Dexter R., Melendrez M., (2000), Through-Thickness Properties of Column Flanges in Welded Moment Connections, Journal of Structural Engineering, Vol 126, DOI:10.1061/(ASCE)0733-9445(2000)126:1(24)

[8] Dubina D., Stratan A., (2002), Behavior of Welded Connections of Moment Resisting Frames Beam to Column Joints, Engineering Structures, Vol 24, Issue 11, https://doi.org/10.1016/S0141-0296(02)00091-3

[9] Haghollahi A., Ahmadi H., (2018), Cyclic Behaviour of Steel Beam to Column Moment Connections Using Different Sizes of Flange Plates and Reinforced by a Single Rib Plate, Civil Engineering Journal, Vol 4, DOI:10.28991/cej-030975

[10] Lu L., Ricles J., Mao C., Fisher J., (2000), Critical Issues in Achieving Ductile Behaviour of Welded Moment Connections, Journal of Constructional Steel Research, Vol 55, DOI:10.1016/S0143-974X(99)00092-9

[11] Nakashima M., Roeder C., Maruoka Y., (2000), Steel Moment Frames for Earthquakes in Unites States and Japan, Journal of Structural Engineering, Vol 126, Issue 8, https://doi.org/10.1061/(ASCE)0733-9445(2000)126:8(861)

[12] Ricles J., Mao C., Lu L., Fisher J., (2003), Ductile Details for Welded Unreinforced Moment Connections Subject to Inelastic Cyclic Loading, Engineering Structures, Vol 25, Issue 6, DOI:10.1016/S0141-0296(02)00176-1

[13] Ricles J., Fisher J., (2002), Development and Evaluation of Improved Details for Ductile Welded Unreinforced Flange Connections, SAC/BD-00/24

[14] EN1090-2 (2018), Execution of Steel Structures and Aluminium Structures Technical Requirements for Steel Structures, European Committee for Standardization; Brussels, Belgium.

[15] FEMA 350 (2000), Recommended Seismic Design Criteria for New Steel Moment Frame Buildings, Washington DC, USA

[16] Tülbentçi, K. (1990), MIG-MAG Eriyen Elektrod ile Gazaltı Kaynağı, Gedik Holding, Istanbul, Turkiye

[17] AWS D.1.8/D1.8M (2016), Structural Welding Code-Seismic Supplement, American Welding Society, MA, USA

[18] IdeaStatiCa V24 (2024) Sonlu Elemanlar Yazılımı, Çek Cumhuriyeti

Turkish Journal of Civil Engineering, 2025, 81-95, Paper 800, ***Research Article***

Modelling of Steady-State Seepage of an Embankment Dam Using Teaching-Learning Based Optimization Algorithm

Arife GUNAY[1*]
Sami Oguzhan AKBAS[2]

ABSTRACT

The goal of the this study is to investigate the applicability of the teaching-learning based optimization (TLBO) algorithm for modeling seepage in embankment dams. The input parameters selected for the models to be built are the values of permeability (k_s), van Genuchten's suitability parameters α and n, whose effect on seepage has been investigated over the years due to their uncertainties. The validity of the TLBO was compared with that of conventional regression analysis (CRA) methods. Both methods were utilized with different regression forms. The parameters chosen as input are modeled as random variables with a log-normal distribution, and total discharge (Q) was obtained. Four statistical indices, that is, root mean square error, mean absolute error, average relative error and coefficient of determination, were used to evaluate the performance of the models. The equations obtained using TLBO algorithms can predict the total discharge in embankment dams better than CRA. In addition, the reliability of TLBO has been demonstrated by conducting analyses using the outputs of CRA as a benchmark.

Keywords: Monte Carlo Simulation, permeability, van genuchten parameters, seepage analysis, teaching-learning based optimization.

1. INTRODUCTION

The continuous and unimpeded movement of water from upstream to downstream of a dam is defined as seepage. The design of embankment dams aims to keep this movement within acceptable limits. In line with this objective, zoned embankment dams are designed using soils with low permeability (k) in the core section. However, the inevitable variability in the

Note:
- This paper was received on April 1, 2024 and accepted for publication by the Editorial Board on October 16, 2024.
- Discussions on this paper will be accepted by May 31, 2025.
- https://doi.org/10.18400/tjce.1462869

1 Karadeniz Technical University, Department of Civil Engineering, Trabzon, Türkiye
arifegunay@ktu.edu.tr - https://orcid.org/0000-0002-3116-0408

2 Gazi University, Department of Civil Engineering, Ankara, Türkiye
soakbas@gazi.edu.tr - https://orcid.org/0000-0002-7872-1604

* Corresponding author

soil properties leads to uncertainties in performance [1,2]. These uncertainties mean that deterministic seepage analyses may produce results that can differ significantly from the measured seepage in the field. Therefore, probabilistic analyses that consider uncertainties often provide a more appropriate approach for seepage analysis of embankment dams.

Many researchers have used various geotechnical and hydraulic properties of the soil as random variables in these probabilistic analyses. Especially k, whose effect on seepage has already been clearly established, is a frequently used property in those studies [e.g.; 1, 3-9]. In addition to k, which is the most important parameter, α and n values, which are the suitability parameters of the van Genuchten water retention model, have also been among the parameters whose effect on seepage has been frequently investigated. Among these studies, Ahmed [4] investigated the seepage in embankment dams by probabilistic analysis, subjected the variable k to log-normal distribution and modelled the confined flow under a hydraulic structure using random field theorem. In the results of the study, it was determined that the amount of seepage was less than that calculated by deterministic methods for all values of coefficient of variation (COV) and fluctuation scale (Θ). Srivastava et al. [5] considered the value of k in a typical soil slope geometry as a log-normally distributed and spatially correlated random variable, and investigated the effect of this random variable on steady-state seepage flow and slope stability problems under steady-state seepage conditions. In the study of Le et al. [6], porosity and k were selected as random variables from heterogeneous material properties, and finite element analyses were performed by Monte Carlo (MC) simulation. Çalamak [1] investigated the effect of soil variability on seepage in three different types of hypothetical embankment dams by taking hydraulic conductivity and Van Genuchten parameters as random variables. Tan et al. [7] numerically simulated saturated-unsaturated seepage by combining MC simulation and random field theory to investigate the effect of the variability of hydraulic parameters on the flow in earthfill dams. Sensitivity analyses revealed that the coefficients of variation of the soil-water relationship characteristic curve (SWCC) parameter n and k_s have a greater influence on the seepage flow rate than the SWCC parameter α.

Based on these considerations, this study presents a probabilistic seepage analysis where k, α, and n are modeled as random variables to determine their effect on total seepage (Q). For this purpose, first, the statistical parameters mean (μ) and coefficient of variation (COV) were determined for k, α and n. Then, a hypothetical dam was created in accordance with the United States Bureau of Reclamation (USBR) criteria. Steady-state seepage analyses were performed on this hypothetical dam. The effect of the selected random variables on Q was investigated. Finally, the seepage within embankment dams is modeled by a new, simple, and robust optimization algorithm called teaching-learning based optimization (TLBO) and the conventional regression model (CRA) which were used in a number of previous studies in other fields of science and engineering [e.g., 10,11]. The TLBO algorithm is preferred because it has a small number of control parameters, and is therefore quite reliable. In addition, the fact that it gives relatively faster results compared to other swarm-based algorithms is also one of the reasons for its preference. Recently, this algorithm has started to be used in geotechnical problems involving retaining wall design and slope stability [12, 13]. This study distinguishes itself by pioneering an examination into the feasibility of employing the TLBO algorithm for modeling seepage in embankment dams, marking the first of its kind in this field.

2. CASE STUDY

A clay core embankment dam that was designed in accordance with the USBR criteria was employed for the analyses. The cross-section of the dam is given in Figure 1. The dam has a base length of 185 m, and a height of 30 m. The upstream and downstream slopes are 3:1 and 2.5:1, respectively. The core section has a width of 40 m, and slopes of 1:2. The typical geotechnical properties of the materials used for the upstream and downstream fill, and for the core are given in Table 1. Typical values from practice and literature were used when selecting deterministic material properties, except for permeability and van Genuchten parameters, which are modeled as random variables. In generating these random variables, particularly permeability, care was taken to ensure the values are plausible and acceptable in geotechnical and dam engineering practice. Detailed information on this consideration is provided in the random variable generation section. Note that using these material models and properties, Günay [14], in her study of probabilistic seepage at Büyükçekmece Dam, obtained results consistent with the measured seepage in the dam.

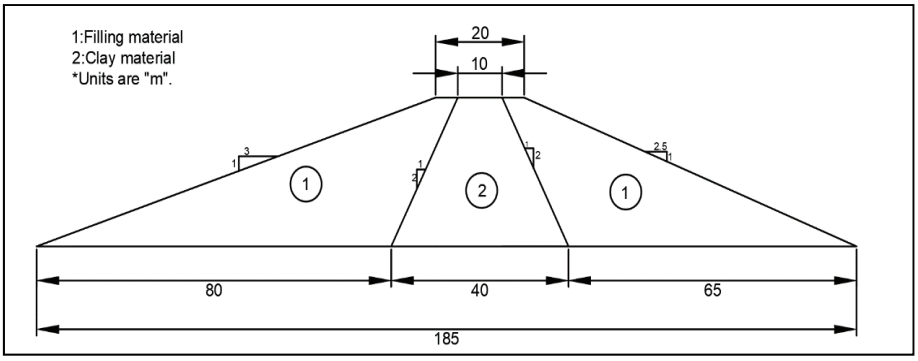

Figure 1 - Cross-section of the application dam

Table 1 - Material properties of the embankment dam

Parameter	Core	Fill	Unit
Soil model	Mohr-Coulomb	Mohr-Coulomb	-
Draninage type	Undrained(B)	Drained	-
γ	18	20	kN/m^3
γ_{unsat}	16	16	kN/m^3
Groundwater classification type	User defined	Hypres	-
$k_x = k_y$	Random variable	1	m/day
α	Random variable	-	m^{-1}
n	Random variable	-	-
E'_{ref}	1,500	20,000	kN/m^2
c'_{ref}	-	5	kN/m^2
$s_{u,ref}$	5	-	kN/m^2
E'_{inc}	300		kN/m^2/m
SWCC fitting model	Van Genuchten	Van Genuchten	-

3. METHODOLOGY

3.1. Finite Element Modelling

In this study, the finite element (FE) analyses for the seepage calculations were carried out using PLAXIS 2D Ultimate v22 [15]. Mohr-Coulomb soil model was deemed sufficient as the soil model, and "flow only" analysis type was used in the analyses. This type of analysis is more useful in problems that deal with fluid flow only. The finite element model was meshed to consist of 707 elements and 5,927 nodes. This mesh system is the finest mesh system (very fine) provided by PLAXIS 2D [15]. Van Genuchten [16] model and "user-defined" were employed for the SWCC curve of the materials. This allows α and n to be entered randomly. When determining the boundary conditions of the model, the bottom of the dam was completely closed to flow to focus solely on the flow within the dam body. Consequently, BoundaryXmin, BoundaryXmax, and BoundaryYmax were open to flow, while BoundaryYmin was closed to flow. The finite element model is shown in Figure 2.

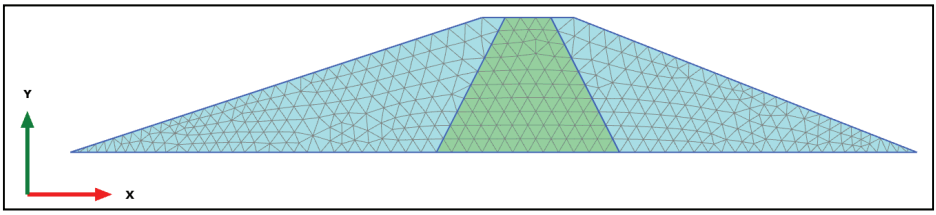

Figure 2 - PLAXIS 2D finite element model

Stochastic analyses were utilized to explore the impact of uncertainties in core k_s and Van genuchten parameters α and n on Q. In these stochastic analyses, Python software [17] embedded in PLAXIS 2D was used to run the MC simulations. PLAXIS 2D v14 and later versions offers a Python scripting interaction interface that makes it possible for users to input data [18, 19, 20]. The interface from PLAXIS to Python is shown in Figure 3.

```
In [1]: import imp
        from math import pi
        import time
        from math import log
        from math import sqrt
        from math import exp
        from math import pow
        from math import sin
        from math import cos
        import random
        import numpy as np
        from pytesseract import pytesseract
        from PIL import ImageGrab
        from PIL import Image
        import pyautogui
        import datetime

In [2]: # Python-Plaxis Bağlantısı
        localhostport_input = 10000
        localhostport_output = 10001
        plaxis_path = r"C:\ProgramData\Bentley\Geotechnical\PLAXIS Python Distribution V1\python\Lib\site-packages"
        found_module = imp.find_module('plxscripting', [plaxis_path])
        plxscripting = imp.load_module('plxscripting', *found_module)
        from plxscripting.easy import *
        s_i, g_i = new_server('localhost', localhostport_input, password = 'BeWxZQcgGtcarC9W')
        s_o, g_o = new_server('localhost', localhostport_output, password = 'BeWxZQcgGtcarC9W')
```

Figure 3 - Plaxis-Python connection [14]

3.2. Random Variable Generation

In the earlier stochastic seepage analyses, in addition to basic hydraulic and geotechnical properties such as k and k_s, Van Genuchten parameters (α and n) were also included in the analyses as random variables. In the current study, as in Li et al. [21] , and Calamak [1] , the k_s, α, and n were treated as random variables. Law [22], Bulnes [23], Warren and Price, [24], Bennion and Griffiths [25] show that k_s can be characterized by a log-normal distribution. In addition, Carsel and Parrish [26] show that α and n also follow a log-normal distribution. The essential statistical information, including the μ and the COV for the k_s, α, and n, was derived from Carsel and Parrish [26], which provides water retention relationships for twelve different soils. Specifically, these values for k_s were determined to be 0.062 m/day and 2.672, respectively [27]. Given the significant *COV(k_s)*, it is possible to produce a simulated k_s value that natural clay material would not typically exhibit. Therefore, values were initially generated with 0.5 COV(k_s). However, as the issue persists, it would be prudent, in accordance with the guidance provided by Casagrande [28], to limit the maximum k_s value to 10^{-4} cm/s, a value commonly associated with clays used in impervious sections of

Table 2 - Parameter values used in the study for k_s

Descriptive statistics	Random variable name			Reference
	k_s (m/day)	α (m^{-1})	n	Carsel and Parrish (1988)
COV	1.334	0.780	0.072	
μ	0.062	1.900	1.310	

```
iterasyon = 201
data = 1
sayacperm =[]
while data < iterasyon:
    muK=0.062
    COVK= 0.68
    u1=random.uniform(0,1)
    u2=random.uniform(0,1)
    sigmaK = COVK * muK
    sigmalnK = sqrt(log(1 + pow((sigmaK / muK), 2)))
    r = sqrt(-2.0 * log(u1)) * sin(2.0 * pi * u2)
    permeability = exp(log(muK) - 0.5 * pow(sigmalnK, 2) + sigmalnK * r)
    while permeability>0.0864:
        u1=random.uniform(0,1)
        u2=random.uniform(0,1)
        sigmaK = COVK * muK
        sigmalnK = sqrt(log(1 + pow((sigmaK / muK), 2)))
        r = sqrt(-2.0 * log(u1)) * sin(2.0 * pi * u2)
        permeability = exp(log(muK) - 0.5 * pow(sigmalnK, 2) + sigmalnK * r)
    print("permeability:" , permeability)
    sayacperm.append(permeability)
```

(a)

```
#İterasyon Başlangıç
iterasyon = 201
data = 1
while data < iterasyon:
    g_i.gotosoil()
    # Degisken Zemin Malzemelerinin Tanımlanıp Atanması
    material_kil= g_i.soilmat()
    permeability = p[data-1]
    #print("permeability",permeability)
    alfa = a[data-1]
    #print("alfa",alfa)
    n = b[data-1]
    #print("n",n)
    material_kil.setproperties(
        #other properties
        "ga",alfa,
        "gn",n,
        "perm_primary_horizontal_axis" , permeability,
        "perm_vertical_axis",permeability)
```

(b)

```
permeability =  0.061451357812616236
a value =  2.6259161240120217
n value =  1.3458530296192706
['‘Total discharge is 0,4852 m3/day/m\n']
```

(c)

Figure 4 - a, b: Random parameter generation and c, example of iteration output in Python

embankments. The mean value of 0.062 m/day represents a suitable k_s that aligns with the criteria proposed by Casagrande [28] for application in impermeable regions of dams and levees. In addition, related studies have shown that the $COV(k_s)$ value for k is in the range of 100-300% [27, 29, 30]. For the α, mean and COV values were taken as 1.90 m^{-1} and 0.78, respectively. The value taken for the mean is between 0.21-2.46 values suggested by Qu et al. [31]. For the n value, mean and COV values were taken as 1.31 and 0.072, respectively. The value assumed for the mean n is between 1.05-1.35, which is the range proposed in Qu et al. [31]. All the obtained values are summarized in Table 2. The Python code for random variable generation using the values given in Table 2 and an example iteration output is given in Figure 4.

3.3. Teaching-Learning Based Algorithm (TLBO)

TLBO is a population-based stochastic optimization algorithm inspired by the teaching-learning process in a classroom developed by Rao et al [32]. This algorithm has been used in many studies such as modeling dissolved oxygen, estimating energy consumption and determining suspended sediment load [10, 33, 34]. In this study, it will be used for the first time on seepage analysis in dams. In the proposed algorithm, each candidate solution is characterized by a set of variables representing a student's results, consisting of grades in different subjects [35]. This algorithm includes teaching and learning phases. The student who best fits the solution is selected as the teacher for the teaching phase. The teaching phase

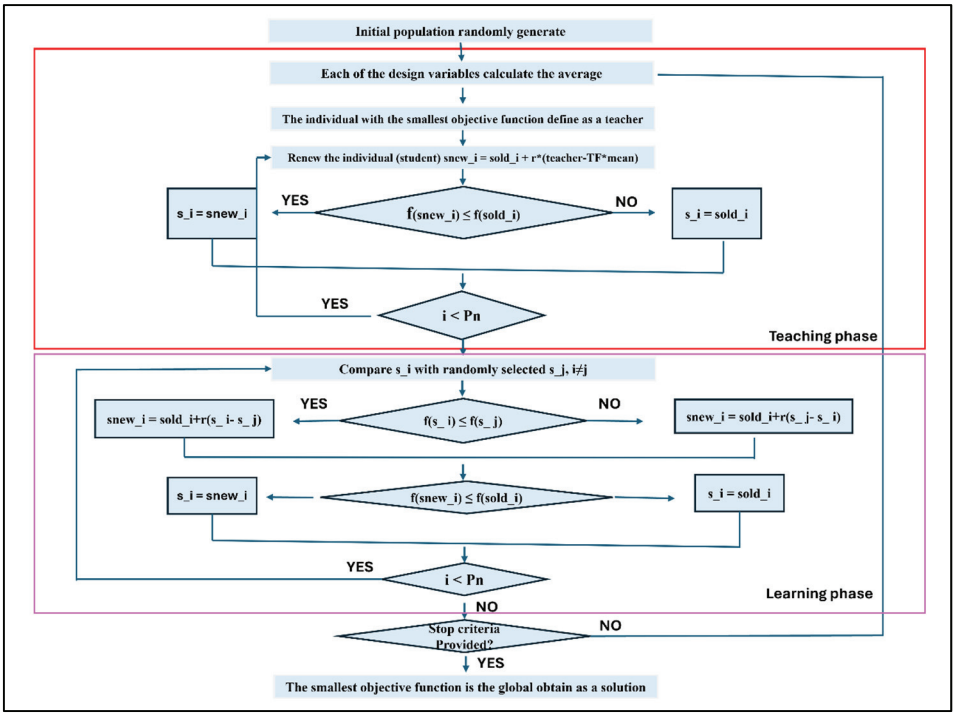

Figure 5 - Flow diagram of TLBO algorithm (Revised from [39])

is where students try to improve their results by getting information from the teacher. At the same time, the phase where students improve their performance by interacting with other students is called the learning phase [36]. The flow diagram of this algorithm is given in Figure 5. The reason why this algorithm is preferred over other algorithms such as the artificial bee colony algorithm or the ant colony algorithm, etc. is its simple digitized structure and independence from a set of control parameters to define the performance of the algorithm [10, 33, 37]. There are two control parameters in this algorithm. The first one is the population size, which is equal to the number of students. The other is the maximum number of cycles. The operation logic of this algorithm can be found in detail in Zou et al. [35] and [38].

The data is used as an input for the algorithm described above after being normalized using Eq.1. The objective function of the TLBO models is the sum square error (SSE). The regression equations have been evaluated by using data in the training set, and the best ones having the minimum SSE are determined. Also, performances of the TLBO and CRA models are evaluated using root mean square error (RMSE), mean absolute error (MAE), average relative error (ARE), and the coefficient of determination (R^2) for training and testing sets. SSE, RMSE, MAE, ARE and R^2 are obtained with Eqs. (2-6), respectively [40]. As the observed and estimated values converge, the Root Mean Square Error (RMSE), which is the standard deviation of the errors, decreases and approaches zero. The closer the RMSE is to zero, the better the correlation is in estimating the desired parameter [41]. In the literature, R^2 values between 0.9 and 1.0 indicate a perfect fit, while values between 0.75 and 0.9 indicate a very good fit [42].

$$Normalized\ value = \left(\frac{Raw\ value - minimum\ value}{Maximum\ value - minimum\ value}\right) \times (0.9 - 0.1) + 0.1 \quad (1)$$

$$\mathrm{SSE} = \sum_{i=1}^{N}(P_i - O_i)^2 \quad (2)$$

$$\mathrm{RMSE} = \left[\frac{1}{N}\sum_{i=1}^{N}(P_i - O_i)^2\right]^{1/2} \quad (3)$$

$$\mathrm{MAE} = \frac{1}{N}\sum_{i=1}^{N}|(P_i - O_i)| \quad (4)$$

$$\mathrm{ARE} = \frac{1}{N}\sum_{i=1}^{N}\left(\frac{(P_i - O_i)}{Pi}\right) \times 100 \quad (5)$$

$$R^2 = 1 - \left(\frac{\sum_{i=1}^{N}(P_i - O_i)^2}{\sum_{i=1}^{N}(P_i)^2}\right) \quad (6)$$

where;

N : the number of observations

O_i : the ith observed value

P_i : the ith estimated value for the regression functions

4. RESULTS AND DISCUSSION

FE analyses were conducted using the random variables k, α, and n, and the distribution of the resulting Q values is plotted in Figure 6. In this figure, the green line represents the deterministic Q result (obtained by keeping the random variables constant, Q_{det}). The red line represents the average Q value obtained probabilistically from 200 analyses. Note that the deterministically obtained value is less than the average of the probabilistically obtained values. Of the 200 Q values given in this histogram, 160 (80 %) were used in training and 40 (20 %) were used in testing. In the modeling phase, four regression functions, namely quadratic function (QF), exponential function (EF), linear function (LF), and hyperbolic function (HF), were used to estimate Q based on the analysis results. In the following, TLBO and CRA were used to optimize the unknown coefficients (w_i) of the independent variables (x_i).

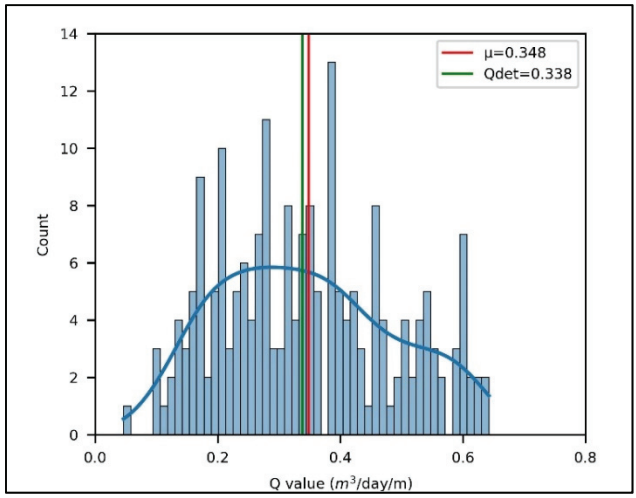

Figure 6 - Histogram of Q values

Using the data obtained from the FE analysis, TLBO and CRA were applied to QF, EF, LF, and HF. One of the major challenges is to determine the best parameters of TLBO, since any change in the algorithm parameters affect the performance of the algorithm. For this reason, different scenarios for TLBO parameters were tested and the most successful features were used. Accordingly, the maximum number of iterations (NMI) = 3000 was set as one of the control parameters of TLBO. The other control parameter, the population size (SP), was set to SP = 100 for linear and hyperbolic regression functions, and SP = 200 for quadratic and exponential functions. Once the control parameters were set, 20 independent runs were performed for each regression equation using TLBO. The control parameter values of the TLBO models yielding the best results for the functions are given in Table 3. CRA analyses were performed with SPSS, version 11.5 for Windows. The optimal coefficients obtained for the functions in the analysis results are presented in Table 4.

The results obtained from the equations and the test set that the equations have never seen before were compared with the probabilistic FE results and the best-fitting equations were

determined. The comparison is based on performance indices such as RMSE, MAE, ARE and R^2. The error values and R^2 for the training and testing sets using TLBO and CRA models are presented in Tables 5 and 6, respectively. After evaluating all equations, the best fitting equation is highlighted in bold for all error values.

Table 3 - The control parameter values of the TLBO and models yielding the best results

The functions	TLBO parameters	
	SP	NMI
Quadratic	200	3000
Exponential	200	3000
Linear	100	3000
Hyperbolic	100	3000

Table 4 - The coefficients obtained from the analysis

	Coefficients									
	w_0	w_1	w_2	w_3	w_4	w_5	w_6	w_7	w_8	w_9
TLBO	1.0084	0.9127	0.0069	-0.0037						
CRA	5.5860	0.8810	0.0450	-0.0050						
$y_{hyperbolic} = w_0 (x_1)^{w1}(x_2)^{w2}(x_3)^{w3}$										
TLBO	0.0325	0.9818	0.0142	0.0011						
CRA	-0.0037	7.2321	0.0317	-0.0002						
$y_{linear} = w_0 + (x_1)w_1+(x_2)w_2+(x_3)w_3$										
TLBO	-6.4455	1.8711	0.1374	0.0038	0.0013					
CRA	-18.148	2.8980	0.3900	0.0020	0.0001					
$y_{exponantial} = w_0 + exp(w_1 +(x_1)w_2+(x_2)w_3+(x_3)w_4)$										
TLBO	-0.0426	1.2226	-0.0003	0.1360	0.0455	-0.0578	0.0198	-0.2306	-0.023	-0.1233
CRA	-0.0500	8.7300	0.0690	0.0080	0.1910	-0.0410	-0.0070	-17.535	-0.0020	0.0010
$y_{quadratic} = w_0 + (x_1)w_1 + (x_2)w_2 + (x_3)w_3 + (x_1 x_2)w_4 + (x_1 x_3)w_5 + (x_2x_3)w_6 + (x_1^2)w_7 + (x_2^2)w_8 + (x_3^2)w_9$										

x_1: k, m/day ; x_2: n ; x_3: α, m^{-1} ; y : Q, m^3/day/m

Table 5 - The model results for training set

The functions	RMSE		MAE		ARE (%)		R^2	
	TLBO	CRA	TLBO	CRA	TLBO	CRA	TLBO	CRA
Hyperbolic	**0.0031**	0.0046	**0.0033**	0.0035	**1.0101**	1.0126	**0.9992**	0.9988
Linear	0.0070	0.0070	0.0058	0.0057	2.2710	2.9656	0.9968	0.9961
Exponential	0.0074	0.0082	0.0074	0.0073	3.2701	2.6687	0.9975	0.9973
Quadratic	0.0061	0.0070	0.0034	0.0035	1.4267	1.4808	0.9988	0.9989

Table 6 - The model results for testing set

The functions	RMSE		MAE		ARE		R^2	
	TLBO	CRA	TLBO	CRA	TLBO	CRA	TLBO	CRA
Hyperbolic	**0.0023**	0.0026	**0.0040**	0.0046	**0.8906**	0.8916	**0.9998**	0.9989
Linear	0.0093	0.0035	0.0079	0.0059	1.6767	1.8379	0.9984	0.9982
Exponential	0.0071	0.0039	0.0130	0.0072	2.1848	2.2585	0.9978	0.9986
Quadratic	0.0031	0.0038	0.0045	0.0035	0.8912	1.0263	0.9995	0.9992

It is clear from Tables 5 and 6 that the best-performing equations are obtained from hyperbolic functions using the TLBO algorithm. The minimum error value in the training and testing set was derived from HF with TLBO algorithm. The smallest ARE value for the training and testing sets were 1.0101% and 0.8906%, respectively in TLBO algorithm, and 1.0126% and 0.8916%, respectively in the CRA. According to the presented results, TLBO improved the performance of hyperbolic function by 32.6% in the training set, and by 11.54% in the testing set compared to CRA. Considering the error values for different function types (Tables 5, 6), it can be seen that the hyperbolic model gives the best result among all methods in both training and testing sets. Nonetheless, the alternative models also demonstrated exceptionally high performance, as evidenced by all R^2 values exceeding 0.99 with both TLBO and CRA methodologies.

Table 7 - The model results for training set with CRA results as a benchmark

The functions	RMSE	MAE	ARE	R^2
Hyperbolic	0.0339	**0.0032**	**1.7598**	**0.9499**
Linear	0.0345	0.0041	2.0790	0.9400
Exponential	0.0344	0.0055	2.4532	0.9373
Quadratic	**0.0321**	0.0035	1.7883	0.9479

Table 8 - The model results for testing set with CRA results as a benchmark

The functions	RMSE	MAE	ARE	R^2
Hyperbolic	0.0027	0.0022	**0.6570**	**0.9808**
Linear	**0.0018**	**0.0009**	0.8072	0.9794
Exponential	0.0060	0.0031	1.1121	0.9693
Quadratic	0.0049	0.0045	1.0773	0.9793

In addition, the results from CRA were utilized as a benchmark to validate the effectiveness of TLBO, and the outcomes obtained using TLBO were compared accordingly. Utilizing the results of CRA, which is more widely used than TLBO, provided more logical and reliable outcomes. The results of these analyses are presented in Tables 7 and 8 for the training and test sets, respectively.

Tables 7 and 8 clearly demonstrate that the best performance is again achieved using hyperbolic functions in the analyses where CRA results were used as a benchmark. The minimum error values in both the training and test sets were obtained from HF. Although a slight decrease in R^2 values is observed in the training set, the values remain between 0.93 and 0.95, indicating the model's robustness

5. CONCLUSIONS

In this study, for the first time, the ability of the Teaching-Learning-Based Optimization (TLBO) algorithm to predict total seepage (Q) in an embankment dam, based on the hydraulic and geotechnical properties of the clay core specifically saturated permeability (k_s) and van Genuchten parameters (α and n) is investigated. The main conclusions that can be drawn from the present study are as follows:

- The comparison of results using various performance indices clearly indicates that the best fit equations for each parameter are obtained from the hyperbolic function.
- The comparison of results demonstrates that the TLBO algorithm outperforms the CRA algorithm in predicting Q, as evidenced by a higher R^2 value and lower error metrics. For the training set, there was a 32% improvement in RMSE, a 5.7% improvement in MAE, and a 19.84% improvement in ARE. Additionally, the R^2 value increased by 4.5%. For the testing set, there was an 11.54% improvement in RMSE and a 13% improvement in MAE.
- To evaluate the reliability of TLBO, additional analyses were conducted using CRA results as a benchmark, comparing the performance of TLBO against CRA. The high R^2 values, ranging between 0.93 and 0.95, confirmed the model's accuracy.
- The equations derived using the TLBO algorithms successfully predict Q. Given this achievement, TLBO can serve as an effective optimization algorithm in seepage problems. Thus, a reasonable and reliable approximation for Q can be provided made by the equation obtained via TLBO.
- Based on the coefficients obtained, it is inferred that the probability distribution parameters of α and n have a lesser impact on Q compared to the parameter k_s.

Acknowledgements

This research did not receive any specific grant from funding agencies in the public, commercial, or not-for-profit sectors.

Author's Contributions

Conceptualization: Arife Gunay; Methodology: Arife Gunay, and Sami Oguzhan Akbas; Formal analysis and investigation: Arife Gunay; Writing - original draft preparation: Arife Gunay; Writing - review and editing: Sami Oguzhan Akbas; Supervision: Sami Oguzhan Akbas.

Fundings

No funding was received to assist with the preparation of this manuscript.

Data Availability

Data will be made available on request.

Declarations

Conflict of interest The author has no relevant financial or non-financial interests to disclose.

Ethics Approval There are no relevant waivers or approvals.

Consent to Participate Not applicable

Consent for Publication The authors allows publication if the research is accepted.

Financial interests The authors declare they have no financial interests.

Declaration of Competing Interest

The authors declare that they have no known competing financial interests or personal relationships that could have appeared to influence the work reported in this paper.

References

[1] Calamak, M., Uncertainty Based Analysis Of Seepage Through Eearthfill Dams. Ph.D. thesis, Dept. of Civ. Eng., Middle East Technical Univ., Ankara, Türkiye 2014.

[2] Polater, Ö., 2021. Infiltration Analysis Of Embankment Dams Using Different Impermeable Materials., M.Sc. Thesis, Dept. of Civ. Eng.,, Bitlis Eren Univ., Bitlis, Türkiye (in Turkish with English abstract) 2021.

[3] Fenton, G., Griffiths, D,. Statistics Of Free Surface Flow Through Stochastic Earth Dam. J. of Geotech. Eng., ASCE, 122(6), 410-427 1996. https://doi.org/10.1061/(ASCE)0733-9410(1996)122:6(427)

[4] Ahmed, A. A., Stochastic Analysis Of Free Surface Flow Through Earth Dams. Comput. Geotech, 36(7), 1186-1190 2009. https://doi.org/10.1016/j.compgeo.2009.05.005

[5] Srivastava, A., Babu, G. L. S., Haldar, S., Influence Of Spatial Variability Of Permeability Property On Steady State Seepage Flow And Slope Stability Analysis. Eng. Geology, 110(3-4), 93-101 2010. https://doi.org/10.1016/j.enggeo.2009.11.006

[6] Le, T. M. H., Gallipoli, D., Sanchez, M., Wheeler, S, J., Stochastic Analysis Of Unsaturated Seepage Through Randomly Heterogeneous Earth Embankments. Int. J. for Num. and Analytical Methods in Geomech., John Wiley & Sons, Ltd, 36(8), 1056–1076 2012. https://doi.org/10.1002/nag.1047

[7] Tan, X.; Wang, X., Khoshnevisan, S.,Hou, X., Zha, F., Seepage Analysis Of Earth Dams Considering Spatial Variability Of Hydraulic Parameters. Eng. Geology, 228, 260-269 2017. https://doi:10.1016/j.enggeo.2017.08.018.

[8] Siacara, A.T.,Beck, A. T., Futai, M. M., Reliability Analysis Of Rapid Drawdown Of An Earth Dam Using Direct Coupling. Comput. Geotech., 118, 103336 2019. https://doi.org/10.1016/j.compgeo.2019.103336

[9] Mouyeaux, A., Carvajal, C., Bressolette, P., Peyras, L.,Breul, P., Bacconnet, C., Probabilistic Analysis Of Pore Water Pressures Of An Earth Dam Using A Random Finite Element Approach Based On Field Data. Eng. Geology, 259, 105190 2019.

[10] Bayram, A., Uzlu, E., Kankal, M., Dede, T., Modeling Stream Dissolved Oxygen Concentration Using Teaching–Learning Based Optimization Algorithm. Environ. Earth Sci., 73, 6565-6576 2015.

[11] Nacar, S., Mete, B., Bayram, A., Estimation Of Daily Dissolved Oxygen Concentration For River Water Quality Using Conventional Regression Analysis, Multivariate Adaptive Regression Splines, And Treenet Techniques. Environ. Monitoring And Assest. vol.192, no.12 2020.

[12] Tayfur, B., Kamiloğlu, H. A. Optimization Of Cantilever Retaining Wall Design Using Improved Teaching-Learning-Based Optimization Algorithms. Firat University Journal of Experimental and Computational Engineering, 3(2), 134-150, 2024.

[13] Kalaivani, K., Priya, D. M., Veena, K., Brindha, K., Karuppasamy, K., Shanmugapriyaa, K. R. Consolidation Coefficient of Soil Prediction by Using Teaching Learning based Optimization with Fuzzy Neural Network. EAI Endorsed Transactions on Internet of Things, 10, 2024.

[14] Günay, A., Uncertainty-Based Investigation Of Seepage In Embankment Dams With Clay Core. M.Sc. Thesis, Dept. of Civ. Eng., Gazi Univ., Ankara, Türkiye (in Turkish with English abstract) 2023.

[15] PLAXIS 2D Material Reference Manuals, PLAXIS BV, Delft, The Netherlands: P, O, Box 572, 2600 AN 2022.

[16] Van Genuchten, M. T., A Closed -form Equation for Predicting the Hydraulic Conductivity of Unsaturated Soils. Soil Sc. Soc. of America J., 44(5), 892–898 1980.

[17] Python version 3 (Programing Language). The Python Software Foundation.

[18] Bozkurt, S., Application Of Finite Element Method In Geotechnical Risk Analysis: An Application For Supported Deep Excavations. M.Sc. Thesis, Dept. of Civ. Eng., Gazi Univ., Ankara, Türkiye (in Turkish with English abstract) 2019.

[19] Ucdemir G., Akbas S., Effect Of Wall Stiffness On Excavation-Induced Horizontal Deformations In Stiff-Hard Clays, Gazi Univ. J. of Sci. Part A: Eng. and Innovation, 113-130, 2023.

[20] Korkut D. E., Akbaş S. O., The Effect Of Incorporating Vertical Spatial Variability On The Probabilistic Analysis Of A Deep Excavation: A Case Study, J. Politecnic, 1-1, 2023.

[21] Li, W., Lu, Z., Zhang, D., Stochastic Analysis Of Unsaturated Fow With Probabilistic Collocation Method. Water Resour Res 45(8):W08425 2009. https://doi.org/10.1029/2008WR007530

[22] Law, J., A Statistical Approach To The Interstitial Heterogeneity Of Sand Reservoirs. Transactions Of The AIME, Soc. of Petroleum Eng., 155(1), 202-222. 1944. https://doi.org/10.2118/944202-G

[23] Bulnes, A. C., An Application Of Statistical Methods To Core Analysis Data Of Dolomitic Limestone. Transactions of the AIME, Soc. of Petroleum Eng., 165(1), 223-240 1946. https://doi.org/10.2118/946223-G

[24] Warren, J. E., Price, H. S.: Flow In Heterogeneous Porous Media. SPE J., Soc. Of Petroleum Eng., 1(3), 153-169 1961. https://doi.org/10.2118/1579-G

[25] Bennion, D. W., Griffiths, J. C., A Stochastic Model For Predicting Variations In Reservoir Rock Properties. SPE J., Soc. of Petroleum Eng., 6(1), 9-16 1966. https://doi.org/10.2118/1187-PA

[26] Carsel, R. F., Parrish, R. S., Developing Joint Probability Distributions Of Soil Water Retention Characteristics. Water Res. Res., 24(5), 755-769 1988. https://doi.org/10.1029/WR024i005p00755

[27] Günay, A., Akbaş, S. O. Kil Çekirdekli Dolgu Barajlarda Kararlı Durum Sızmasının Olasılıksal Analizi. Politeknik Dergisi1-1. (2024). https://doi.org/10.2339/politeknik.1418676

[28] Casagrande, A., Notes on soil mechanics-first semester. Harvard University (unpublished), 129 p 1938.

[29] Baecher, G. B., Christian, J. T., Reliability And Statistics In Geotechnical Engineering. John Wiley & Sons 2005.

[30] Wang, F., Huang, H., Yin, Z., Huang, Q., Probabilistic Characteristics Analysis For The Time-Dependent Deformation Of Clay Soils Due To Spatial Variability. European J. of Environ. and Civ. Eng., 26(12), 6096-6114 2022. https://doi.org/10.1080/19648189.2021.1933604

[31] Qu, Z., Guanhua, G., Yang, J., Evaluation Of Regional Pedotransfer Functions Based On The BP Neural Networks. In International Conference on Comput. and Computing Tech. in Agriculture (pp. 1189-1199). Boston, MA: Springer US 2008.

[32] Rao, R.V., Savsani, V. J., Vakharia, D. P., Teaching-Learning-Based Optimization: A Novel Method For Constrained Mechanical Design Optimization Problems. Comput Aided Des 43:303–315 (2011).

[33] Uzlu, E., Kankal, M., Akpınar, A.,Dede, T., Estimates Of Energy Consumption In Türkiye Using Neural Networks With The Teaching–Learning-Based Optimization Algorithm. Energy, 75, 295-303 2014.

[34] Yılmaz, B., Aras, E., Nacar, S., Kankal, M., Estimating Suspended Sediment Load With Multivariate Adaptive Regression Spline, Teaching-Learning Based Optimization, And Artificial Bee Colony Models. Sci. of the Total Environ. , vol.639, 826-840 2018.

[35] Zou, F., Chen, D., Xu, Q.: A Survey Of Teaching–Learning-Based Optimization. Neurocomputing, 335, 366-38 2019.

[36] Ermis, S., Bayindir, R., Yesilbudak, M., Voltage Stability Study in Power Systems With İmproved Teaching-Learning Based Optimizatıon Algorithm. Gazi Univ. J. of Sci. Part C: Design and Tech., 11(3), 695-705 2023.

[37] Togan, V.: Design Of Planar Steel Frames Using Teaching– Learning Based Optimization. Eng Struct 34:225–232 2012.

[38] Dede, T.: Optimum Design of Grillage Structures To LRFD-AISC With Teaching-Learning Based Optimization. Struct Multidisc Optim 48:955–964 2013.

[39] Uzlu, E., Physical Modelling Of The Accretion Profile Resulting From The Movement Of Solids Perpendicular To The Shore. P.Hd. Thesis, Dept. Of Civ. Eng., Karadeniz Tech. Univ., Trabzon, Türkiye (In Turkish with English Abstract) 2016.

[40] Akbulut, H., Gevrek, L. A., Ay, M. Modeling of Asphalt Pavement Surface Temperature for Prevention of Icing on the Surface. *Turkish Journal of Civil Engineering*, *35*(2), 1-21. 2024.

[41] Tuc, E., Akbas, S. O., Babagiray, G. Reliability and Validity Analysis of Correlations on Strength and Consolidation Parameters for Ankara Clay and Proposal for a New Correlation. Arabian Journal for Science and Engineering, 1-20, 2024.

[42] Demirgül, T., Demir, V., Sevimli, M. F. Farklı makine öğrenmesi yaklaşımları ile Türkiye'nin solar radyasyon tahmini. Geomatik, 9(1), 106-122, 2024.

Turkish Journal of Civil Engineering, 2025, 97-119, Paper 801, ***Research Article***

Experimental Study of Evolution of Breach Resulting from Piping at Upper Part of Earth-Fill Dam

Mehmet Şükrü GÜNEY[1]
Merve OKAN[2*]
Emre DUMLU[3]
Aslı BOR[4]
Gökmen TAYFUR[5]
Pelin AKLIK[6]

ABSTRACT

Piping and overtopping are the most important causes of earth-fill dam failure. Such dams may erode under seepage, causing a reduction in the structural strength. The aim of this study was to investigate the temporal evolution of the breach and flow rate from the breach resulting from the piping in earth-fill dams. The experiments were carried out at Hydraulics Laboratory of Civil Engineering Department of İzmir University of Economics. The dam was constructed by using a mixture consisting of 85 % sand and 15 % fine (low plasticity clay). In the first scenario a circular tunnel with a diameter of 2 cm was created along the centreline at 6 cm below the dam crest whereas in the second one it was located at the upper edge. Six cameras at different locations recorded the evolution of the progress of the breach formation. The pump flow rate was measured by magnetic flow meter, and the continuity equation was used to calculate the flow rate values from the breach. The time-varied values of the total breach areas were determined using the Gauss Area formula. The image processing method

Note:
- This paper was received on March 27, 2024 and accepted for publication by the Editorial Board on November 8, 2024.
- Discussions on this paper will be accepted by May 31, 2025.
- https://doi.org/10.18400/tjce.1459836

1 Izmir University of Economics, Department of Civil Engineering, İzmir, Türkiye
sukru.guney@ieu.edu.tr - https://orcid.org/0000-0003-1441-4784

2 Izmir University of Economics, Department of Civil Engineering, İzmir, Türkiye
merve.okan@ieu.edu.tr - https://orcid.org/0000-0001-6095-2992

3 The University of Mississippi, National Center for Computational Hydroscience and Engineering, Oxford, USA
edumlu@go.olemiss.edu - https://orcid.org/0000-0003-4311-3040

4 Norwegian University of Science and Technology Trondheim, Norway
Izmir University of Economics, Department of Civil Engineering, İzmir, Türkiye
asli.b.turkben@ntnu.no - https://orcid.org/0000-0002-1679-5130

5 Izmir Institute of Technology, Department of Civil Engineering, İzmir, Türkiye
gokmentayfur@iyte.edu.tr - https://orcid.org/0000-0001-9712-4031

6 Izmir University of Economics, Department of Civil Engineering, İzmir, Türkiye
pelin.aklik@ieu.edu.tr - https://orcid.org/0000-0002-0070-2307

* Corresponding author

was also applied in the determination of the breach areas. The time-dependent changes of water depth in the channel were also recorded. The obtained experimental findings are presented and commented, together with the universal dimensionless curves. The failure of the dams occurred mainly because of the head cut erosion developed from downstream to upstream. When breaching started, the orifice flow was converted to open channel flow where breach bottom behaved like a broad crested weir. In the second scenario, the rigid lateral side considerably influenced the flow rate and the development of the breach. The peak flow rate corresponding to the first scenario was found approximately 2.3 times greater than that of the second one. The maximum values of all the breach parameters were reached earlier in the case of the seepage along the centerline. The ratios between the values corresponding to the first and the second scenarios were found as 3.25 and 1.75 for maximum breach areas at downstream and at upstream sides, respectively. These ratios were 2.44 and 1.37 for the average breach widths at downstream and upstream sides, respectively. A very good agreement was found between the area values obtained from Gauss area method and image processing technique, in both scenarios. This fact demonstrated that either of these two approaches can be used to determine the time-dependent breach areas. These experimental findings provide the opportunities for the calibration and validation of the numerical models used in the relevant numerical investigations. This study also offers guidance for the strategies concerning emergency action plans related to the failure of homogeneous earth-fill dams when the piping starts at upper part of the homogeneous earth-fill dams.

Keywords: Earth-fill dam, piping, breach geometry, breach development, discharge from the breach.

1. INTRODUCTION

Piping due to seepage is considered to be one of the main causes of the dam failure. Piping, caused by seepage, stands as a primary contributor to dam failures. Zhong et al. (2021) [1] analyzed more than 3500 historical cases of embankment dam failures; one of the major failure modes is due to piping/seepage accounting for 35% of all. Internal erosion encompasses processes where soil particles are eroded within or beneath the embankment due to seepage, manifesting itself as final mechanism of backward erosion piping [2]. Piping is a process where seepage forces cause the removal of fine particles along a path from the upstream to the downstream face of a structure [3]. As internal erosion progresses, piping can lead to breaching, with the loss of material escalating the risk of collapse in geotechnical structures due to high seepage pressures [4]. Once the piping channel becomes large enough, the outflow through the breach increases, accelerating the failure. A notable example is the Teton Dam failure, where initial piping triggered internal erosion through cracks in the key trench fill, ultimately leading to the dam's complete collapse, resulting in 11 fatalities and extensive property damage [5].

Temporal development of the breach resulting from piping depends on various factors including the porous medium characteristics, the flow parameters, the dams' geometric properties as well as the piping location. Earth-fill dams are more susceptible to internal erosion and piping due to seepage. As internal erosion and piping due to seepage are the main causes of failure in these dams, the control of seepage is extremely important in dam design and construction [6].

Soil composition plays a vital role in the breach initiation time, breach formation time, breach width, breach height, and the peak outflow. These breaching factors present a significant threat to life and property in the downstream of a dam [7].

Dhiman and Patra (2020) [7] investigated the influence of the soil properties on the breaching process by means of small-scale cohesive and non-cohesive embankments. In all experiments, the embankment height was 0.3 m with a crest width of 0.1 m. The mean particle size (d_{50}) of CL soil and sand were 0.018 mm and 0.52 mm, respectively. The average breach width decreased by 67.5% when the proportion of fine particles was increased from 6% to 16%. Zhu et al. (2011) [8] built 5 embankments (1 with pure sand and 4 with various sand-silt-clay mixtures) to investigate breach evolution. They found that cohesive soil embankments eroded slowly and were significantly affected by head cut erosion. Morris et al. (2008) [9] revealed that instead of simplified approaches, more realistic approaches are required about the breach mechanism as well as the breach geometry and flow through the breach.

Zomorodian et al. (2020) [10] constructed homogeneous earthen dams 0.15 m high, 0.35 m wide and created a groove of 1 cm square at 14 cm from the bottom. The test material was a mixture of uniform sand and fine-grained soil. Their results revealed that the initiation and development of the erosion by overtopping depended on the soil compaction level. Sharif et al. (2015) [11] investigated the piping erosion process in an earthen embankment by creating a hole at the bottom of the dam to initiate the piping. The soil mixture used in these experiments consisted of 64% medium sand, 29% silt and 7% clay. They obtained empirical formulas to predict the erosion depth, the area of vertical erosion and the eroded volume. The ratio of the average erosion depth to the average erosion bottom width was found to be close to one. Elkholy et al. (2015) [12] investigated the piping erosion process in an earthen embankment by creating a hole at the bottom of the dam to initiate the piping. Different soil mixtures classified as silty sand were used with constant upstream head. The researchers reported the occurrence of the maximum depth of erosion on the upstream side and the maximum bottom width of erosion on the downstream side.

Annunziato et al. (2024) [13] analyzed the Derna dam break event that occurred in Libya in September 2023. They modelled the dam break, estimated the flood extent, established its timeline, and compared the model results with the available qualitative or quantitative post-event information.

In various numerical studies, the shape of the breach is typically considered trapezoidal. However, the breach shape actually depends on several parameters including the dam geometry, soil properties, hydraulic conditions as well as the seepage location. Numerous experiments with different scenarios are needed to provide accurate data for use in numerical analyses. Since many images in the literature show breaches in their last stages, it is also important to identify and take into account how the geometry of the breach changes with time.

In the literature, there have been many studies on dam failures, particularly those caused by overtopping, but there exist limited piping experiments because of relative difficulties to perform them. This study is a part of the project TUBITAK 119M609, supported financially by the Scientific and Technological Research Council of Turkey. The aim of this project is to investigate the temporal evolution of the breach and flow rate through the breach resulting

from piping starting at different locations of the earth-fill dams. The experiments were carried out at Hydraulics Laboratory of Civil Engineering Department of İzmir University of Economics. The experiments were performed on homogeneous earthen dams, constructed from a mixture of 85 % sand and 15 % fine (low plasticity clay). For the first scenario, a circular tunnel with a diameter of 2 cm was created along the centerline, 6 cm below a homogeneous dam crest whereas in the second one it was located at the upper corner. These scenarios were presented in two different international scientific meetings [14, 15]. The experiments were performed by designing and building dam bodies in laboratory flumes with significant dimensions compared to those available in the literature concerning such experiments performed in the laboratory. The experimental setup, experimental procedures, and soil properties are described in detail. The obtained experimental findings are presented and commented. The objective of this study is to conduct experiments to investigate the development of dam failure resulted from the piping starting at upper part of the earth-fill dams to provide insights into the breach mechanism and data to the relevant researchers who deal with numerical analyses and emergency action plans.

2. EXPERIMENTAL PROCEDURE

The experimental dam was built in a rectangular channel of 1 m wide, 0.81 m high and 5.44 m long, as shown in Fig. 1. The dam having a height of 0.6 m, a bottom width of 2 m and a

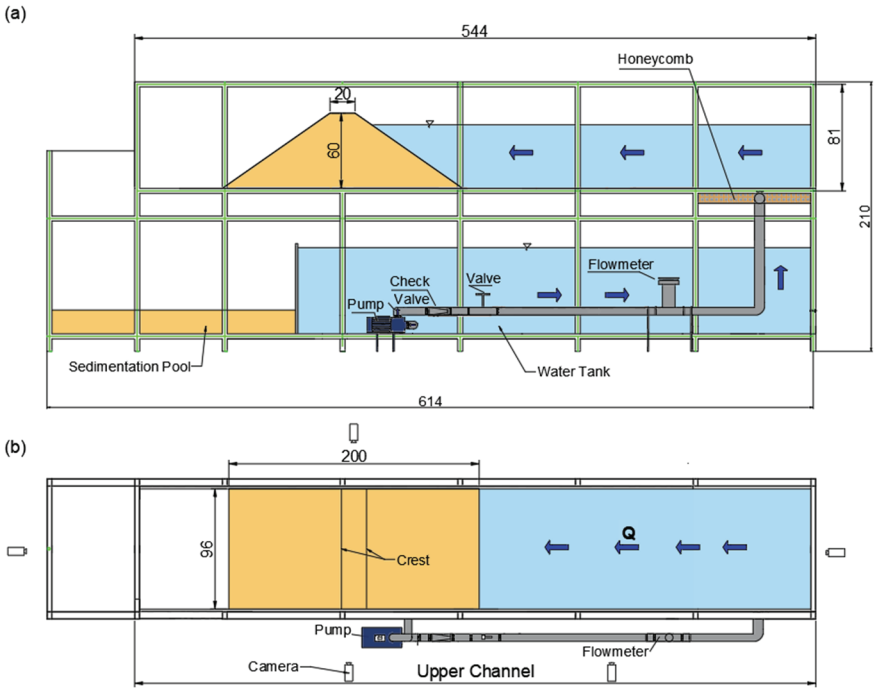

Figure 1 - Experimental system (a) side view, (b) plan view (All dimensions are in cm)

crest width of 0.20 m was built in the upper channel. The slopes of the upstream and downstream sides were set to 1:1.5. Water circulated between the lower reservoir and the upper channel by means of a pump. Soil mechanics tests were carried out in the laboratory before the construction of the dam.

The grain-size distribution curve for soil mixture obtained from sieve analysis (ASTM D-6913) and hydrometer analysis (ASTM D-7928) is given in Fig. 2a. Some characteristic diameter values are as follow; D_{10}=0.006 mm, D_{30}= 0.075 mm, D_{50}= 0.3 mm, and D_{60}= 0.4 mm. The coefficients of uniformity and gradation were found as C_u =66.7 and C_c =2.34, respectively. The soil classified as Clayey Sand with a corresponding symbol SC according to Unified Soil Classification System. The specific gravity for the mixture was found as SG= 2.63 (ASTM D854 – 23).

Proctor test (ASTM D-698) was performed to obtain the maximum dry unit weight and the optimum water content (Fig. 2b). From Fig. 2b, $\Upsilon_{dry,max}$= 1.794 gr/cm^3 and w_{opt} = 12.5 %. In the experiments, the energy was reduced by 50 % in order to facilitate the occurrence of piping. The applied compaction energy was 309 kJ/m^3. Hence, the number of blows applied for each layer during the construction of the dam was 13 instead of 25. In the experiments, the bulk density of 1.997 g/cm^3 was satisfied for each layer. Before the compaction, each layer was 14 cm thick and after the compaction it was reduced to 10 cm.

The constant head permeability test (ASTM D-2434) was performed to determine the hydraulic conductivity of the mixture. The coefficient of permeability was obtained as k=0.00047 cm/s. From the Atterberg test (ASTM D-4318), LL was found to be equal to 17.5 %. From the direct shear test (ASTM D-3080) two important parameters for the soil were evaluated as cohesion c= 15.33 kPa and internal friction angle ϕ = 33.93°. According to the consolidation test (ASTM D-2435-04) results, the compression index C_c =0.1, the swell index C_s = 0.007, the recompression index, C_r = 0.009, and E_{oed}= 35714 kPa. The unconfined compression test (ASTM D2166-00) was realized with 3 different loading increments. The unconfined compression index C_{un} value was found as 9.95 kPa.

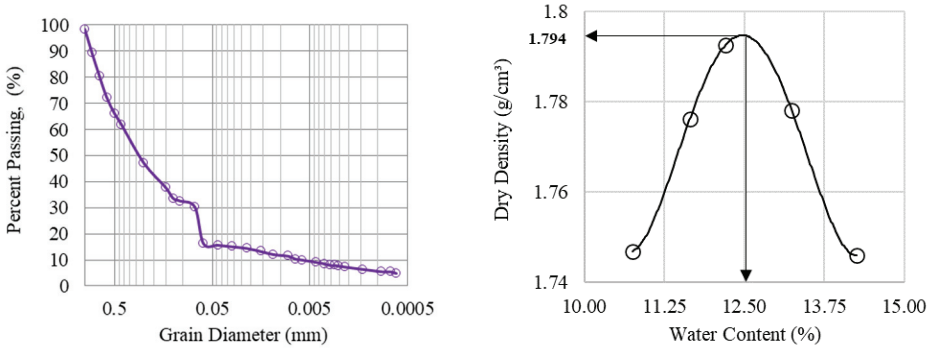

(a) (b)

Figure 2 - a) Grain size distribution of soil mixture with sieve analysis and hydrometer analysis b) dry density versus water content graph

The properties of the mixture used in the dam construction are summarized in Table 1.

Table 1 - Soil mixture Properties

% Fine (Low plasticity clay)	15
% Sand	85
Cohesion, c (kPa)	15.3
Angle of Friction, ϕ (°)	33.9
Specific Gravity, SG	2.63
D_{50} (mm)	0.3
The coefficient of Permeability (cm/s)	0.00047
Liquid Limit, LL (%)	17.5
Optimum Water Content (%) (25 blows)	9.8
Max. Dry Density (g/cm³) (25 blows)	1.886
Optimum Water Content (%) (13 blows)	12.5
Max. Dry Density (g/cm³) (13 blows)	1.794
Oedometric modulus of deformation, E_{oed} (kPa)	35714

The dam was constructed layer by layer. Each layer of 14 cm was compacted so that its thickness becomes 10 cm by using Proctor Hammer and plate. Some construction stages and finished shape of the dam body are given in Fig. 3.

Figure 3 - Some construction stages: (a) Compacting by proctor hammer, (b) After compaction of the first layer, (c) After compaction of the last layer, (d) Final shape

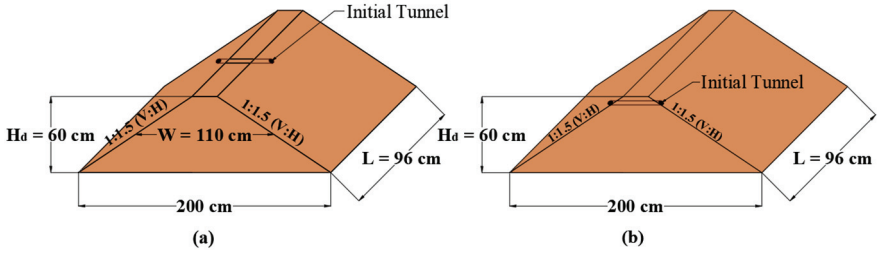

Figure 4 - Schematic views of the dam body corresponding to seepage a) along centerline b) at corner

In order to generate the formation of the breach, a circular hole of 2 cm diameter lying from upstream to downstream was created at 54 cm from the bottom of the dam body (Fig. 4).

3. EXPERIMENTAL RESULTS

The pump flow rate was measured by a magnetic flowmeter. The evolution of the dam failure was recorded by six cameras placed at different locations. In order to adjust the water level, an electromagnetic sensor was attached which starts and stops the pump when water depths in the channel were 0.540 m and 0.555 m, respectively.

The ratio of the local hydraulic gradient to critical hydraulic gradient determines whether the local particle migrates by seepage forces [16, 17, 18 and 19]. The critical hydraulic gradient, i_{cr}, was calculated by $i_{cr} = \frac{(\gamma_{sat}-\gamma_w).(1-n)}{\gamma_w}$; where n is the porosity, γ_{sat} is the saturated unit weight, and γ_w is the unit weight of water [16]. In this study, by using respectively numerical values of 0.32, 21.2 kN/m^3, and 10 kN/m^3, it was obtained as $i_{cr} = 0.76$.

3.1. Case 1: Piping at the Upper Part along the Centerline

The temporal developments of the breach recorded by the cameras located at downstream and upstream of the dam are given in Fig. 5 and Fig. 6, respectively. The time t=0 corresponds to the starting of the seepage [15, 19]. As seen in Figures 5 and 6, there was head cut erosion proceeding from downstream to upstream. The breach formation started at downstream side first and progresses backward to upstream side.

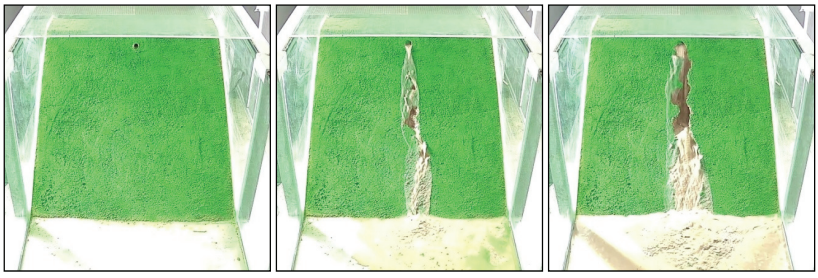

t= 0 *t=52 s* *t=80 s*

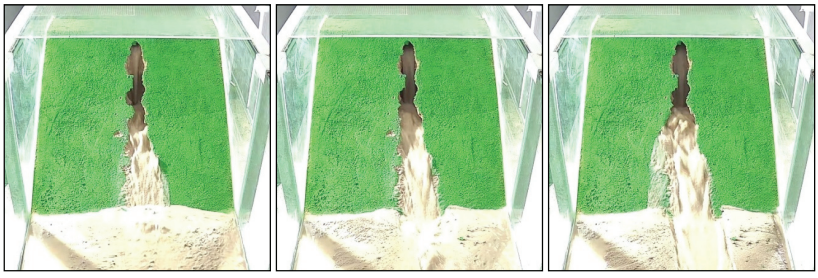

t=120 s *t=160 s* *t= 180 s*

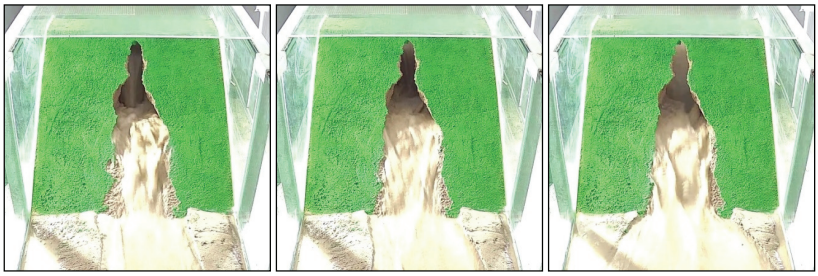

t= 230 s t=280 t= 380 s

Figure 5 - The temporal development of the central breach at downstream

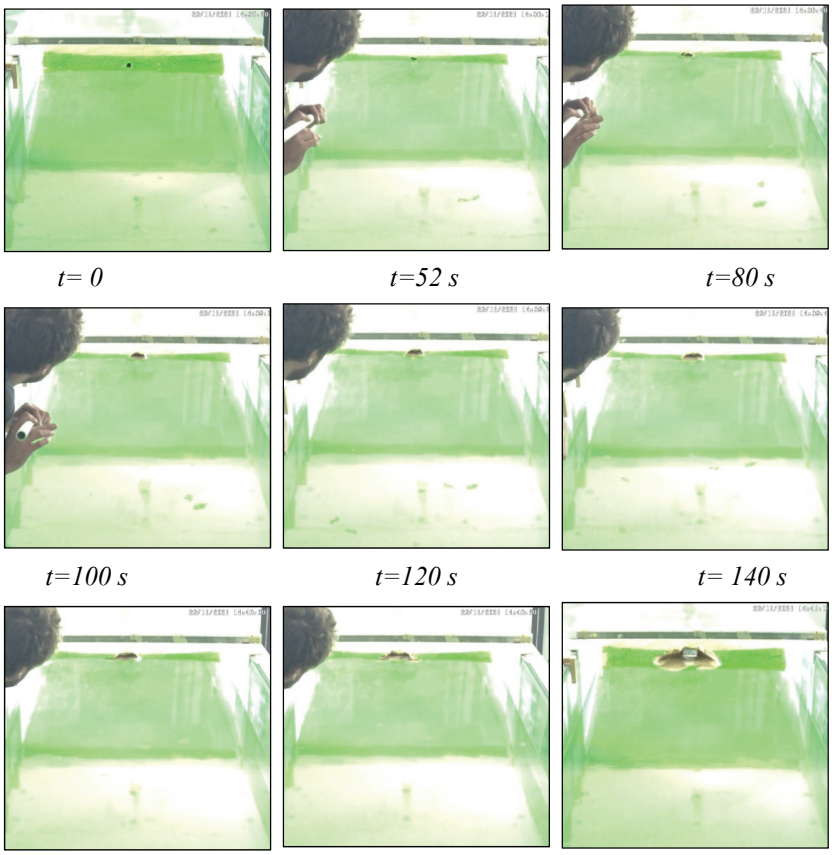

t= 0 t=52 s t=80 s

t=100 s t=120 s t= 140 s

t= 160 s t=180 s t= 230 s

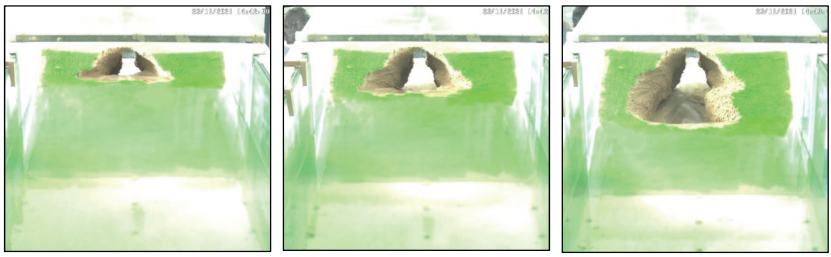

t=280 s *t= 330 s* *t=380 s*

Figure 6 - The temporal development of the central breach at upstream

The water depths in the channel were obtained from the related camera recordings.

The discharge of water outgoing from the breach was determined by using the continuity equation:

$$\Delta S=(Q_{pump}- Q)\cdot\Delta t \quad (1)$$

where Q_{pump} is the flow rate delivered by the pump, Q is the discharge from the breach, and ΔS is the storage in the channel during the time interval Δt.

The time-varied water level in the upstream reservoir and average discharge from the central breach are given in Fig. 7.

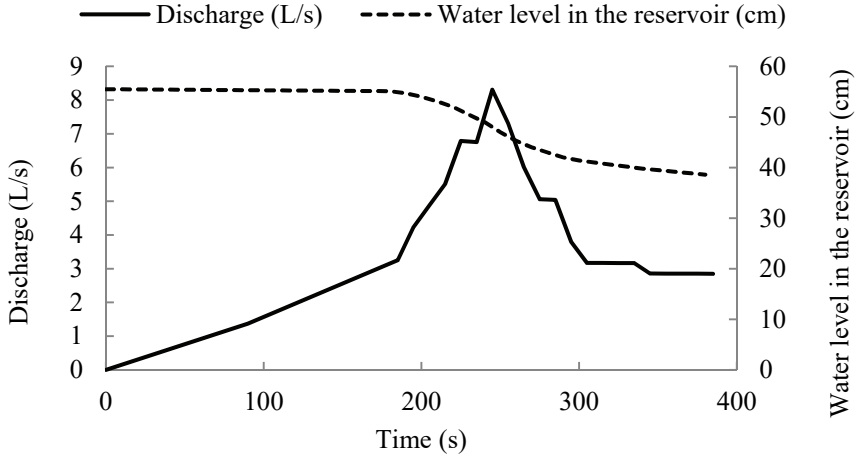

Figure 7 - Time-varied water level in the upstream reservoir and average discharge from the central breach

The maximum discharge from the breach was calculated as Q_{max}=8.31 L/s at t=245 s.

The geometry of the breaches was obtained by examining the images of the cameras located at upstream, downstream and lateral sides. In order not to work with fisheye images, the

videos acquired from lateral camera recordings were edited and straightened using the Hit-film-Express version 2021.1. Besides, extra sensitive solutions were applied to ensure that the images were completely flat. The images obtained from the records corresponding to a certain time were scaled and the boundary coordinates of the breaches were determined in the Get-data Graph Digitizer 2.26 environment.

The time-varied breach areas were calculated by using the Gauss area formula:

$$Area = \frac{1}{2}\sum_{i=1}^{n} x_i(y_{i+1} - y_{i-1}) = \frac{1}{2}\sum_{i=1}^{n} y_i(x_{i+1} - x_{i-1}) \quad (2)$$

where n is the number of sides, x_i and y_i represent the abscissa and ordinate in the coordinate i, respectively.

The temporal variations of the central breach area at downstream and upstream are presented in Fig. 8.

During the experiment, the breach initiated on the downstream side and then evolved towards to upstream side. As expected, there was a delay in the evolution of the breach at upstream side. At downstream the breach reached its maximum value at t=370 s and remained nearly constant while at upstream side the evolution of the breach continued, and its maximum value was greater than that at downstream.

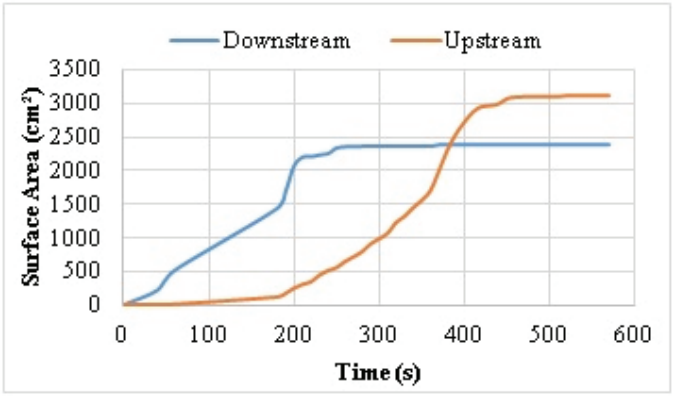

Figure 8 - Temporal variations of the central breach area at downstream and upstream

The maximum breach surface area at the upstream was found to be A_{umax}= 3128.7 cm^2 at t=520 s.

At downstream A_{dmax}= 2379.3 cm^2 at t=370 s and remained unchanged afterwards.

3.2. Case 2: Piping at the Upper Part Corner

This scenario was realized to enable better visualization of the breach development by means of the transparent glass side and the temporal developments of the breach recorded by the

cameras located at downstream, upstream and lateral side of the dam are shown in Figs. 9, 10 and 11, respectively. The time t=0 indicates the beginning of the seepage [14, 19].

t=0 s *t=220 s* *t=340s*

t=680 s *t=1020 s* *t=1360 s*

Figure 9- The temporal development of the corner breach at downstream

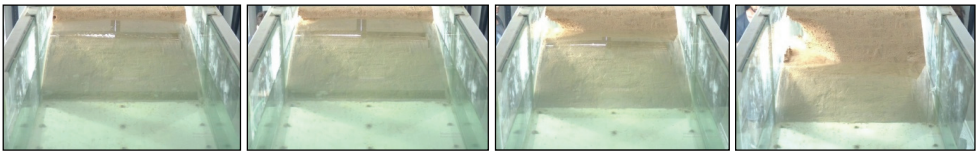

t=0 s *t=220 s* *t=340s* *t=680 s*

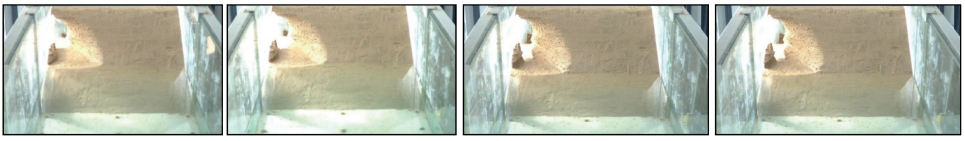

t=1020 s *t=1360 s* *t=1700s* *t=2040 s*

Figure 10 - The temporal development of the corner breach at upstream

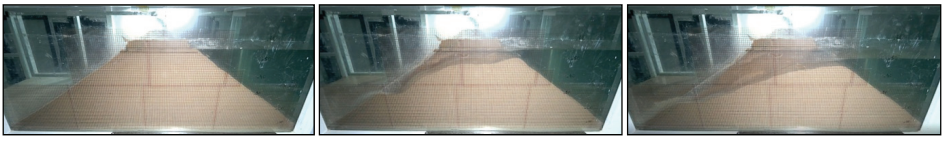

t=0 s *t=220 s* *t=340 s*

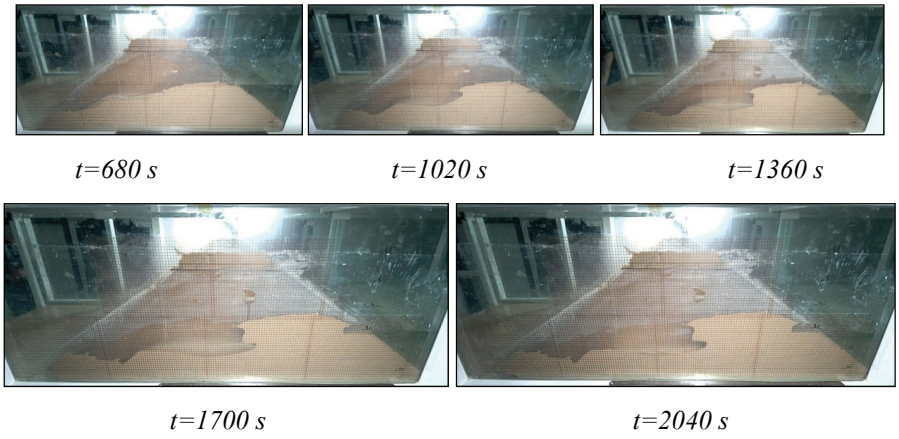

Figure 11 - The temporal development of the corner breach at lateral side

The time-varied water level in the upstream reservoir and average discharge from the corner breach are given in Fig. 12.

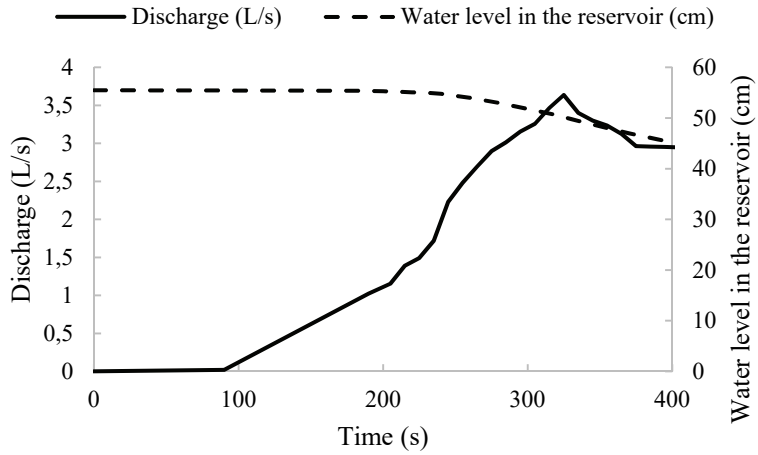

Figure 12 - Time-varied water level in the upstream reservoir and average discharge through the corner breach

The maximum discharge from the breach was calculated as Q_{max}=3.64 L/s at t=320 s. The peak flow rate was found to be quite smaller compared to that found in the 1st scenario (8.31 L/s) and this value was reached later (320 s instead of 245 s.).

The temporal variations of the corner breach area at downstream, upstream and lateral side are presented in Fig. 13.

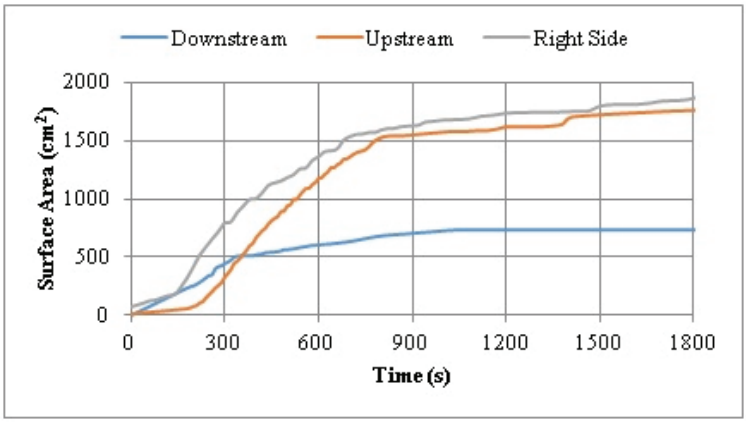

Figure 13 - Temporal variations of the corner breach area at downstream, upstream and lateral side

Some comparative experimental findings are given in Table 2.

The maximum values of all the parameters given in Table 2 were reached earlier in the case of the seepage along the centerline.

Table 2 - Comparison of some experimental parameters

Case (Scenario) number	1	2
Location of the seepage	Upper center	Upper corner
Max. flow rate Q_{max} (L/s)	8.31	3.64
t_Q= time to reach Q_{max} (s)	245	320
Max. breach area at downstream A_{dmax} (cm^2)	2379	733
t_d=time to reach A_{dmax} (s)	370	1080
Max. breach area at upstream A_{umax} (cm^2)	3129	1792
t_u=time to reach A_{umax} (s)	520	1950
Max. avg. breach width at downstream B_{dmax} (cm)	22	9
$t_{B,d}$=time to reach B_{dmax} (s)	370	520
Max. avg. breach width at upstream B_{umax} (cm)	41	30
$t_{B,u}$=time to reach B_{umax} (s)	390	580

Likewise, it was observed that the breach started at the downstream side and then developed towards to upstream side. The delay in the development of the breach at upstream was found to be smaller compared to the 1st scenario. The breach surface area of the upstream was recorded at a maximum level of A_{umax}=1760 cm^2 at t =1800 s. At downstream A_{dmax}= 732 cm^2 at t=1080 s and remained unchanged, also A_{latmax}= 1875 cm^2 at t=1800 s.

4. USE OF IMAGE PROCESSING TECHNIQUE TO ASSESS THE EVOLUTION OF BREACH

The image processing technique was also used to monitor the erosion process for the breach surface area.

Since it was not possible to apply spray paint to the glass side, the surface where erosion occurs was painted with green colour on Matlab environment by using "drawpolygon" command in order to display the eroded area for the case 2.

Matlab Color Thresholder – HSV was used to detect the breach surface areas. The breach areas were obtained by adjusting the HSV colour space. In this study, H, S, and V values were adjusted to detect colours other than green.

Fig.14 illustrates the bottom erosion lines and the average erosion depths corresponding to the 2nd case.

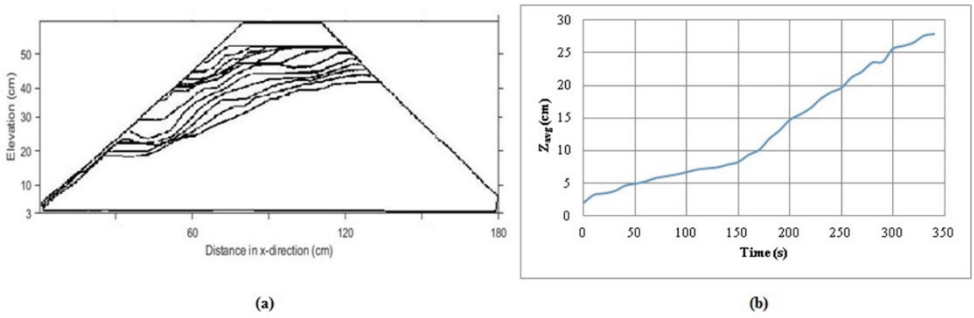

Figure 14 - a) Bottom erosion lines for every 30 seconds (starting from t=10 sec) b) Temporal variation of the average erosion depths for case 2

As seen from this figure the average breach depth developed rather slowly in the first half of the experiment period while it developed nearly twice as fast in the second half. Besides, when the first half of the experiment period was completed, the edge of bottom erosion line reached the upstream surface of the dam, and then it was observed that there was an increase in the development of breach depth at the second half of the period.

The time dependent image processing using Matlab Color Thresholder for downstream and upstream sides of the dam corresponding to the 1st case are given in Figs. 15 and 16, respectively.

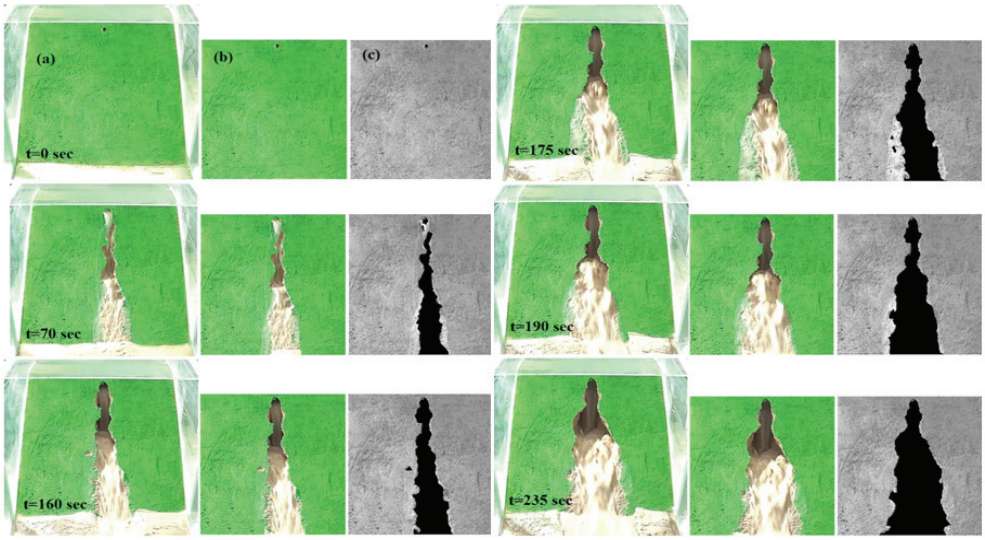

Figure 15 - Time dependent image processing using Matlab Colour Thresholder for downstream – HSV. a) Original picture from experiments. b) Cropped Image c) After Colour Thresholding for case 1

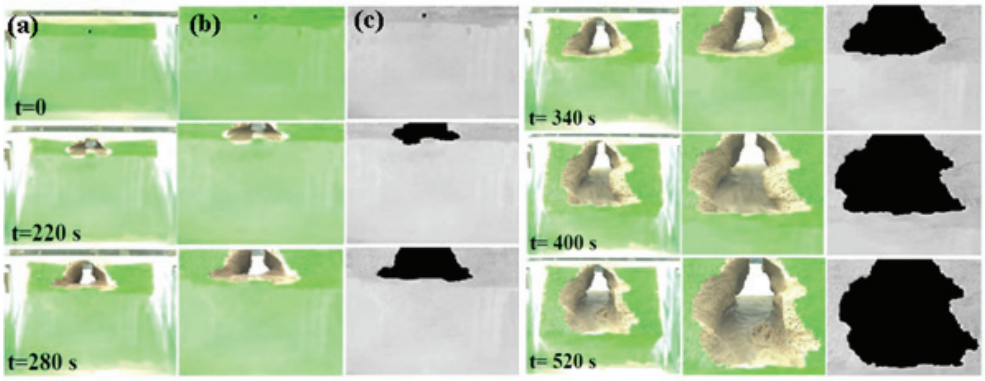

Figure 16. Time dependent image processing using Matlab Colour Thresholder for upstream - HSV. a) Original picture from experiments. b) Cropped Image c) After Colour Thresholding for case 1

Figure 17 represents the evaluation of eroded lateral area at different time instants for the 2nd case.

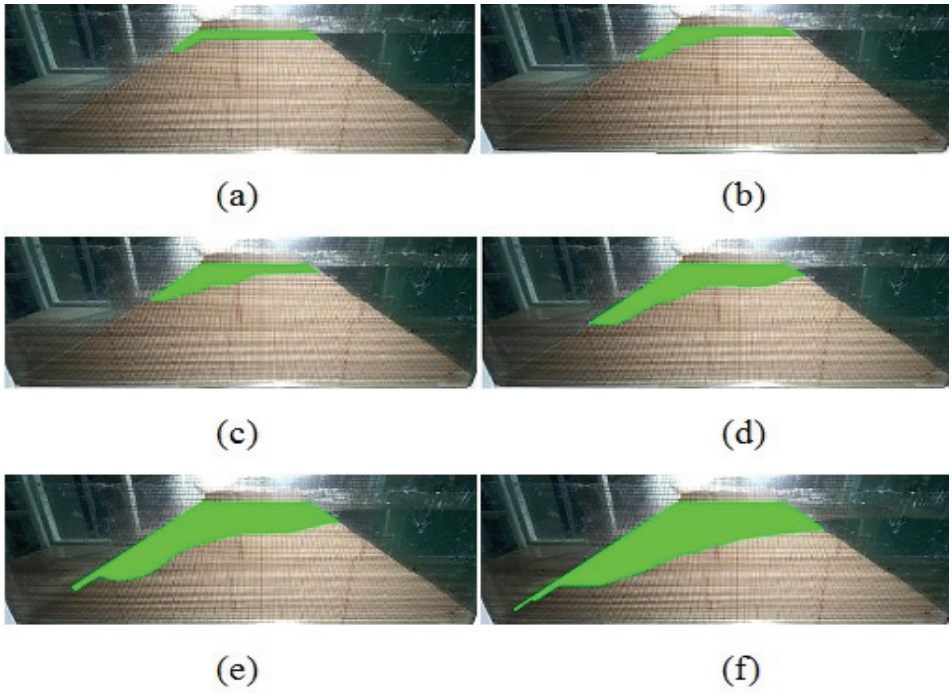

Figure 17 - The evaluation of eroded side area at different time instants a) t=10 sec, b) t=70 s, c) t=130 sec, d) t=190 sec, e) t= 250 sec, f) t=310 sec for case 2

The calculated breach area values were compared with those obtained from the Gauss Area method (Figs. 18 and 19).

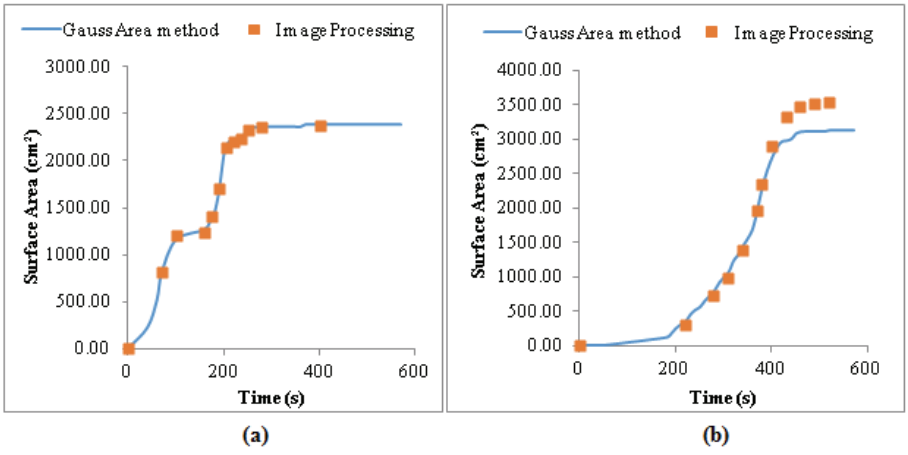

Figure 18 - Comparison of Gauss Area method and Image Processing results for case 1 a) at downstream b) at upstream

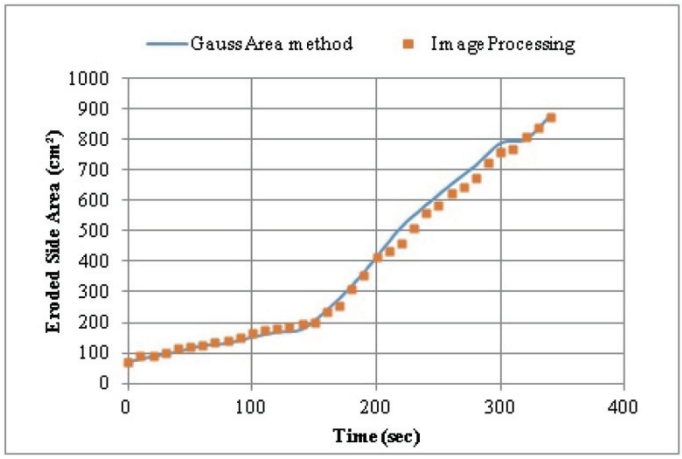

Figure 19 - Comparison of Gauss Area method and Image Processing results for the 2nd case

A very good agreement was found between the area values obtained from these two different approaches for both cases 1 and 2. Consequently, it was demonstrated that either of these approaches can be used to determine the time-dependent breach areas.

5. COMPARISON OF THE EXPERIMENTAL RESULTS BY DIMENSIONLESS CURVES

The dimensionless time-dependent curves were also generated to obtain the universal curves which can be used in the cases of homogeneous earth-fill dams having different dimensions and under various hydraulic conditions.

The dimensionless parameters are generated by dividing the time dependent values of the parameter in question to its maximum value. The time elapsed to reach the maximum flow rate Q_{max} is denoted by $t_{Q.}$ Similar subscripts are used for the maximum value of other parameters. The obtained dimensionless time varied flow rates, breach areas and breach widths versus dimensionless time curves are given in Figs 20, 21, 22, 23 and 24, respectively.

It was revealed that the dimensionless flow rates versus dimensionless time could be considered as two segment lines with two different slopes and two different stages, the first slope being smaller. The first stage lasted much longer in the 1st scenario.

The dimensionless breach areas versus dimensionless time in the 2nd scenario could be approximated to two segment lines while in the 1st scenario the linear behavior appeared only in the first stage.

The tendency of the dimensionless curves at upstream were found to be very different in the 1st and 2nd scenarios. The evolution of the dimensionless breach areas was nearly exponential in the 1st scenario whereas the evolution can be considered as combination of the straight

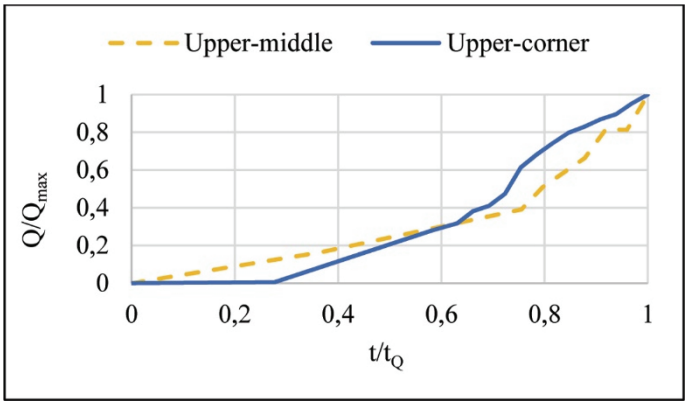

Figure 20 - Dimensionless flow rates versus dimensionless times curves

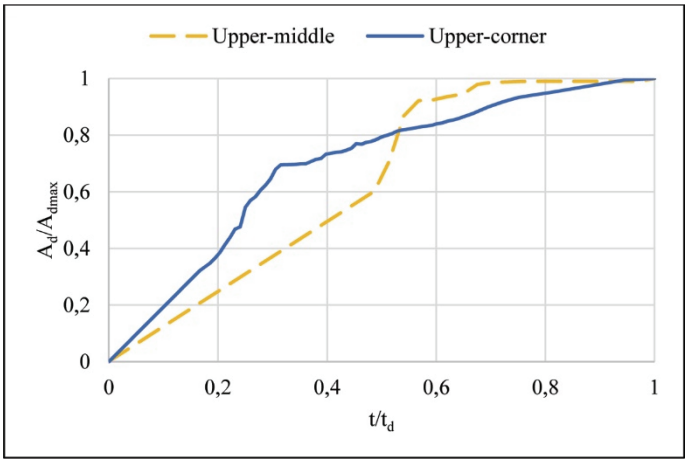

Figure 21 - Dimensionless breach areas at downstream versus dimensionless times curves

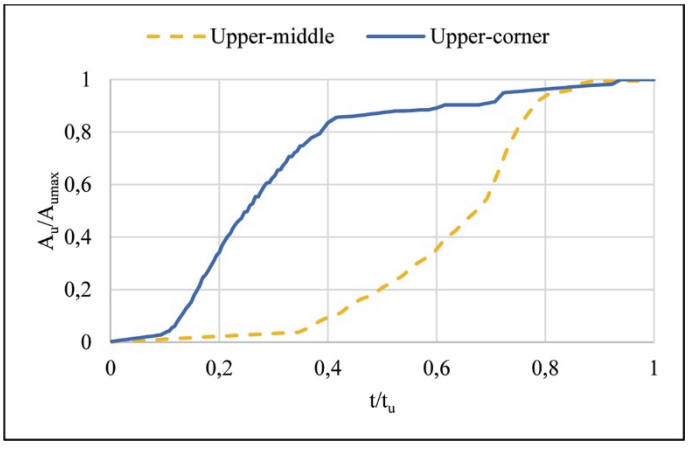

Figure 22 - Dimensionless breach areas at upstream versus dimensionless times curves

lines when the seepage initiated at corner. Besides, the upstream breach area was significant when t=0.4 t_u in the 2nd scenario while at this time the breach area was quite small and then increased significantly in the 1st scenario.

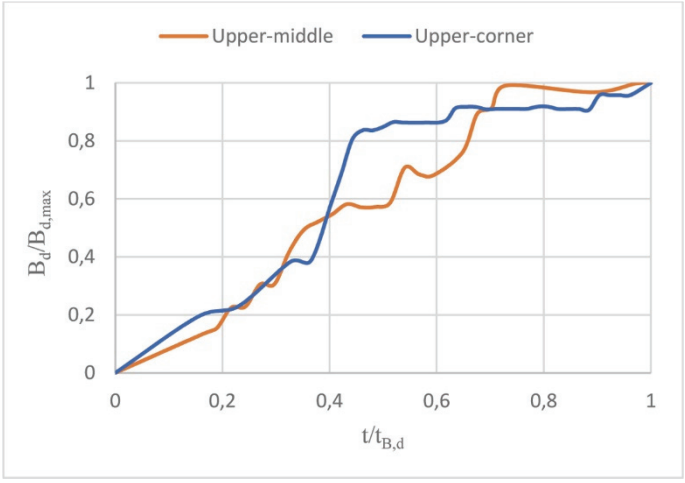

Figure 23 - Dimensionless breach widths at downstream versus dimensionless times curves

When t= 0.50 $t_{B,d}$ the breach width at downstream was almost B_d= 0.85 $B_{d,max}$ in the 2nd scenario, while B_d= 0.58 $B_{d,max}$ in the case of the 1st scenario.

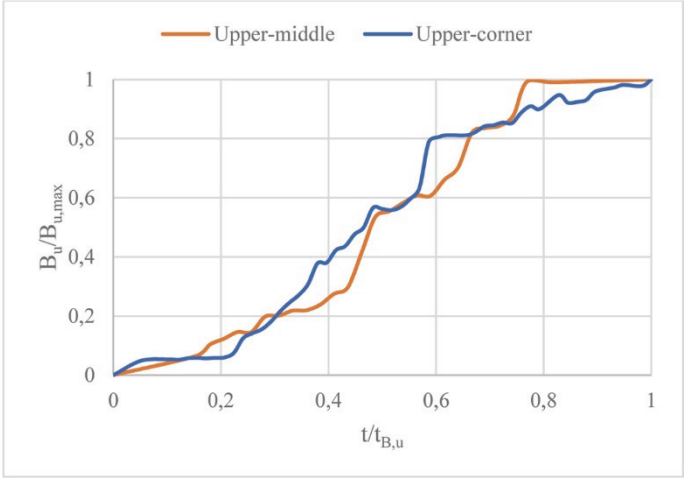

Figure 24 - Dimensionless breach widths at upstream versus dimensionless times curves

When t= 0.50 $t_{B,u}$ the breach width at upstream was approximately B_u= 0.48 $B_{u,max}$ in both cases. In the 2nd scenario, the dimensionless breach width developed continuously but in the 1st scenario there was no change in dimensionless breach width beyond t= 0.76 $t_{B,u}$.

Nevertheless, the best compatibility was obtained in the case of the dimensionless upstream breach widths for both scenarios.

6. CONCLUSIONS

In this study, the failure of dam occurred mainly because of the head cut erosion. Head cut erosion directly started at the downstream surface of the dam where seepage initiated. While the water was seeping through the circular tunnel the material of the dam was moved away. Due to eroded material, piping enlarged causing the transportation of more material. Head cut erosion developed from downstream towards upstream. When breaching started, the orifice flow was converted to open channel flow where breach bottom behaved like a broad crested weir. At the same time, breach experienced widening until head cut reached the upstream surface. Afterwards, breach continued to enlarge longitudinally toward to channel bottom.

The breach areas obtained by using the Gauss area functions were found to be in accord with those obtained from the image processing method.

In the 2nd scenario, the lateral side being rigid influenced considerably the flow rate and the development of the breach. The peak flow rate corresponding to the 1st case was found to be approximately 2.3 times greater than that of 2nd case.

The maximum breach areas and average breach widths were found to be lower in the 2nd case due to the limited available space for the breach development. Consequently, the ratios between the values corresponding to the 1st and 2nd scenarios were found as 3.25 and 1.75 for maximum breach areas at downstream and at upstream sides, respectively. These ratios were 2.44 and 1.37 for the average breach widths at downstream and upstream sides, respectively.

This study revealed the temporal development of the breach mechanism in the cases where the seepage is located at the upper middle or upper corner of homogeneous earth-fill dam. In both cases the maximum breach areas and average breach widths at upstream side of the dam were found to be greater compared to those observed at downstream.

The dimensionless curves corresponding to time-dependent flow rates, breach areas and breach widths were also generated in order to get universal curves, making possible their use in the cases of other homogeneous earth-fill dams having different dimensions and under various hydraulic conditions, when the seepage starts at upper part of the dams.

These experimental findings provide the opportunities for the calibration and validation of the numerical models used in the relevant numerical investigations. This study also offers guidance for the strategies concerning emergency action plans related to the failure of homogeneous earth-fill dams when the seepage starts at upper part of the dams.

Since the piping phenomenon is a complicated phenomenon depending on several factors, it would be very useful to perform numerous experimental studies on the homogeneous earth-fill dams constructed with different mixtures, possessing different geometry with different piping locations. It would also be interesting to perform such experiments on earthen dams with clay core. A numerical model calibrated and validated according to such experimental findings would make possible the investigation of the behavior of the real dams in the case of piping.

Symbols

A_d : temporal breach area at downstream

A_u : temporal breach area at upstream

A_{umax} : maximum breach area at upstream

$A_{d\,max}$: maximum breach area at downstream

A_{latmax} : maximum lateral breach area

B_d : temporal breach width at downstream

B_u : temporal breach width at upstream

C : cohesion

C_c : coefficient of gradation or compression index

CL : low plasticity clay

C_s : swell index

C_u : coefficient of uniformity

C_{un} : unconfined compression index

C_r : recompression index

D : grain diameter

E_{oed} : Oedometric modulus of deformation

H_d : dam height

I : coordinate

i_{cr} : critical hydraulic gradient

k : coefficient of permeability

L : dam length

LL : Liquid Limit

n : porosity

SC : clayey sand

SG : specific gravity

Q : discharge from the breach

Q_{max} : maximum flowrate from the breach

Q_{pump} : flowrate delivered from the pump

x_i : abscissa

y_i : ordinate

w_{opt} : optimum water content

ΔS : storage in the channel

Δt : time interval

γ_w : unit weight of water

γ_{sat} : saturated unit weight

$\gamma_{dry,max}$: maximum dry unit weight

ϕ : internal friction angle

Acknowledgements

The authors thank the Scientific and Technological Research Council of Turkey (TUBITAK) for supporting financially this study through the project 119M609.

References

[1] Zhong, Q., Wang, L., Chen, S., Chen, Z., Shan, Y., Zhang, Q., Ren, Q., Mei, S., Jiang, J., Hu, L., & Liu, J., Breaches of embankment and landslide dams - State of the art review. Earth-Science Reviews, 216, 103597, 2021. https://doi.org/10.1016/j.earscirev.2021.103597

[2] Robbins, B. A., & van Beek, V. M., Backward erosion piping: A historical review and discussion of influential factors. Association of State Dam Safety Officials, Dam Safety 2015, September, 2015.

[3] ASCE/EWRI Task Committee on Dam/Levee Breaching, Earthen Embankment Breaching. Journal of Hydraulic Engineering, 137, 12, 1549–1564, 2011. https://doi.org/10.1061/(ASCE)HY.1943-7900.0000498

[4] Sellmeijer, J. B. On the mechanism of piping under impervious structures [Bibliotheek Technische Universiteit], 1988. http://repository.tudelft.nl/assets/uuid:7f3c5919-1b37-4de9-a552-1f6e900eeaad/TR diss 1670(1).pdf

[5] Teton Dam History & Facts . http://www.usbr.gov/ssle/damsafety/index.html, 2016.

[6] Al-Janabi A.M.S., Ghazali A.H., Ghazaw Y.M., Afan H.A., Al-Ansari N., and Yaseen Z.M., Experimental and numerical analysis for earth-fill dam seepage. Sustainability, 12(6),2490, 2020. https://doi.org/10.3390/su12062490.

[7] Dhiman, S., and Patra, K. C., Experimental study of embankment breach based on its soil properties. ISH Journal of Hydraulic Engineering, Taylor & Francis, 26, 3, 247–257, 2020.

[8] Zhu, Y., Visser, P. J., Vrijling, J. K., and Wang, G., Experimental investigation on breaching of embankments. Science China Technological Sciences, 54, 1, 148–155, 2011.

[9] Morris, M., Hassan, M., Kortenhaus, A., Geisenhainer, P., Visser, P., and Zhu, Y., Modelling breach initiation and growth. Flood Risk Management: Research and Practice, 581–591, 2008.

[10] Zomorodian, S. M. A., Noghab, M. J. A., Zolghadr, M., and O'Kelly, B. C., Overtopping erosion of model earthen dams analysed using digital image-processing method. Proceedings of the Institution of Civil Engineers: Water Management, 173, 6, 304–316, 2020.

[11] Sharif, Y. A., Elkholy, M., Hanif Chaudhry, M., and Imran, J., Experimental Study on the Piping Erosion Process in Earthen Embankments. Journal of Hydraulic Engineering, 141, 7, 04015012, 2015.

[12] Elkholy, M., Sharif, Y. A., Chaudhry, M. H., and Imran, J., Effect of soil composition on piping erosion of earthen levees. Journal of Hydraulic Research, 53, 4, 478–487, 2015.

[13] Annunziato, A., Santini, M., Proietti, C., Girolamo, L., Lorini, V., Gerhandinger, A., Tucci, M., Modelling and Validation of the Derna Dam Break Event GeoHazards, 5, 2, 504-529, 2024. https://doi.org/10.3390/geohazards5020026.

[14] Guney, M. S., Dumlu, E., Okan, M., and Tayfur, G., Experimental Study of Breach Evolution and Discharge Through Breach Resulting from Piping due to Seepage at the Upper Corner of in an Earth-Fill Dam. 14th International Conference on Hydroscience & Engineering (ICHE 2022) MAY 26-27, 2022, İzmir, Turkey, 99–109, 2022a.

[15] Guney, M. S., Okan, M., Dumlu, E., Bor, A., Aklık, P., and Tayfur, G., Experimental Study of the Evolution of the Breach and the Discharge Through the Breach Resulting from Piping due to Seepage at the Earth-Fill Dam Top. Proceedings of the 39th IAHR World Congress 19-24 June 2022, Granada, Spain, 2735–2743, 2022b.

[16] Ojha, C. S. P., Singh, V. P., and Adrian, D. D., Influence of Porosity on Piping Models of Levee Failure. Journal of Geotechnical and Geoenvironmental Engineering, 127, December, 1071–1074, 2001.

[17] Richards, K. S., and Reddy, K. R., Critical appraisal of piping phenomena in earth dams. Bulletin of Engineering Geology and the Environment, 66, 4, 381–402, 2007.

[18] Terzaghi, K., Peck, R. B., and Mesri, G., Soil mechanics in engineering practice. Wiley, New York, 1996.

[19] Okan, M., Experimental and Numerical Investigation of Piping in Uniform Embankment Dam with Weak Layer at the Upper Region. M.Sc. Thesis, İzmir Institute of Technology, 2022.

Turkish Journal of Civil Engineering (formerly Teknik Dergi)
Manuscript Drafting Rules

1. The whole manuscript (text, charts, equations, drawings etc.) should be arranged in Word and submitted in ready to print format. The article should be typed on A4 (210 x 297 mm) size paper using 10 pt (main title 15 pt) Times New Roman font, single spacing. Margins should be 40 mm on the left and right sides and 52.5 mm at the top and bottom of the page.
2. Including drawings and tables, articles should not exceed 25 pages, technical notes 10 pages.
3. Your contributed manuscript must be sent over the DergiPark system. (http://dergipark.gov.tr/tekderg)
4. The text must be written in a clear and understandable language, conform to the grammar rules. Third singular person and passive tense must be used, and no inverted sentences should be contained.
5. Title must be short (10 words maximum) and clear, and reflect the content of the paper.
6. Sections should be arranged as: (i) abstract and keywords, (ii) title, abstract and keywords in the other language, (iii) main text, (iv) symbols, (v) acknowledgements (if required) and (vi) references.
7. Both abstracts should briefly describe the object, scope, method and conclusions of the work and should not exceed 100 words. If necessary, abstracts may be re-written without consulting the author. At least three keywords must be given. Titles, abstracts and keywords must be fitted in the first page leaving ten line space at the bottom of the first page and the main text must start in the second page.
8. Section and sub-section titles must be numbered complying with the standard TS1212.
9. Symbols must conform to the international rules; each symbol must be defined where it appears first, additionally, a list of symbols must be given in alphabetic order (first Latin, then Greek alphabets) at the end of the text (before References).
10. Equations must be numbered and these numbers must be shown in brackets at the end of the line.
11. Tables, drawings and photographs must be placed inside the text, each one should have a number and title and titles should be written above the tables and below the drawings and photographs.
12. Only SI units must be used in the manuscripts.
13. Quotes must be given in inverted commas and the source must be indicated with a reference number.
14. Acknowledgement must be short and mention the people/ institutions contributed or assisted the study.
15. References must be numbered (in brackets) in the text referring to the reference list arranged in the order of appearance in the text. References must include the following information:

    If the reference is an article: Author's surname, his/her initials, other authors, full title of the article, name of the journal, volume, issue, starting and ending pages, year of publication.

    Example : Naghdi, P. M., Kalnins, A., On Vibrations of Elastic Spherical Shells. J. Appl. Mech., 29, 65-72, 1962.

    If the reference is a book: Author's surname, his/her initials, other authors, title of the book, volume number, editor if available, place of publication, year of publication.

    Example : Kraus. H., Thin Elastic Shells, New York. Wiley, 1967.

    If the reference is a conference paper: Author's surname, his/her initials, other authors, title of the paper, title of the conference, location and year.

    If the source is a thesis: Author's surname, his/her initials, thesis title, level, university, year.

    If the source is a report: Author's surname, his/her initials, other authors, title of the report, type, number, institution it is submitted to, publication place, year.
16. Discussions to an article published in Turkish Journal of Civil Engineering (formerly Teknik Dergi) should not exceed two pages, must briefly express the addressed points, must criticize the content, not the author and must be written in a polite language. Authors' closing remarks must also follow the above rules.
17. A separate note should accompany the manuscript. The note should include, (i) authors' names, business and home addresses and phone numbers, (ii) brief resumes of the authors and (iii) a statement "I declare in honesty that this article is the product of a genuinely original study and that a similar version of the article has not been previously published anywhere else" signed by all authors.
18. Copyright has to be transferred to UCTEA Turkish Chamber of Civil Engineers. The standard copyright form signed by the authorised author should therefore be submitted together with the manuscript.

CONTENTS

RESEARCH ARTICLE

UCTEA Turkish Chamber of Civil Engineers
TMMOB İnşaat Mühendisleri Odası
Necatibey St. No: 57, Kızılay, Ankara / Türkiye
Tel: +90.312.294 30 00 - Faks: 294 30 88
imo@imo.org.tr - www.imo.org.tr